공학박사 학위논문

Development of Hydrogen Retention Model Based on Plasma-Tungsten Interaction Analysis

플라즈마-텅스텐 상호작용 해석을 통한 수소 흡착 모델 개발

2018 년 2 월

서울대학교 대학원

에너지시스템공학부

진 영 길

Abstract

Development of Hydrogen Retention Model Based on Plasma-Tungsten Interaction Analysis

Younggil Jin
Department of Energy Systems Engineering
The Graduate School
Seoul National University

The hydrogen retention model using hydrogen particle balance equation was developed to explain temporal and spatial variation of hydrogen plasma properties (n_e, T_e) near the plasma-facing material boundary. The balance contains the outflux of hydrogen ions from plasma to wall and the influx of hydrogen neutrals from wall to plasma. Especially, the model considered the plasma-facing area where hydrogen retention occurs during operation. Tungsten was selected as wall material because it is a representative metal boundary as well as a promising fusion plasma-facing material. The influx equations from wall to plasma is functions of desorption energy set (E_{des}), which represents the various hydrogen retention reactions.

Hydrogen retention reactions in tungsten can occur as hydrogen solution, hydrogen oversaturation-induced vacancy trapping, implanted impurity-induced chemical trapping, physical damage-induced defect cluster trapping. The types of retention reactions are dependent on various plasma-wall interaction (PWI) conditions.

The model was firstly constructed with the assumption that plasma properties can be changed by neutral gas influx from wall material because it changes boundary condition between plasma and wall. The influx is recycling flux, which is dependent on volume retention reactions of hydrogen in wall material because retention reactions decide amount of recycling flux and period of recycling. Thus, the purpose of hydrogen retention model is to expect the variation of plasma as functions of hydrogen retention reactions in volume of wall material. The volume retention reaction rate is governed by desorption energies (E_{des}) of specific set of retention reactions because different set of retention reactions are formed by different PWI conditions.

Experiments to determine the hydrogen desorption energy (E_{des}) was in tungsten was performed with various PWI conditions as the deuterium plasma exposure onto tungsten, the deuterium plasma exposure onto carbon-implanted tungsten, the deuterium plasma exposure onto defect-formed tungsten, the gas-admixed ($P_{He\ or\ Ar}$ ~10-20%) deuterium plasma exposure onto tungsten, the deuterium plasma exposure onto recrystallized tungsten. Plasma was consistently exposed onto tungsten with electron cyclotron resonance (ECR) plasma system. The deuterium was used as hydrogen isotope because it has higher measurement reliability of thermal desorption spectroscopy (TDS) than hydrogen. The set of desorption energies of specific retention reactions were obtained by using TDS. Because accurate measurement of desorption energy is the precondition for present work, the reliability of TDS was confirmed by international TDS round robin experiment (TDS-RRE).

Hydrogen retention reactions in tungsten were figured out with corresponding desorption

energies; the hydrogen solution ($E_{des,0}$: 0.75-0.95 eV), the hydrogen oversaturation-induced vacancy trapping ($E_{des,1}$: 1.84 eV), the implanted carbon impurity-induced chemical trapping ($E_{des,2}$: 2.33 eV), and the physical damage-induced defect cluster trapping ($E_{des,3}$: 2.39 eV). In terms of variation effect in fusion-relevant condition, both He ash and Ar puffing gas effects were indirectly understood by using admixing condition. However, both gases did not change the desorption energy ($\Delta E_{des,i}$=0) compared to deuterium plasma case due to no formation of extrinsic trapping site. The effect of tungsten recrystallization was also analysed that can reduce hydrogen retention amount (ΔN_{wall}=30-50%) due to reduced fabrication-defects without the change of desorption energy ($\Delta E_{des,i}$=0). For the consideration of ion incident energy, the dimensions of volume retentions were extended from subsurface (nm ~ μm) to bulk (μm ~ mm) depending on the implanted plasma ions (100 eV/D_2^+), the impurity ions (300 eV/C^{4+}), and the high energy ions (2.8 MeV/W^{2+}). By using experimentally-obtained desorption energy data, the hydrogen retention model was constructed with long-term volume retention reactions and corresponding desorption energies.

Based on the model with experimentally-obtained desorption energy data, validation to expect temporal plasma variation with wall recovery time was performed. The wall recovery time explains settling time of plasma property as functions of retention reactions and corresponding desorption energies. The validation experiment showed that the longer wall recovery time (0 ~ 14,400 sec) for the hydrogen retention conditions with higher desorption energies (0.75 ~ 2.39 eV). Thus, long-term volume retentions dominate the settling time of plasma property as a rate determining step. The spatial variation of plasma was observed with distance from wall to plasma, where the variation of plasma density occur by hydrogen recycling, is comparable to mean free path (MFP) between neutral particles (D_2). The variation of plasma by volume retention reactions cannot be explained or expected by using conventional particle balance equation, which considers wall as fixed boundary. In this dissertation, the

extended particle balance was proposed with newly developed hydrogen retention model by considering volume retention reactions with dependence on plasma-wall interaction conditions. Therefore, the plasma-wall interaction must be considered to analyse wall as a transient boundary condition of plasma system.

Keywords: hydrogen retention model, plasma-wall interaction (PWI), hydrogen plasma, tungsten, thermal desorption spectroscopy (TDS).

Student ID: 2012-30268

Contents

List of Tables

List of Figures

Chapter 1 . Introduction

1.1 Motivation: Variation of hydrogen plasma by retention and recycling in wall material

Theoretically, hydrogen retention can be defined as physical adsorption (physisorption) or chemical adsorption (chemisorption) on surface, while, solution or trapping in volume of material. The trapping in volume is belong to long-term retention since it has significantly lower reaction rate at common operation temperature due to higher desorption energy than the other retention reactions. The time scale of recycling of long-term retention is longer than the unit operation time of plasma system, thus, we can define it as 'long-term retention' or static retention. The definition of the other retention reactions is short-term retention or dynamic retention such as surface adsorption and solution. Because the definition of desorption energy is summation between activation energy of diffusion and binding energy of trapping site, long-term retention occurs as volume retention reaction.

The cause of variation of bounded hydrogen plasma is mainly hydrogen retention in volume of wall because the volume retention reactions changes particle balance in plasma system for longer operation time scale than surface adsorptions. The variation is change of hydrogen plasma properties including plasma density (n_e) and electron temperature (T_e). Because of harsh condition to occur hydrogen retention, fusion plasma reactor should consider hydrogen retention as a cause of plasma variation. Researchers of fusion plasma reactor mentioned that the proper design of a fusion reactor is not possible unless there is an understanding of the hydrogen isotope retention and recycling [1]. For shot-to-shot operation of fusion plasma,

hydrogen can be retained into wall material during previous shot then the hydrogen can be recycled during following shot. R. Causey [1] pointed out 2 important issue: 1) from the tritium inventory point of view, it is absolutely necessary to understand the short-term and long-term hydrogen isotopes retention characteristics of the individual materials used for the first wall or divertor because the radioactive tritium limits the available shot to safety limit of fusion reactor, 2) from the plasma density and fueling point of view, it is necessary to understand the recycling characteristics of these materials. In common, long-term retention stands for static retention which has higher desorption energy occurred in volume while short-term retention stands for dynamic retention which has lower desorption energy occurred in surface.

Hydrogen retention is the interaction from plasma to material. While hydrogen recycling is the interaction from material to plasma. Hence the intrinsic interaction between plasma and material is retention and recycling. These characteristics are frequently observed in plasma system as shown in Figure 1-1 (a) and (b). The figures show variation of plasma density and electron temperature according to pre-ion irradiation fluence. The deuterium retention is proportional to pre-ion irradiation fluence and the recycling is proportional to retention amount. Thus, the figures imply plasma variation in bounded system will be changed as wall retention in increased with operation time.

For the retention point of view, previous researches have studied retention amount to expect even though the expectation is very limited for specifically assumed condition such as Figure 1-2 [2]. T. Tanabe [3] mentioned that extensive studies on hydrogen retention in tungsten loaded by ion implantation, plasma exposure have been done, reported amounts on H retention in W, and their dependences on the incident flux, fluence and temperature are very inconsistent.

For the recycling point of view, most representative case is easily found from KSTAR as shown in Figure 1-3. The figure shows the direct relationship between plasma and wall retention and recycling [4]. However, there is no significant change of plasma property for the condition

of recycling (recycling rate < 0). It is common result for present plasma system including tokamak because the retention amount is not sufficient to make effect recycling flux to be sufficient to change plasma property. Because the retention and recycling are not steady-state but transient, it is difficult to expect the variation of hydrogen plasma for long-term operation. Thus, the understanding of hydrogen retention is the key task for stable operation of plasma system during long-term operation. The importance of this phenomenon will be significant for long-term operation, harsh plasma-wall interaction condition, large plasma-facing material's area, and high permeability discharge gas such as hydrogen.

Therefore, the hydrogen retention model is necessary to expect plasma variation based on understanding of retention and recycling in plasma system. Developed model is for general plasma system, however, fusion relevant effect will be included to make a possibility of application of fusion reactor. Thus, relevant plasma surface-interaction condition will be considered as a cause of different retention and recycling reactions.

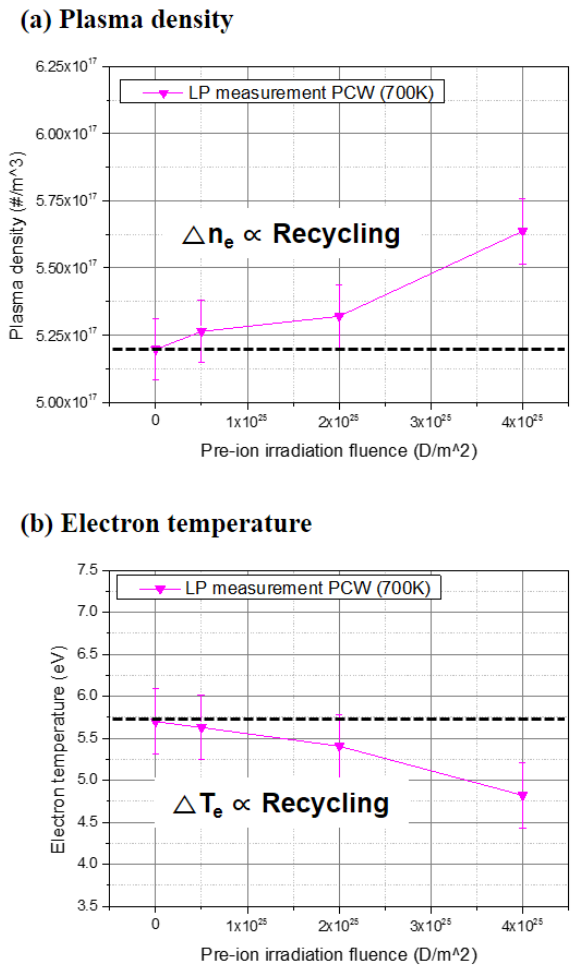

Figure 1-1. Plasma variation by recycling flux. (a) Variation of plasma density with pre-ion irradiation fluence, (b) variation of electron temperature with pre-ion irradiation fluence. The recycling flux has proportional relationship with pre-ion fluence because the retention amount is generally proportional to ion irradiation fluence.

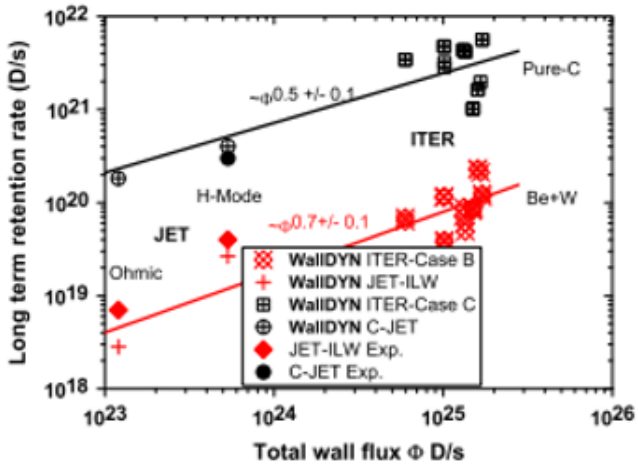

Figure 1-2. Long-term retention rate extrapolated by experimental data and WallDYN code results for specific operation condition and wall material [2].

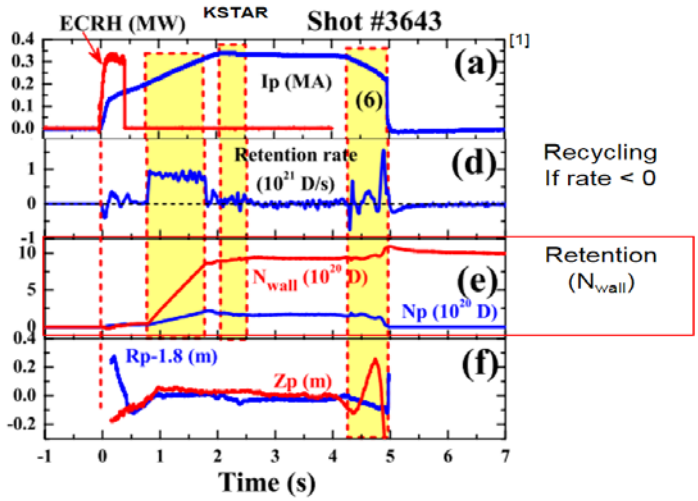

Figure 1-3. Shot record of KSTAR operation including retention rate and wall inventory (N_{wall}). The corresponding shot number is #3643 which is reported by KSTAR team and collaborative researcher [4].

1.2 Previous study: Lack of consideration on long-term retention and recycling

For this dissertation, the wall material was specified as a tungsten for present work because it is a representative metal boundary as well as promising fusion plasma-facing material. Hence, the retention reactions of hydrogen into tungsten will be considered, however, it is not implying that present study is only for tungsten but all material because the only difference is desorption energy but not types of retention reactions. Considered reactions also occur in all material.

Previous retention model has focused on 'retention itself' as a result because the retention study was performed by mainly fusion plasma research field, which has importance of tritium retention in terms of safety limit, rather than process plasma field. Furthermore, there is lack of long-term volume retention model because they were not arranged and defined obviously. Naturally, there is no consideration on plasma variation by retention because the operation time scale is still too short to consider long-term retention effect on recycling. However, for the preparation of long-term operation such as ITER or DEMO, long-term retention reaction is key phenomenon, which will dominate retention amount and recycling flux. In detail, most representative previous retention model is WallDYN [5]. Nevertheless Tanabe defines key retention phenomena including long-term retention as shown in review paper [3] and in Table 1-1, the retention model of WallDYN includes short-term retention reactions only such as surface adsorption, solution, surface co-deposition without trapping by hydrogen-induced defect, trapping by implanted chemical impurity, trapping by physical damaged-induced defect. The earlier reactions are short-term reactions while the latter reactions are long-term reactions. Because the long-term reaction is still ineffective for current experimental tokamak device such as JET, the long-term retention reaction was not included into model. In summary, previous retention studies mainly consider short-term retention reaction (dissociation, recombination) on

surface without consideration on long-term volume retention in volume. However, in case of hydrogen plasma for long-term operation, volume retention should be considered to understand recycled hydrogen influx from wall to plasma because the volume retention (trap) rate can be over the surface short-term retention reaction rate, depending on various plasma-wall interaction conditions.

For the hydrogen retention model point of view, previous all model does not include recycling flux into particle balance equation. Because of that, previous model only expects wall retention amount or retention rate nevertheless the recycling flux should be expected to operate plasma system stably without perturbation of recycled neutral gas flux from wall. Because of the lack of consideration on recycling flux, edge plasma condition such as ion temperature and plasma density were considered as fixed variable of outflux from plasma to wall material. Thus, the variation of plasma cannot be analysed with previous typical model. The case of WallDYN is arranged in Table 1-2.

Table 1-1. Coverage of previous hydrogen retention model for retention reaction in tungsten. [3], [6]

Retention reactions in Tungsten (Arranged by Tanabe in 2014 [3])		**Included in WallDYN**	**Time scale**
Surface adsorption (Intrinsic)		O	Short-term
Solution (Intrinsic volume)		O	Short-term
Surface co-deposition effect		O	Depends
Trapping (Extrinsic long-term retention in volume)	By H induced defect	X	Long-term
	By chemical Impurity	X	Long-term
	By physical defect	X	Long-term

Table 1-2. Parameter differences in the ITER background plasmas and how they qualitatively affect the WallDYN solution. [5]

Parameter	**Range**	**Effect**
Separatrix distance	10 cm, 4 cm	Charge states at the wall
Density	Low/Medium/High	Wall fluxes
Far SOL T_e/T_i	T_e = 10 eV, T_i = 20 eV or T_e =20 eV, T_i =50eV	Erosion rates
Far SOL V_{pep}	35 m/sec or 100 m /sec	Far SOL density
Far SOL *T-grad*	off or on	Erosion
Near SOL flux	0 or 0.5 Mach	Transport to inner divertor

1.3 Structure of proposed hydrogen retention model

This dissertation formulates the hydrogen retention model to explain plasma variation resulted from influx from wall to plasma by calculating neutral gas influx as functions of desorption energy (E_{des}) to consider into particle balance equation. The governing equation is particle balance equation, which consists of set of desorption rate equations for various volume retention reactions with desorption energies as activation energy of Arrhenius form. The desorption energies are formed differently depending on different plasma-wall interaction conditions. By using the desorption energy, variation of plasma can be explained by the definition of 0-dimensional particle balance equation including influx from wall to plasma as functions of volume retention reactions. For the modelling, wall is defined as plasma-facing area where hydrogen retention occurs during operation.

The key parameter is desorption energy of each volume retention reaction because both retention and recycling are functions of the desorption energy as activation energy in Arrhenius form. The function is as shown in equation (1.1). The retention amount is determined by desorption energy because the amount is the result of equilibrium between retention and desorption during plasma irradiation. Note that the desorption energy is the summation of activation energy of diffusion and binding energy of trapping site as shown in equation (1.2). The definition is understandable with potential wall of endothermic reactions in terms of transition state theory. Because the activation energy of diffusion is approximately constant in same material, the variable is binding energy which depends on trapping site. For the case of tungsten, the activation energy of diffusion is about 0.39 eV. Retention amount is determined by desorption energy as functions of each volume retention reaction. Therefore, the retention model should include most of hydrogen retention reactions and corresponding desorption energy data to formulate particle balance equation based on retention amount. In addition, recycling is also

determined by desorption energy. The desorption energy is the activation energy for hydrogen de-trapping from trapping site such as defect as shown in equation (1.3). Where the 1st term, the 2nd term, the 3rd term, the 4th term are net flux to surface of molecule, rate of recombination, rate of dissociation, atomic flux diffusing from bulk to surface, respectively. The recycling flux is proportional to atomic flux diffusing from bulk to surface. Thus, both retention and recycling are function of desorption energy depending different PWI condition. Therefore, present work builds the hydrogen retention model based on desorption energy of specific volume retention reactions for possible plasma-wall interaction condition, and then validate it with recycling experiment based on obtained desorption energy.

$$K_{des} = K_0 \exp\left(-E_{des} / kT\right) \tag{1.1}$$

$$E_{des} = E_{diff} + E_b \tag{1.2}$$

$$\begin{aligned} &\sum_i a_{m_s}\left(P_{m_i}K_{d_{m_i}} - K_{r_{m_i}}C_sC_{s,j}\right) + \sum_j \frac{C_sC_jD_s}{N\lambda} + C_s\lambda\left[\nu_0 \exp\left(-\frac{E_b}{kT}\right)\right] \\ &+D_s\nabla C_s\left(\sum_i n_i\left[\frac{D_s}{\lambda^2} - \nu_0 \exp\left(-\frac{E_{des}}{RT}\right)\right]\right) = 0 \end{aligned} \tag{1.3}$$

To validate hydrogen retention model if it can be used for expecting plasma variation, recycling experiment will be simulated with information of desorption energy of volume retention reaction as a cross-validation with experiment. However, it is not including power balance because it focuses on relative variation of plasma property due to recycling but not pursue expectation of absolute amount of plasma property values. This structure of model is described in Figure 1-4. The main difference between previous study and present study is consideration on long-term volume retention reaction and wall influx which is a function of

volume retention reaction parameter. The difference is also well described in the figure. Equation (1.4) and equation (1.5) also well show the difference of two cases.

$$\sum_j (\pm \mathrm{N}_j \, k_j \prod_l n_{R,l}) + \Gamma_H^{source} - \Gamma_H^{out} = 0 \tag{1.4}$$

$$\sum_j (\pm \mathrm{N}_j \, k_j \prod_l n_{R,l}) + \Gamma_H^{source} - \Gamma_H^{out} + \Gamma_H^{in} = 0 \tag{1.5}$$

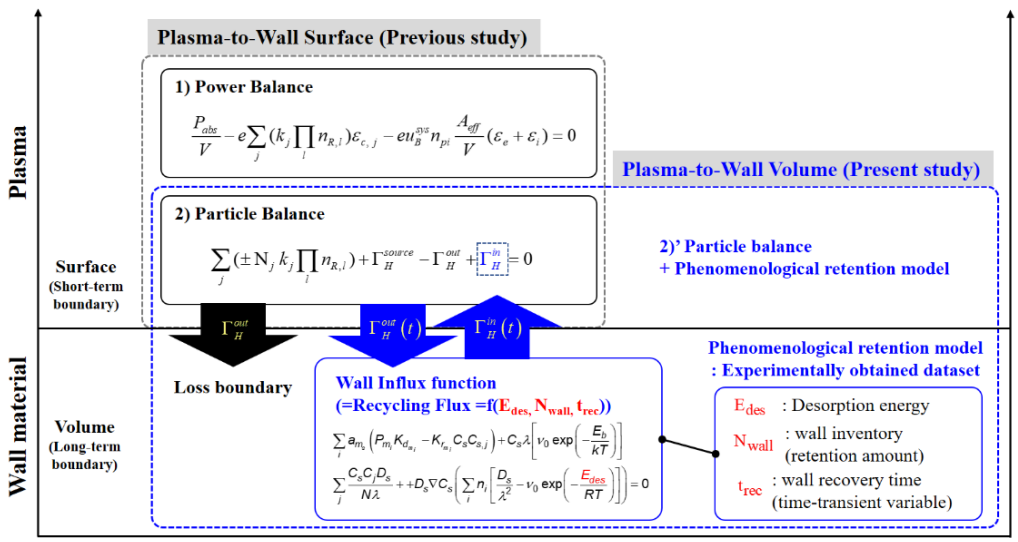

Figure 1-4 Structure of hydrogen retention model

Chapter 2 . Objectives and Strategy

To establish logical research, research strategy was arranged with definition of model and validation part. The hydrogen retention model includes various volume retention reactions into particle balance equations depending on PWI condition. Hence the particle balance equation is function of desorption energy (E_{des}) and wall recovery time ($f(E_{des})$). The definition of wall recovery time is that the time to consume retention amount to be equilibrium in terms of wall, while, the definition of settling time of plasma property is that time to consume from onset of variation to end of variation of plasma property in terms of plasma. Intrinsically, the two types of time definitions are same. The validation includes expected temporal variation of H plasma ($f(E_{des})$), and experimentally-measured temporal variation of H plasma ($f(E_{des})$). Overall parts are described in Figure 2-1. In addition, to simulate plasma-wall interaction conditions, corresponding experimental condition were arranged with the condition as shown in Table 2-1. The table clearly show that the plasma-wall interaction conditions of present work is not sufficient to upper limit of fusion plasma condition, but it is approximately like lower limit of fusion plasma. Thus, with the assumption that the degree of plasma condition makes no new mechanism but the only thing different is degree of effect, we can extrapolate the results from process plasma to fusion plasma.

With the preposition, the development of hydrogen retention model has been carried out as arranged in Figure 2-2. First, characterization of desorption energy of long-term volume retention reactions was carried out to estimate desorption rate function for particle balance equation. To achieve that, 3 of main extrinsic PWI conditions were included in main experimental work. The conditions include deuterium plasma exposure onto tungsten,

deuterium plasma exposure onto carbon-implanted tungsten, deuterium plasma exposure onto defect-formed tungsten, gas-admixed (10-20 *vol.%*) deuterium plasma exposure onto tungsten, deuterium plasma exposure onto recrystallized tungsten. The first one will show hydrogen induced intrinsic volume retention reaction, which implies the hydrogen retention can be enhanced by hydrogen itself during long-term operation even though there is no extrinsic effect. While, the second one will show implanted chemical impurity-induced volume reaction which will occur in multi-material configuration, implying that the impurity with high hydrogen affinity can be the additional source of long-term hydrogen volume retention when it implants into tungsten material. The third one will present physical damage induced volume retention reaction which can occur under high energy particle impact such as high energy ion, self-ion, and neutron. The energy of self-ion will not be constant because it is result of sputtering and re-implantation while the energy of neutron will be approximately 14.1 MeV because it is results of fusion reaction. In addition to the PWI condition, fusion-relevant effects of both He ash gas and Ar puffing gas were indirectly investigated by using admixing condition into deuterium plasma with known variation of plasma density to confirm whether the variation of retention is larger than variation of plasma density variation or not. For the case of the variation of retention is larger than variation of plasma density, we can conclude that the gases has effect on retention by intrinsic characteristics of the gas. In addition, the heat flux-induced recrystallization effect was also investigated to consider material changes during operation.

For the main reactions, the desorption energy (E_{des}) will be measured by using thermal desorption spectroscopy (TDS). As mentioned earlier, the desorption energy is the key parameter of present study because it dominates recycling flux as well as retention amount for given plasma-tungsten interaction condition as mentioned earlier. According to desorption rate shown in Figure 2-3, only 0.1 eV makes $10^{1\text{-}2}$ of desorption rate (K_{des}) hence the accurate measurement of E_{des} is essential. Thus, to improve the accuracy and consistency of hydrogen

retention model, the TDS was developed and improved to enable measure hydrogen desorption energy. Based on overall point of view, the strategy includes development of TDS. Next section will show the detail of development of TDS in present work.

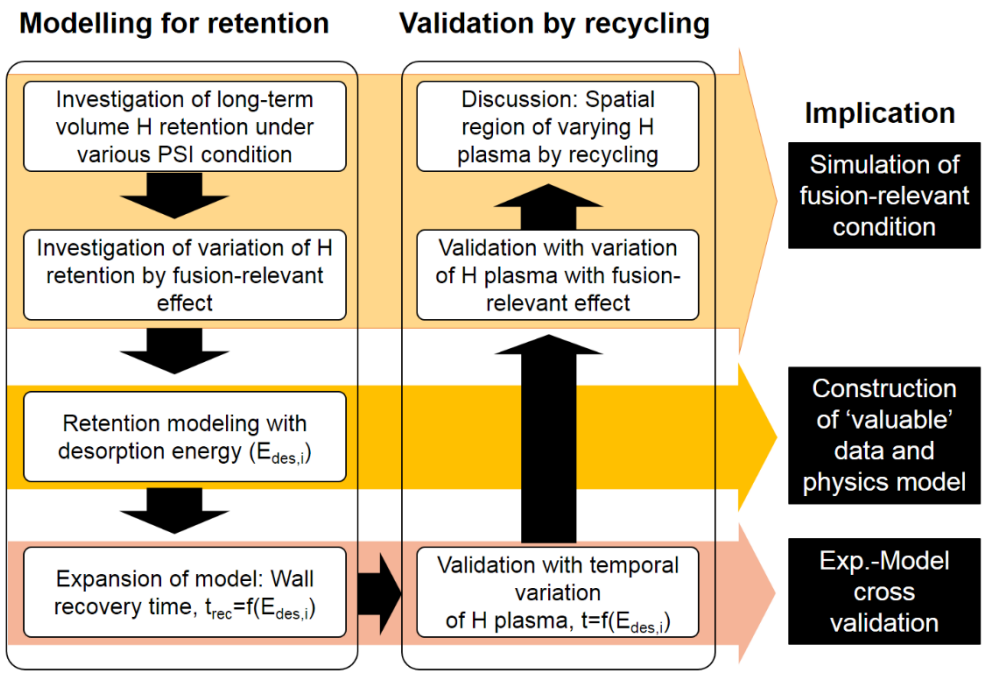

Figure 2-1. The description of research strategy with definition of model and validation part. The model is arranged including volume retention mechanism under PWI variation of retention, volume retention parameter (E_{des}), wall recovery time ($f(E_{des})$). The validation includes temporal variation of H plasma ($f(E_{des})$), variation of h plasma, temporal variation of H plasma ($f(E_{des})$).

Table 2-1. Definition of fusion-relevant plasma-wall interaction condition.

Condition	**SNU-ECR**	**Fusion relevant condition**	
		Lower limit condition	Upper limit condition
Ion incident energy	E_{sh}~10-300 eV	E_{sh}<100 eV	E_{sh} ~ 0 eV
($E_i=E_{sh}+E_{th}$)		(detach mode, ion [7])	(ash, neutral)
	E_{th}~0 eV	E_{th} ~ 0 eV	E_{th} ~ 3.5 MeV
	E_i~10-300 eV	E_i<100 eV	E_i ~ 3.5 MeV
Ion flux	~10^{21} He/m^2-s	~10^{20} He/m^2-s	~10^{23} He/m^2-s
		dep. on 1st wall/divertor and scenario, considering fraction ~10% He for D plasma [8], [9]	
Admixing fraction	0-20 *vol.%*	5 *vol.%* [10]	25 *vol.%* [10]
Ion fluence	~10^{25} He/m^2	~$10^{23\text{-}25}$ He/m^2	~$10^{28\text{-}30}$ He/m^2
(defined by operating time)		dep. on operation time, considering fraction ~10% He for D plasma, Divertor strike point for unit shot 400 s [8]	
Mixing condition	simul. /seq.	simultaneous	
Tungsten temp.	400-900 K	400 K [8] (~DBTT, non-strike point)	1200 K [8] (~RCT, strike point)

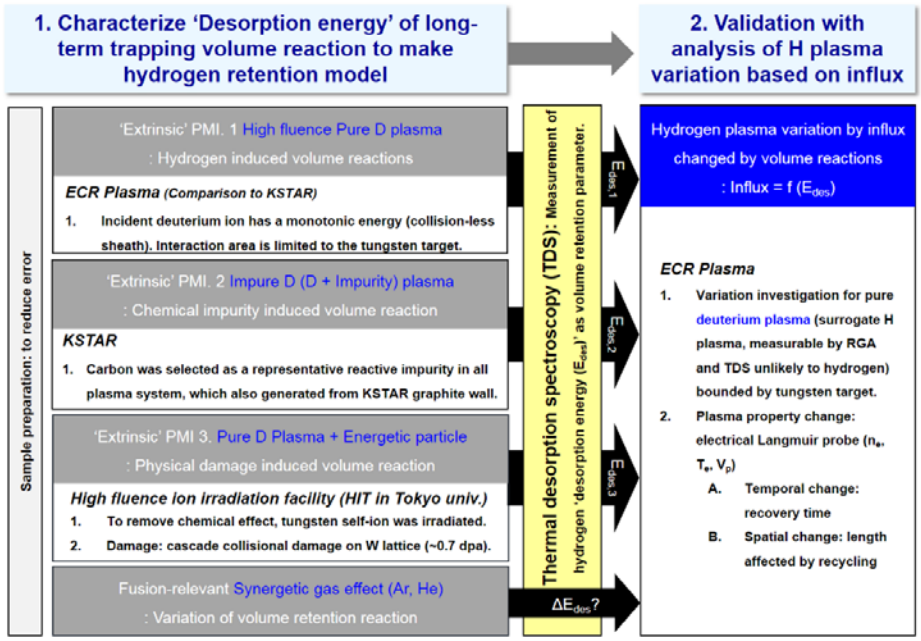

Figure 2-2. Description of strategy for developing hydrogen retention model considering plasma-wall interaction

.

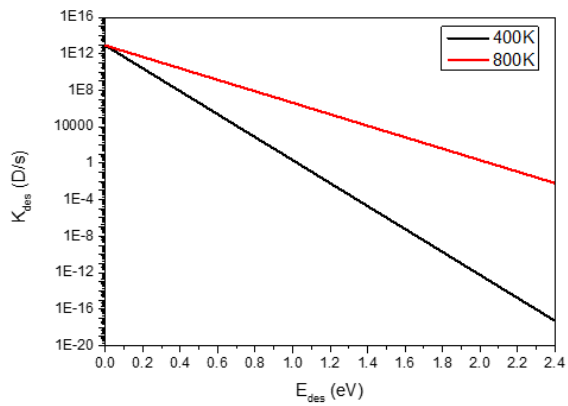

Figure 2-3. Example of desorption rate calculated as a function of desorption energy with two different temperature conditions.

Chapter 3 . Development of Thermal Desorption Spectroscopy (TDS) to Characterize Desorption Energy as Retention Parameter

To measure desorption energy accurately for various volume retention reactions, thermal desorption spectroscopy was developed via arrangement of principle, design of TDS, and standardization of TDS methodology with interactional TDS Round Robin Experiment (TDS-RRE). The 3 of procedure is essential to confirm reliability of TDS methodology to improve accuracy and consistency. Previous most of retention data of lots of group show scatter of data due to lack of some of three procedure [11]. The detail will be discussed in following sections.

3.1 Principle of thermal desorption spectroscopy (TDS)

The thermal desorption spectroscopy, generally called TDS, is the diagnostic consist of residual gas analyzer and the linear heating furnace, and high vacuum chamber system. Basically, the principle of TDS is that the higher energy is required to be de-trapping the higher temperature is need for de-trapping. In other words, the de-trapping of deuterium is proportional to temperature when the heating rate is constant (linearity of TDS). The Figure 3-1 well show the principle. Theoretically, heating rate (β) sets with 1 K/s which is satisfied to the Redhead approximation (equation (3.1)) based on Kissinger equation (equation (3.2)) [12], being adapted to the analysis of the desorption energy from the TDS spectra. Note that the approximation provides a low error rate of < 1.5% when $10^8 < \nu/\beta < 10^{13}$ K^{-1}, where ν is the Debye frequency.

The desorption property can be analyzed by using the approximation of [13] as shown in equation (3.2),

$$E_{des} = RT_p \left[\ln\left(\frac{\nu_1 T_p}{\beta} \right) - 3.64 \right] = f\left(T_p\right) \tag{3.1}$$

$$r_d = \frac{\sigma_A d\Theta_r}{dt} = \nu_n \sigma_A^n \Theta_A^n \exp\left(-E_{des} / kT\right) \tag{3.2}$$

where ν is the pre-exponential factor of the first order desorption (~ 10^{13} s^{-1}), E_{des} is the activation energy of desorption, R is the gas constant, and T_p is the peak temperature of the TDS spectrum. According to equation (3.2), the peak temperature of TDS represents to desorption energy of deuterium from the trapping site, so the corresponded defect type can be analyzed as shown in Figure 3-2.

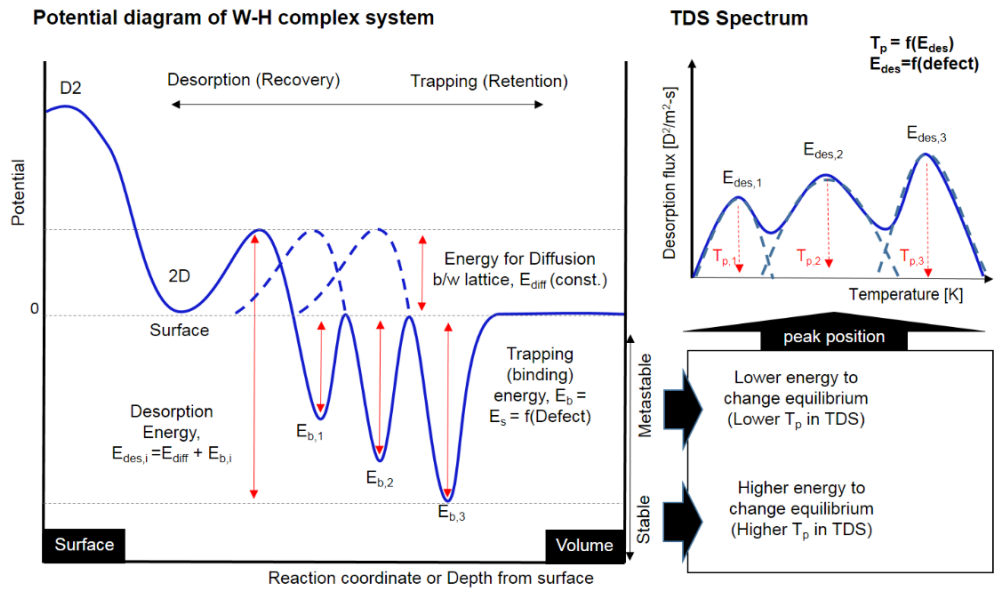

Figure 3-1. Principle of thermal desorption spectroscopy, which is consist of potential diagram of W-H complex system and the relationship with TDS spectrum.

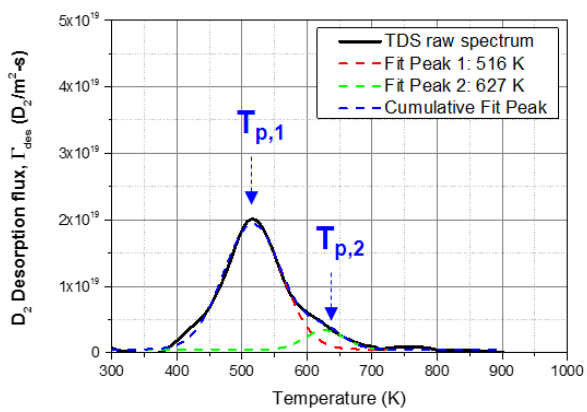

Figure 3-2. Example of TDS spectrum for hydrogen retention in tungsten. The spectrum shows peaks at 516 K and 627 K indicating 1.55 eV and 1.89 eV of desorption energy, respectively.

3.2 Development of TDS to measure accurate desorption energy of volume hydrogen retention

Thermal desorption spectroscopy of Seoul National University (SNU-TDS) was developed in this study to adapt study on hydrogen retention model. Figure 3-3 shows that the description of SNU-TDS system. In commercial, there is no appropriate thermal desorption spectroscopy which ensures low outgas rate and high vacuum pressure, and linear heating rate.

The requirement of TDS system for advanced retention study with reliable data need linear ramp up rate of temperature, high mass resolution of residual gas analyzer (RGA) or quadrupole mass spectroscopy (QMS), and high vacuum system with negligible outgas. The linear ramp up rate is important to determine hydrogen desorption energy from trapping site because desorption energy is calculated from the desorption temperature. These factors are important to estimate desorption energy for specific volume retention in tungsten because the little error in desorption energy (E_{des}) makes large error in desorption rate (K_{des}) as discussed in section 1.3. Thus, the consistence between sample temperature and furnace temperature is also important as well as linearity of heating furnace. The mass resolution of RGA is important in case of isotope is included in residual gas such as hydrogen and deuterium. The high vacuum chamber is also necessary because outgas from system can disturb signal of hydrogen isotope gas. Just in case, hydrogen can be mixed with water as a form of HDO, D_2O. By refined designing of SNU-TDS, it was obtained that no outgas source, minimized TDS chamber, utility, minimizing thermocouple measuring error, minimize gauge distortion, and proper positioning of gauge and RGA for correction factor estimation at the same location.

The specification of developed SNU-TDS was compared to overseas research group to make sure achievement of SNU-TDS. Table 3-1 shows the specification including ramp rate (TDS temperature resolution), Maximum temperature (TDS scope), TDS time interval, TDS gas

purity, TDS mass resolution. As arranged in table, most of all specification of SNU-TDS meets minimum standards of TDS.

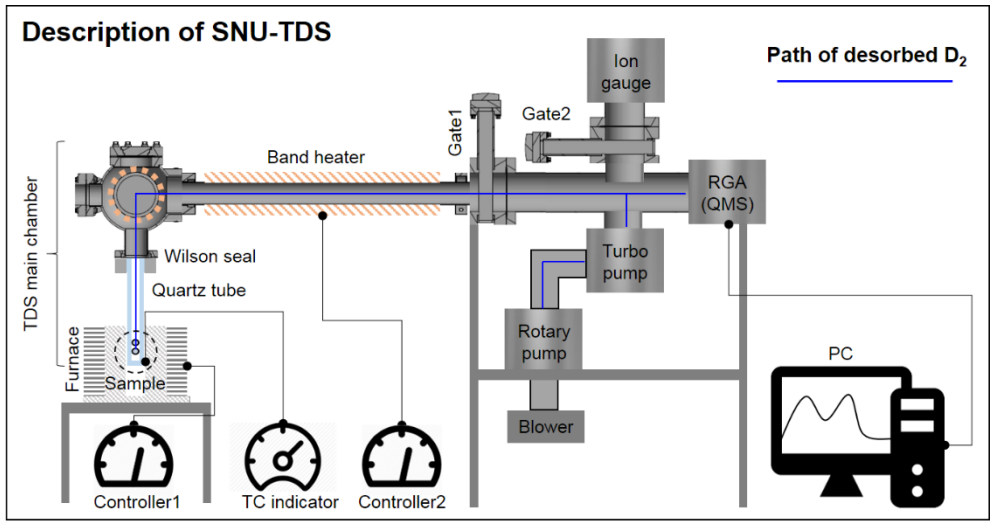

Figure 3-3. The description of SNU-TDS system developed in present work. The system is ex-situ type facility, which consists of plasma source chamber, residual gas analyzer, linear heating furnace, and high vacuum system.

Table 3-1 Specification of SNU-TDS with comparison to main groups of retention study.

Specification	**SNU PAL**	**INL**	**JAEA**	**IPP**	**IAEA recommended**
Type	Ex-situ	Ex-situ	Ex-situ	Ex-situ	N/A
Ramp rate	10-60 K/min (1-6 counts/K)	10 K/min (6 counts/K)	6-30 K/min (2-10 counts/K)	120 K/min (0.5 counts/K)	6-60 K/min (1-10 counts/K)
Maximum temperature	1273 K (cover W~900 K)	1273 K (cover W~900 K)	1273 K (cover W~900 K)	1750 K (cover W~900 K, C~1400K)	1273 K (cover W~900 K)
TDS time interval	<few days	19 h	N/A	Several months	<1 month
TDS gas purity	D_2, HD, HDO, D_2O	D_2, HD	D_2, HD, HDO, D_2O	D_2, HD	D_2, HD, (+H_2, H_2O, HDO, D_2O
TDS mass resolution	0.1 amu (QMS) 1.0 amu (RGA)	0.1 amu (QMS)	0.1 amu (QMS)	0.1 amu (QMS)	N/A

3.3 Standardization of TDS methodology

To obtain reliable and reproducible data from TDS, methodology is also standardized as well as system development. The methodology is also main reason of that there is large scattering between TDS data even though the experimental condition is not so much different between research groups. Thus, the methodology was arranged in this study. The arranged main process can be summarized as 3 steps: 0) TDS background measurement without sample, 1) RGA raw data measurement with sample, 2) Calibration of TDS spectrum with background signal and temperature profile. The detained procedure of TDS is arranged in Table 3-2. By step 0), the system outgas can be removed from sample outgas signal. By step 1), main data of TDS experiment is obtained. Then by step 2), the residual gas analyzer data can be calibrated to TDS data consisting of temperature and desorption flux from time and partial pressure.

For the consistency of data analysis, standard procedure for TDS data analysis is also established. The procedure consists of data smoothing and peak analysis. Data smoothing consists of 1) acquisition of RGA raw data, 2) peak smoothing with moving average, and 3) TDS peak deconvolution. The example of procedure is shown in Figure 3-4. The detail of analysis for TDS to extract desorption energy is arranged in Figure 3-5.

The peak analysis can be performed with reference information of possible desorption energy between hydrogen and tungsten as arranged in Table 3-3, which were taking from other literatures [14]–[17]. The table was arranged and confirmed as results of this study. The detailed result is in results section. Based on the reference data, The retention enhancement of damaged tungsten was investigated by using the TDS system constructed in the Plasma Application Laboratory of Seoul National University [13].

Table 3-2. Standard procedure of TDS measurement.

1. Background signal acquisition (without sample)	
1.1	Baking (50°C, 1h): setup heater 30°C in 1h due to overshooting
1.2	Outgas pumping (>24h) for Base Pressure < $2x10^{-6}$ Torr
1.3	RGA conditioning (Warm-up time: Mass stability ±0.1 amu after 30 minutes.)
1.4	Repeat filament degas and pumping until P_{H2O} < 20% of P_{total}.
1.5	Turn off ion gauge to prevent loss of rare neutral gas by ion gauge.
1.6	Trend data acquisition until saturation of HD, D_2, H_2O.
1.7	RGA recording (20 sample/amu) with linear temperature ramp up (setup heater ~ 1200°C/60min for 20K/min) ➔ Guarantee range: 20-820°C in 40 min.
2. Main signal acquisition (with sample)	
2.1	Same process of 1 ~ 7 *check point: similar pressure range with 1.

Table 3-3. Types of trapping of *D* in tungsten including desorption energy (E_{des}) and corresponding TDS peak temperature (T_{peak}) for given heating rate.

E_{des} **: Desorption energy**	***E_b*** **: Binding energy**	**Expected *T_p* : Peak temperature in the TDS spectrum**	**Observed *T_p* in the PCW-(v) TDS spectrum**	**Reference**
0.75–0.95 eV	**0.35–0.55 eV (D solution in W +Dislocation trap)**	**350–550 K**	**439-516 K**	[13], [17]
1.84 eV	**1.45 eV (vacancy-D trap)**	**566–666 K**	**600-647 K**	[13], [18], [19]
2.33 eV	**1.94 eV (cluster, cavity)**	**700–800 K**	**799 K**	[3]
2.39 eV	**2.0 eV (*C-D* trap)**	**746–846 K**	**709-766 K**	[20]

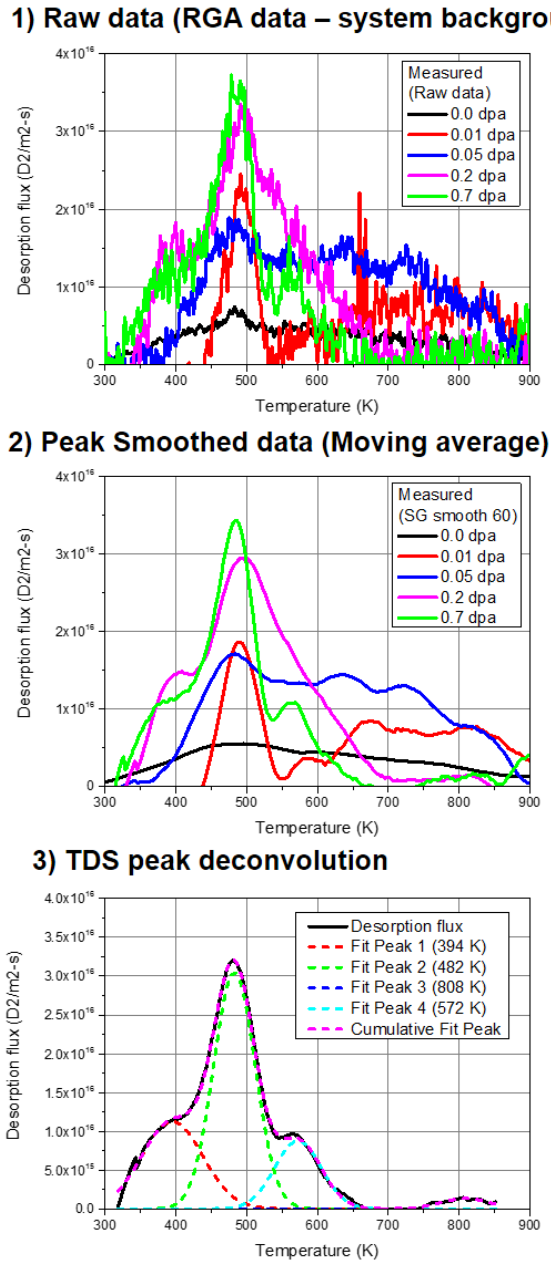

Figure 3-4. Example of standard procedure for TDS data analysis. The procedure consists of 1) RGA raw data acquisition, 2) peak smoothing with moving average, 3) TDS peak deconvolution.

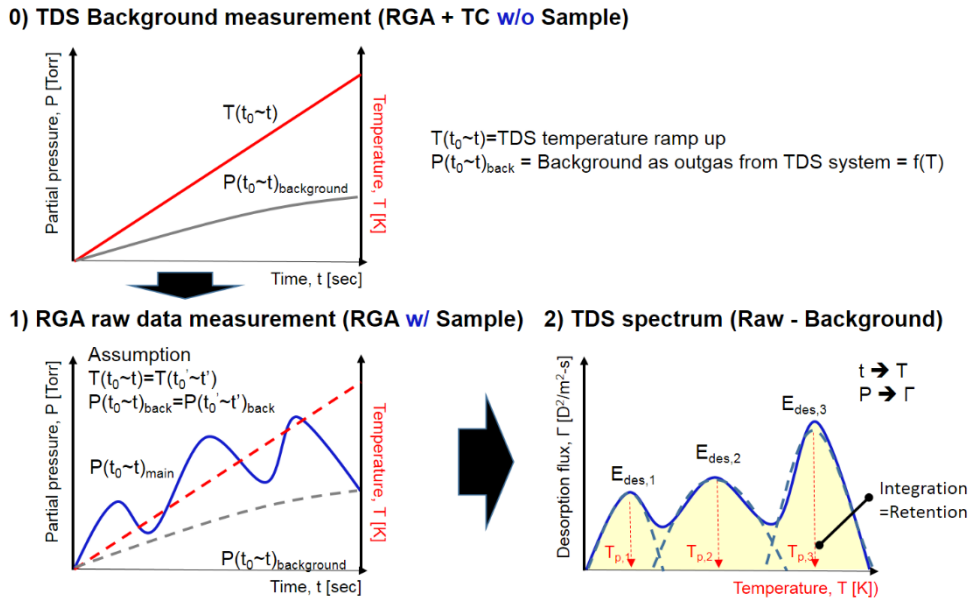

Figure 3-5. Standardized TDS methodology with detailed 3 steps: 0) TDS background measurement without sample, 1) RGA raw data measurement with sample, 2) Calibration of TDS spectrum with background signal and temperature profile.

To establish reliability of TDS system and methodology, we have participated for round robin experiment for thermal desorption spectroscopy (TDS-RRE). TDS-RRE was initiated by IAEA CRP (Code = F43021: Plasma-Wall Interaction with Irradiated Tungsten and Tungsten Alloys in Fusion Devices) to improve achievement of coordinated research program (CRP) by making international standard for plasma-wall interaction diagnostic. The purpose of TDS-RRE is 'International standardization' of thermal desorption spectroscopy organized by IAEA based on CRP. Making standard procedure for TDS is due to scattered data of research groups nevertheless its significance on safety limit analysis of fusion reactor. TDS-RRE pursues confirmation of reliability and reproducibility of TDS data with 'cross-validation' by comparison between participants. The program is not for mechanism study but reliability of measurement itself. The participants of the program are arranged in Table 3-4. The TDS data for standard samples are collected from participants to compare data quantitatively and to find solution to standardize TDS methodology internationally. By participating the TDS-RRE, SNU-TDS was validated that it has relatively higher accuracy and consistency as shown in Figure 3-6. The accuracy was estimated by comparting retention amount between nuclear reaction analysis (NRA) and TDS, and between participants. The consistency was estimated by testing TDS system whether it can distinguish slightly different standard samples.

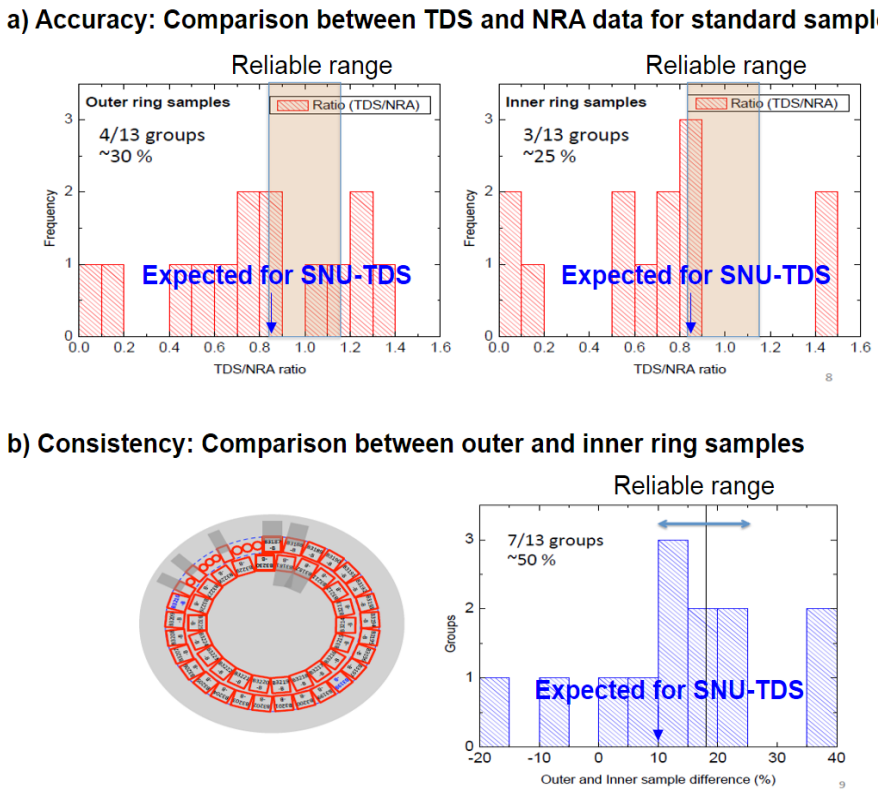

Figure 3-6. The results of TDS-RRE for TDS standardization. a) accuracy: comparison between TDS and NRA data for standard samples, b) consistency: comparison between outer and inner ring samples.

Table 3-4. Participants of TDS-RRE

Name	Affiliation
Alexander Pisarev	National Research Nuclear University "MEPhI", Moscow, Russian Federation
Brian D. Wirth	University of Tennessee, USA
Christian Grisolia, R. Bisson, E. Hodille, Commissariat	Energie Atomique, Cadarache, France/ Aix-Marseille University, France
Davide Curreli	University of Illinois at Urbana Champaign, Urbana IL, USA
Guang-Nan Luo	Institute of Plasma Physics, Chinese Academy of Sciences, Hefei, People's Republic of China
Heun Tae Lee	Osaka University, Osaka, Japan
Jim W. Davis, Tamara Finlay	University of Toronto, Canada
Jochen Linke	Bernard Unterberg, Forschungszentrum Julich, Germany
Long Cheng	Beihang University, Beijing, People's Republic of China
Masashi Shimada, Chase Taylor	Idaho National Laboratory, USA
Mizuki Sakamoto	University of Tsukuba, Japan
Sabina Markelj	Josef Stefan Institute, Ljubljana, Slovenia
Yuji Hatano	Toyama University, Japan
Younggil Jin and Gon-Ho Kim	Seoul National University, South Korea
Hyun-Kyung Chung	International Atomic Energy Agency, Vienna, Austria

Chapter 4 . Hydrogen Retention Model Based on Desorption Energy for Various Plasma-Wall Interactions

4.1 Hydrogen retention reactions under plasma-tungsten interaction condition

Plasma-facing tungsten material under hydrogen plasma will be exposed by mainly hydrogen ion. Thus, the intrinsic volume retention reaction will be dominated by hydrogen plasma irradiation condition such as ion fluence in long-term operation. In addition, there obviously will be impurity ions and high energy ions, especially for fusion plasma, neutron, sputtered W self-ion, carbon impurity ion, Ar puffing gas, and He ash. Thus, in this section, the hydrogen retention reactions will be investigated with focusing on desorption energy as volume retention parameter. Above condition was arranged by Tanabe as effective long-term retention phenomena of tungsten.

4.2 Hydrogen-induced intrinsic volume retention: H solution ($E_{des,0}$) and H oversaturation ($E_{des,1}$)

4.2.1 **Introduction**

To investigate hydrogen-induced intrinsic volume retention reactions, TDS experiment was performed for the condition of deuterium plasma exposure onto tungsten.

In general, incident hydrogen firstly forms solution reaction in tungsten lattice. The other hydrogen-induced intrinsic phenomenon occurs for higher hydrogen fluence case: implanted deuterium in tungsten reaches its oversaturation concentration and makes vacancy defect depending on deuterium solubility in tungsten. The phenomenon is important because it can induce long-term retention even there is no other extrinsic effect such as high energy particle or impurity. Thus, the understanding of hydrogen oversaturation in tungsten is precondition to understand all volume retention reaction in tungsten. Because the phenomenon depends on the ion incident energy and ion fluence, the study for hydrogen oversaturation considers those two factors for experiment.

Basically, the deuterium retention of tungsten is negligible due to its low solubility for hydrogen [21], so ideal tungsten is concerned as a low retention material. This ideal property is often not adapted in the practical use of tungsten, especially, in the plasma-wall interaction condition (PWI) because the high energy ions cause various defects in tungsten and increases retention. J. Roth *et al.* [22] and Z. Tian *et al.* [23] suggested that the ion-induced defect formation could be induced by the deuterium oversaturation as well as the high energy ion-induced cascade collisional damage. Recently, it reports that the experimental observation of ion-induced defect fraction is increase up to 5×10^{-2} *at.%* during PWI, which value is greater than the intrinsic defect (4×10^{-4} *at.%*) [24]. Tanabe suggested that the oversaturation of

incident deuterium ion could increase the local stress field and induce defects even though the ion energy is low. [3] It implies that a low solubility of tungsten can be disadvantages for long-term operation if the oversaturation dominates retention. Recent study proposed that the oversaturation-induced defect forms through a formation of self-interstitial atoms (SIAs) of W by accumulated deuterium [25], [26]. From those previous studies, it concludes that the low energy deuterium ion may induce the defect formation and change the retention of W. However, previous researches can't explain the oversaturation depth and PWI condition dependency because there is no systematic investigation with consideration of ion energy and fluence. It is not aware the ion irradiation condition for oversaturation induced defect and retention changes which is triggering to our experiments. Thus, present work has significance as a first experiment to examine oversaturation.

In this study, the irradiation ion energy chose in care after analyzing the cascade collisional defect formation from the SRIM simulations. The region of oversaturation in deuterium (D) ion induced W is investigated from the analysis of secondary ion mass spectroscopy (SIMS) data and the defect property is analyzed using the thermal desorption spectroscopy (TDS) measurement. Results shows the back up for the proposed mechanism of oversaturation induced defect formation on W irradiated by plasma ion and, especially it clearly reveals that the energy region which is lower than that of the cascade collisional defect formation.

Through the overall experiment, the volume retention reactions and corresponding desorption energies will be revealed for deuterium plasma-facing tungsten condition.

4.2.2 **Experimental setup**

Experiment was performed with series procedure: 1) deuterium plasma irradiation on tungsten by electron cyclotron resonance (ECR) plasma system, 2) retention characterizing by TDS, 3) the other post-mortem analysis. To reduce redundancy of description, experimental setup mainly arranged with plasma irradiation condition and other post-mortem analysis excepting setup for TDS, which is arranged in previous section and is consistent to all experiment.

All experiments were performed with mechanically polished tungsten samples (ITER-grade tungsten, Plansee), which has 99.96% purity and dimension of 10 mm diameter and 3 mm thickness. The specimens were pre-annealed with 573 K for 12 hours to remove intrinsic defect to distinguish ion-induced defect only. After pre-treatment, the samples were irradiated in ECR plasma system with a low ion energy of 100 eV/D_2^+ according to an 87 V target bias and -13 V plasma potential in D_2^+ dominant plasma. It provides the similar condition of far scrape-off layer (far-SOL) in fusion reactor.

Figure 4-1 shows a schematic of ECR plasma source used in this study. It consists of a stainless steel cylindrical chamber with microwave generator [27]. The electron density and temperature of the plasma near the target were determined using Langmuir probe measurement. The estimated electron density and temperature were 3.4×10^{17} m^{-3} and 5 eV, respectively. The ion flux on the tungsten target assumed to meet Bohm flux condition [28], analyzing the flux 2.8×10^{21} D_2^+/m^2s. The condition is relevant to far SOL region of KSTAR that facing 1st wall, which has ion flux about ~10^{21} D^+/m^2s and ion energy under 100 eV [29]. During deuterium ion irradiation, the temperature of tungsten species increases due to heat up from the irradiated ion energy transferred but it was controlled 700-800 K by the active cooling system. The temperature will be considered theoretical threshold condition for

oversaturation because the concentration is dependent on material temperature.

To distinguish the oversaturation-induced defect formation from cascade collisional damage, the energy of irradiation ion is chosen under the threshold energy of cascade-induced defect formation in W. The threshold energy of defect formation by cascade collisional damage was investigated from SRIM 2013 (the stopping and range of ions in matter) [30] simulations, which are shown in Figure 4-2. Defect formation rates from irradiated D^+, D_2^+, and D_3^+ vary with difference incident energy ranged of 50-2000 eV at normal angle incident to consider mixed ion D plasma. This simulation cannot provide the oversaturation damage. The results show the minimum threshold energy for cascade collisional damage is ~250 eV for considering all deuterium ions because the defect formation rate (vacancy, displacement) is zero under 250 eV. Thus, the incident energy (E_i) should be larger than 250 eV. Thus, the chosen ion incident energy of 100 eV is far less than the cascade collisional damage threshold. Therefore, it can be assumed that the ion energy of present study (100 eV/D_2^+) induce defect formation by only oversaturation damage but no cascade collisional damage.

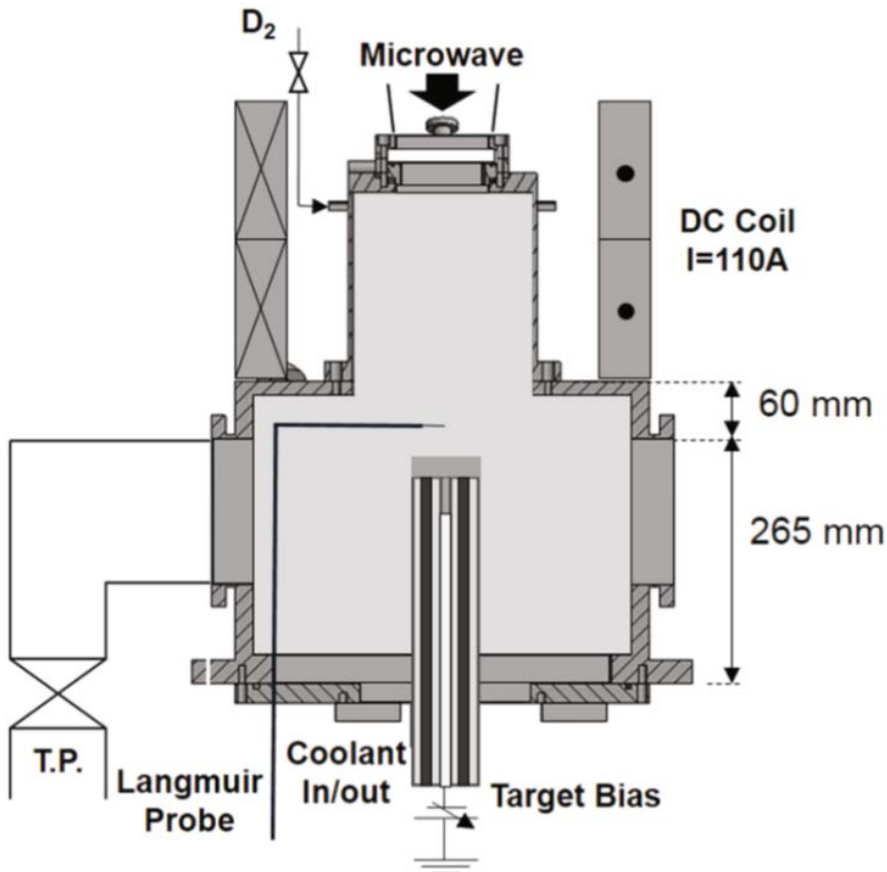

Figure 4-1. The electron cyclotron resonance (ECR) plasma source generates a deuterium plasma density of ~3.4 × 10^{17} m^{-3} and at a temperature of 5 eV. From assumptions of D+ 2 dominating and a Bohm current, the ion flux is 2.8 × 10^{21} D^{+2} /m^2s. The sheath potential is 100 eV, so the incident ion energy is 100 eV/D_2^+.

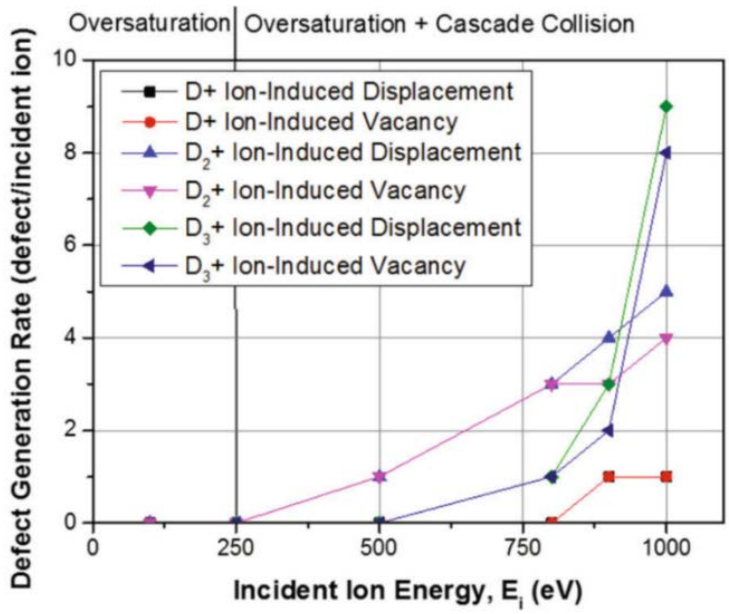

Figure 4-2. Defect formation rate per incident ion caused by cascade collisional damage as a function of the energy of the ion, calculated by using SRIM 2013 with full cascade. The damage consists of a displacement and a vacancy for each deuterium ion, D^+, D_2^+ , and D_3^+ , for energies of 50 − 2000 eV. The incident ions are in the normal direction ($\psi = 0^\circ$).

After ion irradiation, the SIMS (TOF-SIMS-5, ION-OF) measurement for the deuterium irradiated W is carried out. Since SIMS measurement is conducted 3-4 days after plasma irradiation, it can release the information mostly of the trapped particle in the defect of W. The generated defect enhances trapping at forming zone, the existence of defect and oversaturation depth can be revealed by peaked region in retained D depth profile that is obtained by SIMS. Note that the position of defect and oversaturation depth is same because the defect can be form at the boundary of oversaturated region according to suggested mechanism [3]. Since using low power SIMS measurement, it is suitable to resolve nm-scale depth profile for analyzing oversaturation depth, having the depth resolution ranged of 0.6-1 nm The SIMS measurements of deuterium retention profile in depth collected in the flat surface regions with the sputter area (150 x 150 μm^2) and the detection area (40 x 40 μm^2) which may avoid the systematic error from top and bottom critical dimension difference. After SIMS measurements, Profiler (DXT-A, Bruker) measured the sputtered depth after SIMS measurement to correct sputtering depth.

Figure 4-3 show the FESEM images of the tungsten samples before and after low energy deuterium ion irradiation. Figure 4-3 (a) represents the image of the tungsten pristine. Figure 4-3 (b), (c), and (d) represent the images after irradiation for D_2^+ ion fluence of 0.5 x 10^{25} D/m^2, 2.0 x 10^{25} D/m^2, and 4.0 x 10^{25} D/m^2, respectively. While the pristine show just mirror-like flat surface, the irradiated samples have the blister structure that formation induces from the plastic deformation induced by the retained deuterium in tungsten [21], [31]. Notes that it implies retained deuterium in intrinsic defect free W regardless of its low solubility [21]. The inside square region in Figure 4-3 indicates the spot size of SIMS measurement and SIMS data are shown in Figure 4-4.

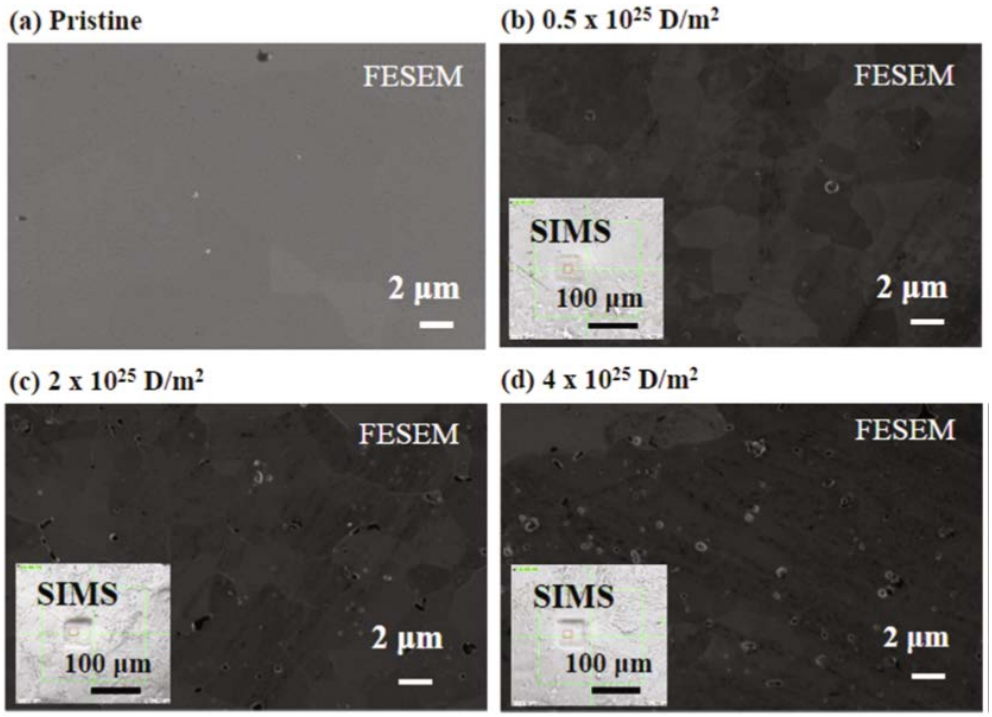

Figure 4-3. FESEM images of deuterium ion-irradiated tungsten: (a) pristine tungsten before irradiation and tungsten irradiated with deuterium ions at fluence of (b) 0.5×10^{25} D/m^2, (c) 2.0×10^{25} D/m^2, and (d) 4.0×10^{25} D/m^2. The square spot in the insert plot represents the region of the SIMS measurement.

4.2.3 **Hydrogen-induced volume retention reactions and corresponding desorption energy**

Figure 4-4 (a)-(c) show the SIMS measurement for various deuterium irradiation on tungsten, (a) 0.5 x 10^{25} D/m^2, (b) 2.0 x 10^{25} D/m^2, and (c) 4.0 x 10^{25} D/m^2, respectively. At depth = 0, the amount of D concentration corresponded to the surface adsorption property is limited to small value ~10 which are almost the same for various ion fluence conditions as shown in Figure 4-4 (a)-(c). High intensity peak indicates using arrow in the figures. The depths of high intensity peak were observed only 15 nm for 2.0 x 10^{25} D/m^2, and 16 nm for 4.0 x 10^{25} D/m^2, respectively. The peak intensity is about 15-16 nm from surface. Notes that the depth is slightly deepen with increasing ion fluence.

Now remind that the trapping sites such as defect formed a high D concentration zone as reported previously [24]. Then if it can be determined where oversaturation is overcome the solubility limit, the oversaturation induced defect is easily observed. Practically the solubility limit in ion irradiated in W is difficult to estimate. Theoretically, the oversaturation limit as well as hydrogen concentration in lattice sites C can be obtained from Sievert's law [32], where k is the solubility of the hydrogen, and p is hydrogen pressure to solid surface. However, p is non-measurable value from experiment, so the theoretical expectation of C is only available. Regardless of that difficulty, the critical region can be obtained from the experimental observation such as the hydrogen depth profile data taken from SIMS. Figure 4-4 (d)-(f) show the converted deuterium concentration in tungsten which was calculated for standard SIMS yield for deuterium to tungsten matrix as described in equation (4.1).

$$C_D[\text{fraction}] = \frac{RSF_D}{RSF_W}\frac{I_D}{I_W} \quad (4.1)$$

where RSF_D and RSF_W is relative sensitivity factor (*RSF*) of deuterium and tungsten in SIMS, respectively. I_D and I_W represent SIMS intensity. The used *RSF* ($RSF_D \sim 4.3 \times 10^{23}$, $RSF_W \sim 6.25 \times 10^{24}$ [33]) of SIMS are not absolute value because it depends on material fabrication. Thus, only relative amount will be compared in this section. For 0.5×10^{25} D/m^2, no distinguishable subsurface peak was observed, and the D concentration is low which is about 10^{-2} *at.%*. It implies that the accumulated deuterium is not to form oversaturation zone in tungsten because solubility limit of D_2 in tungsten. However, for 2.0 and 4.0×10^{25} D/m^2, the peaked high deuterium concentration (10^{-1}) observes clearly near 15-16 nm as shown in Figure 4-4 (b) and (c). Remind that the depth is far beyond the expected ion implant range (1.6 nm). Because the theoretical expectation in previous literature suggest that the oversaturation can be occur for over certain concentration such as a few 10-10^{-4} *at.%* for 700-800 K, observed difference in deuterium concentration in tungsten can be evidence of oversaturation occurrence. The peaked shape also supports the evidence.

Figure 4-5 shows clearly the oversaturation depths for various deuterium fluences which are acquired from fits to the data. The error bars in the plot were obtained from the standard variance of four samples irradiated at the same time. As mentioned earlier, the high resolution of the SIMS measurement provides a low uncertainty of 0.6−1 nm. Figure 4-5 shows that oversaturation occurs approximately between 1.0×10^{25} D/m^2 and 2.0×10^{25} D/m^2. Above 2.0×10^{25} D/m^2, the depth increases very slightly with increasing ion irradiation fluence, so the maximum depth must be in the range of 16 – 17 nm, which is indicated by the asymptotic dotted line in the Figure 4-5. More investigations are required to determine the exact value of the threshold for oversaturation and the exact value of the saturation depth.

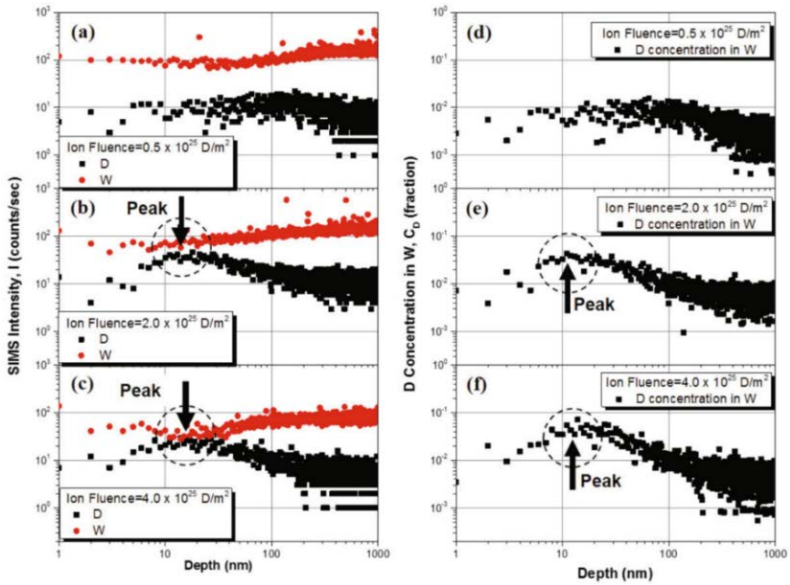

Figure 4-4. (a)–(c) SIMS raw data for deuterium-ion-irradiated tungsten and (d)–(f) calculated concentration. (a) and (d) for 0.5×10^{25} D/m^2, (b)–(d) 2.0×10^{25} D/m^2, and (c)–(f) 4.0×10^{25} D/m^2. For (a)–(c), the black symbols represent deuterium, and the red symbols are for tungsten.

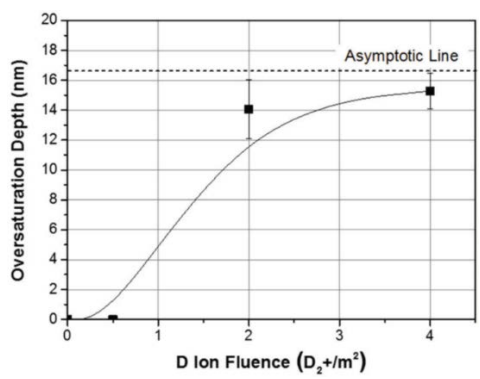

Figure 4-5. Oversaturation depth estimated from SIMS data for 0.5×10^{25} D/m^2, 2.0×10^{25} D/m^2, and 4.0×10^{25} D/m^2. The target temperature was kept at 700 K. The line represents the best fit to the data. Error bars represent the standard variance of four samples.

Figure 4-6 shows the TDS spectra for tungsten irradiated with fluences of 0.5×10^{25} D/m^2, 2.0×10^{25} D/m^2 and 4.0×10^{25} D/m^2. As mentioned in the experimental section, the Redhead approximation of equation (3.1) was adapted to determine desorption energy (E_{des}) and a binding energy (E_s) from the TDS peak temperature (T_p). For the fluence of 0.5×10^{25} D/m^2 in Figure 4-6, D_2 desorption was negligible, so no trapping sites and no oversaturation-induced defects occurred. In addition, no distinguishable peak regions in the SIMS spectra of Figure 4-4 (a) and (d) were measurable. When the TDS spectrum in Figure 4-6 for 0.5×10^{25} D/m^2 was compared to that for 2.0×10^{25} D/m^2, an increase in retention was observed, which implies that a sufficient D ion fluence forms a solution in defect-free tungsten. The corresponding peak temperature and desorption energy are 462 K and 0.89 eV, respectively. However, the SIMS results in Figure 4-4 (b) and (e) show peaked regions, which imply oversaturation. Thus, we can deduce the presence of oversaturation-induced vacancy generation in 2.0×10^{25} D/m^2 irradiated W. For a more detail analysis, TDS deconvolutions for 2.0×10^{25} D/m^2 and 4.0×10^{25} D/m^2 were performed, and the results are shown in Figure 4-7 (a) and (b).

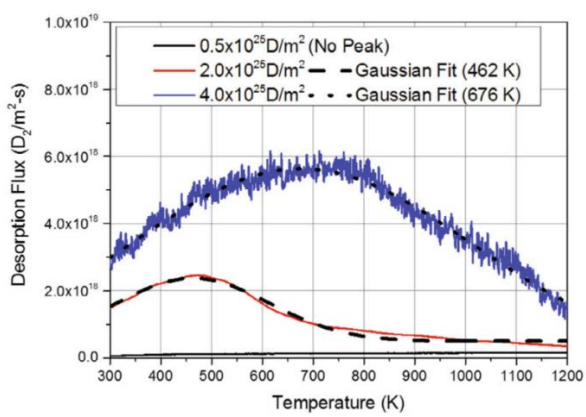

Figure 4-6. TDS spectra of deuterium-ion irradiated tungsten: 0.5×10^{25} D/m^2 (black solid line), 2.0×10^{25} D/m^2 (red solid line), and 4.0×10^{25} D/m^2 (blue solid line). The dashed line and the dotted line represent Gaussian fits.

Figure 4-7 shows the TDS peak deconvolutions obtained by using a Gaussian fitting for the first-order desorption peak. A comparison of 2.0×10^{25} D/m^2 in figure 20 (a) to 4.0×10^{25} D/m^2 in Figure 4-7 (b) shows a clear transition of retention from solution-dominant retention to vacancy rapping-dominant retention. While the case of 2.0×10^{25} D/m^2 in Figure 4-7 (a) shows a dominant solution peak at 452 K and a small vacancy trapping peak at 670 K, which correspond to E_{des} ~ 1.84 eV, the case of 4.0×10^{25} D/m^2 in Figure 4-7 (b) shows a significant peak at 680 K and a negligible solution peak at 455 K. For peaks of 670 − 680 K, E_s is about 1.45 eV and E_{des} is about 1.84 eV. Note that the value of E_s is relevant to the known value of the vacancy-D binding energy ($E_b = E_s$ = 1.45 eV [21]). Therefore, the defect type generated due to oversaturation is obviously a vacancy and its formation is proportional to the D fluence. This implies that oversaturation-induced defect generation is a dominant retention mechanism for W irradiated with low energy ions (lower than the energy of the cascade collisional damage threshold, ~250 eV). For the plasma facing W in a fusion reactor, oversaturation needs to be considered in the development of a basic retention estimate model for steady-state and long-term operations before additional damage, such as self-ions and neutrons, are considered.

In conclusion of section 4.2, the oversaturation was observed as a cause of change of volume retention reactions in tungsten irradiated by deuterium plasma. The experimental evidences of deuterium oversaturation were found with oversaturation depth, ion-fluence dependency, and induced defect type. SIMS results show that the oversaturation depth was formed at deeper region than ion implantation range (1.6 nm for 100 eV/D_2^+) during the irradiation, which has threshold-like property near 1.0-2.0 x 10^{25} D_2/m^2 and ion-fluence dependency as 15-16 nm for 2.0-4.0 x 10^{25} D_2/m^2. The result implying that oversaturation may dominate retention for low ion energy condition (< cascade collisional damage threshold, ~250 eV) such as low T_i in far-SOL fusion plasma during long-term operation. For the conditions, TDS analysis reveal that the oversaturation-induced defect type is vacancy because the measured desorption temperature is

relevant to desorption energy (E_s=1.84 eV) of D to vacancy. Thus, the retention reactions under deuterium plasma are consist of deuterium solution ($E_{des,0}$=0.75-0.95 eV), and oversaturation-induced vacancy trapping ($E_{des,1}$=1.84 eV). These two volume retention reactions are intrinsic reaction of hydrogen retention because they can be formed under deuterium plasma only.

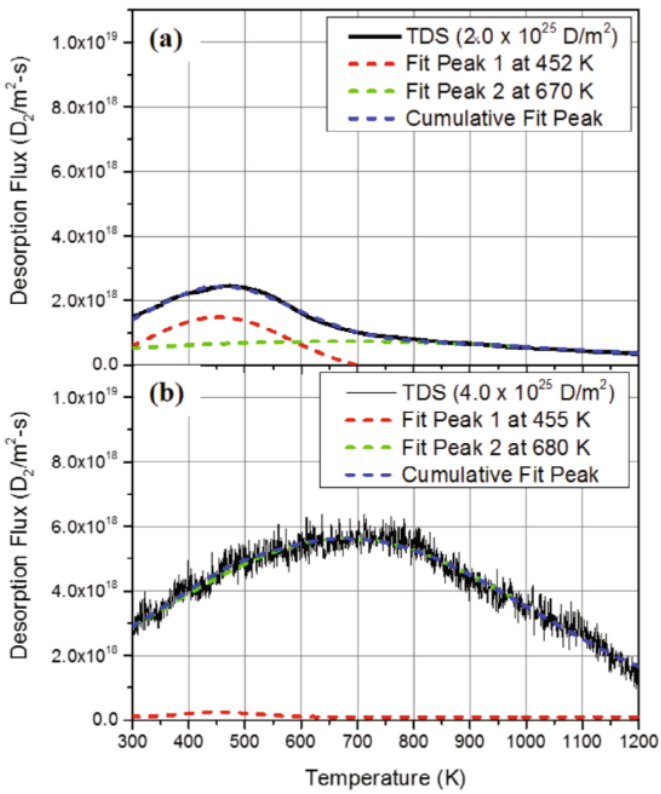

Figure 4-7. (a)–(b) Deconvolution of TDS spectra for deuterium-ion-irradiated tungsten. (a) is for 2.0 × 10^{25} D/m^2 ion fluence: 451 K (red short dashed line), 650 K (green short dashed line), and the cumulative fit peak (blue short dashed line). A Gaussian fit is adapted to obtain the fit line for each TDS peaks. (b) is for 4.0 × 10^{25} D/m^2 ion fluence: 455 K (red short dashed line), 680 K (green short dashed line), and the cumulative fit peak (blue short dashed line).

4.3 Chemical impurity-induced long-term volume retention: impurity chemical trapping ($E_{des,2}$)

4.3.1 **Introduction**

To investigate chemical impurity-induced extrinsic volume retention reaction, TDS experiment was performed for the condition of deuterium plasma exposure onto carbon-implanted tungsten.

In the case of fusion reactor which has hydrogen isotopes as fuel gas, radioactive tritium retention in chamber wall is main safety concern [34]–[36]. This phenomenon has possibility of enhancement under deuterium plasma including reactive chemical impurity, which can be generated because of plasma-wall interaction (PWI) such as sputtering and erosion. Specifically, JET ITER-Like Wall experiment (JET-ILW) have reported that increased deuterium retention in tungsten wall due to implanted and deposited beryllium impurity, which has high hydrogen affinity than tungsten. The beryllium impurity was generated from the first wall and then re-implanted onto wall via ionization and acceleration through plasma as a form of Be^{2+} [37]. In addition, KSTAR have also steadily reported that the existence of chemical impurity ion in core and scrap-off layer (SOL) plasma. The main impurity ion is carbon (C^{4+}) because of the sputtering of graphite wall during intensive plasma operation such as H-mode. Unlikely to beryllium, carbon impurity is most common impurity source in plasma system because it can be existed by natural wall contamination even though there is no carbon-based wall material. Thus, the carbon is most representative chemical impurity source in bounded plasma system. However, it does not mean the carbon is also dominant impurity source of tokamak since there can be more severe impurity source such as beryllium. But this dissertation is not only for tokamak but also for process plasma system, we can define the carbon as an impurity source in

bounded hydrogen plasma system. In terms of impurity ion's incident energy, carbon ions generally sustain their thermal energy as 300-400 eV for ELMy H-mode and 30-100 eV for ELM-suppression approaching to wall in KSTAR approaching to wall in KSTAR [38], implying possibility of impurity ion implantation on installed wall material at the same time that the fuel deuterium gas is retained. In the point of occurrence of long-term deuterium retention by reactive chemical impurity, previous researches using linear device reported that increase of hydrogen retention in tungsten proportional to carbon impurity contents [39]–[42], showing possibility of chemical impurity trapping of deuterium in chemical impurity-implanted tungsten.

Present work initiated with two propositions: 1) there can be chemical impurity trapping effect in carbon-implanted tungsten exposed to KSTAR deuterium plasma. 2) The effect of carbon impurity will depend on plasma-facing condition such as wall position (midplane/divertor) and ELM suppression because it depends on impurity transport and implantation. Thus, we organize the experiment to reveal the characteristics with the variables.

Through the overall experiment, the volume retention reactions and corresponding desorption energies will be revealed for deuterium plasma-facing tungsten with impurity ion effect.

4.3.2 **Experimental setup**

Overall experiment was performed with series procedure: 1) implantation of carbon impurity in KSTAR, 2) deuterium plasma irradiation on tungsten by ECR plasma system, 3) retention characterizing by TDS, 4) the other post-mortem analysis. As mentioned in previous part, setup for TDS is omitted.

Experiment was carried out strategically to understand the effect of chemical impurity trapping in tungsten by investigating phenomenal difference between tungsten and carbon-impurity-implanted tungsten. To investigate retention properties for both cases, carbon-impurity-implanted tungsten was prepared by installing tungsten samples using manipulator during 2016 campaign of Korea superconducting tokamak advanced research (KSTAR), which has graphite wall hence we can expect carbon-impurity implantation onto tungsten. Overall experiments are arranged in subsection and described as a flow chart shown in Figure 4-8.

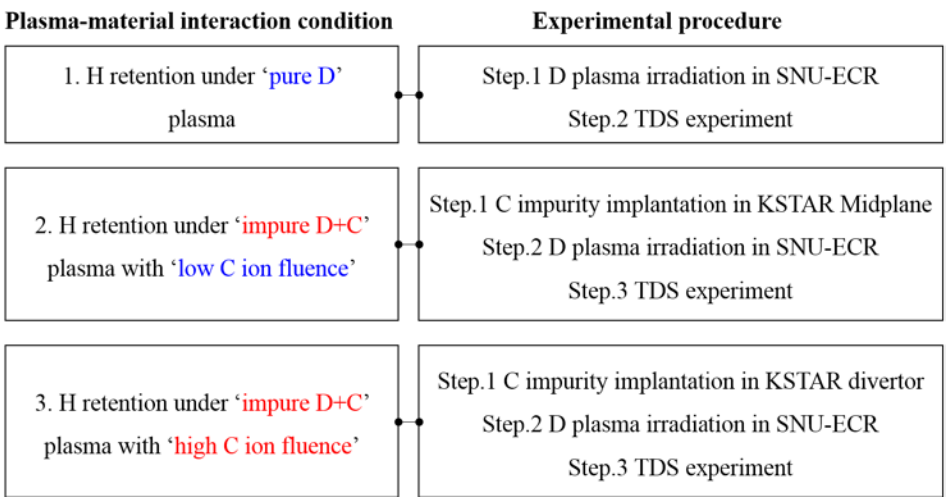

Figure 4-8. Description of simulated plasma-wall interaction condition and simulator condition during experiment.

All experiments were performed with poly-crystalline tungsten samples (ITER-grade tungsten, Plansee). All tungsten samples were mechanically polished up to roughness under 30 nm. Tungsten samples have 99.96% purity. The sample dimension is 10 mm in diameter and 3 mm in thickness, being annealed at a mid-temperature (1273 K) for 12 hours to reduce uncertainty of different initial condition that fabrication-induced defects. By polishing after annealing, the effect of rough surface resulted from annealing was also removed.

Carbon-mixed plasma irradiation was performed with KSTAR, which can provide carbon mixed plasma irradiation during operation in fusion-relevant system (midplane, divertor) because its plasma-facing material is carbon-based graphite to be sputtered and re-implanted into installed tungsten target. The purpose of experiment in KSTAR is not the deuterium retention in tokamak but the impurity implantation in tokamak. Because the experiment time is limited to accumulate plasma exposure time under similar condition, the irradiation time is too short to store enough deuterium. Expected deuterium fluence during experiment is about 8.36~12.5 x 10^{23} D/m^2 for midplane and 4.18~8.36 x 10^{24} D/m^2 for divertor. It is common limitation of experimental tokamak because they must research various subjects within finite duration of campaign. The plasma exposure of tungsten in KSTAR was performed only for a half day (30~40 shots, 200-400 secs), which time operated by same operating scenario such as ELMy H-mode or ELM-suppression as arranged in Table 4-1. Nevertheless, total ion fluence (D+C) is too less to induce sufficient deuterium retention, implanted carbon impurities amount is sufficient to make change in deuterium retention for following deuterium irradiation as shown in our following results.

The expected fraction of carbon ion per deuterium ion is several percentage reported by KSTAR experimental data. The fraction can be varied by shot to shot depending on operating condition and operation time, however, at least, carbon ion is observed for all KSTAR shots. The incident energy of carbon is about 300-400 eV for ELMy H-mode and 30-100 eV for

ELM-suppression approaching to wall in KSTAR [38]. To guarantee, higher impurity fluence onto divertor than midplane, the experiment of both midplane and divertor were performed at the same shot. Because expected total ion flux is higher at divertor, the expected carbon ion fluence is higher for divertor than midplane nevertheless the exposure time is same.

For that experiment, tungsten samples were installed in KSTAR by using two manipulator systems as shown in Figure 4-9 [43]. To compare different plasma irradiation condition, which can be effective variables for chemical impurity flux to wall: The one was installed at midplane located at the position distant from last-closed flux surface (LCFS) by 10 cm, the other was installed at divertor located near strike point. We can expect more impurity flux at divertor since the transport rate is higher for parallel field transport than cross-field transport [44]. Samples were exposed to the same plasma operating condition, simultaneously. The other distinguishable conditions are ELMy H-mode experiment and ELM-suppression experiment hence it can be compare with ELM effect on implantation of chemical impurity ion onto tungsten samples at wall. In terms of experimental variables, ELM makes insignificant difference in incident ion energy but clear difference in incident ion fluence during same time according to the charge exchange spectroscopy (CES) results of KSTAR for carbon ion [38]. Nevertheless, the ion energy is different for ELM conditions (ELMy H-mode: 300-400 eV, ELM-suppression: 30-100 eV), the ion energy was not considered as main variables because it is not the cause of deuterium retention change when the energies are lower than threshold of cascade collisional damage of tungsten by carbon. Hence, we only expect that the difference of incident impurity ion fluence between ELMy H-mode and ELM-suppressed H-mode plasma in KSTAR. Because the effect of ion incident energy was considered when we discuss implanted depth of ion, the difference of ion incident energy will be discussed with SIMS data, indirectly. The shot information for two different H-mode plasma conditions were obtained by KSTAR shot data as shown in Figure 4-10. To distinguish ELM-suppression condition, D alpha

signal was obtained by KSTAR team using filter scope as a typical diagnostic [45], [46]. The ELM-suppression shot show suppressed D alpha (656.28 nm) signal in the figure. Sample temperature was assumed as comparable to near tile temperature. Near tile temperature was measured by directly-connected thermo-couple located at 5 mm distance from tile surface. For quantitative analysis, edge plasma condition near sample positions are arranged as shown in Table 4-1 and Table 4-2 according to previous reports of KSTAR [38], [47], [48].

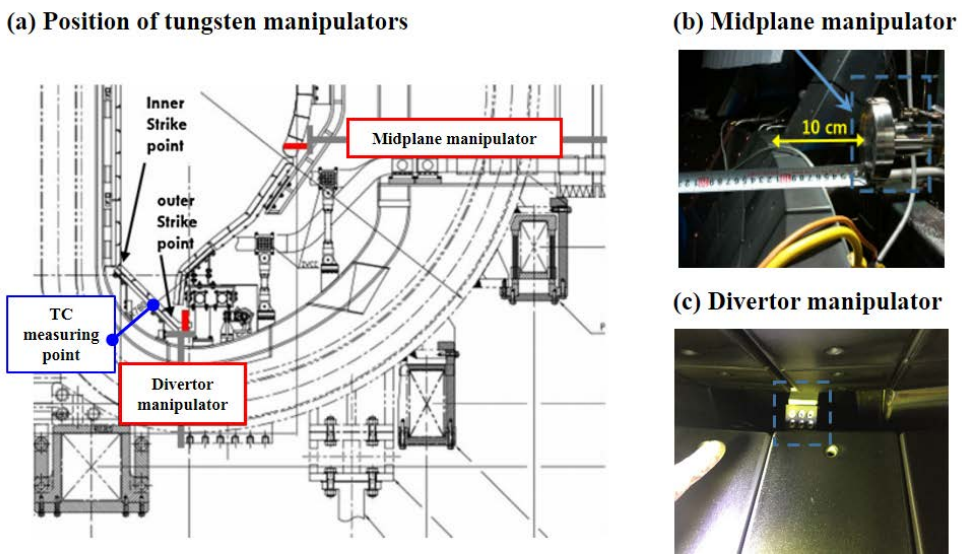

Figure 4-9. Schematic and photos for sample installation: (a) position of tungsten manipulators in KSTAR, (b) midplane manipulator, (c) divertor manipulator.

Table 4-1 Edge plasma condition near manipulator.

Property	**Condition**	
	Midplane	**Divertor**
Ion flux	2~3 x 10^{21} /m^2-s	1~2 x 10^{22} /m^2-s, ~10^{24}
	for ELMy H-mode	for ELMy H-mode [49]
	2~3 x 10^{20} /m^2-s	1~2 x 10^{21} /m^2-s, ~10^{24}
	for ELM-suppression	for ELM-suppression
Expected total	210~330 sec (~30 shot x 7~11 sec)	210~330 sec (~30 shot x 7~11 sec)
exposure time	for ELM-suppression	for ELM-suppression
	210~330 sec (~30 shot x 7~11 sec)	210~330 sec (~30 shot x 7~11 sec)
	for ELMy- H-mode	for ELMy- H-mode
Expected total D ion	8.36~12.5 x 10^{23} D/m^2	4.18~8.36 x 10^{24} D/m^2
fluence	for ELMy H-mode	for ELMy H-mode
	8.36~12.5 x 10^{22} D/m^2	4.18~8.36 x 10^{23} D/m^2
	for ELM-suppression	for ELM-suppression
D and C ion incident	300-400 eV/D+ (Ψ_i=85°) [12]	Assumed as
energy	for ELMy H-mode	ELMy H-mode > ELM-suppression
	30-100 eV/D^+ (Ψ_i=85°)	
	for ELM-suppression	
	($E_i = E_{i,thermal} + E_{i,sh} + E_{i,tor}$)	
Temperature during	300-400 K	>300 K [43], [47]
operation		dep. on shot time

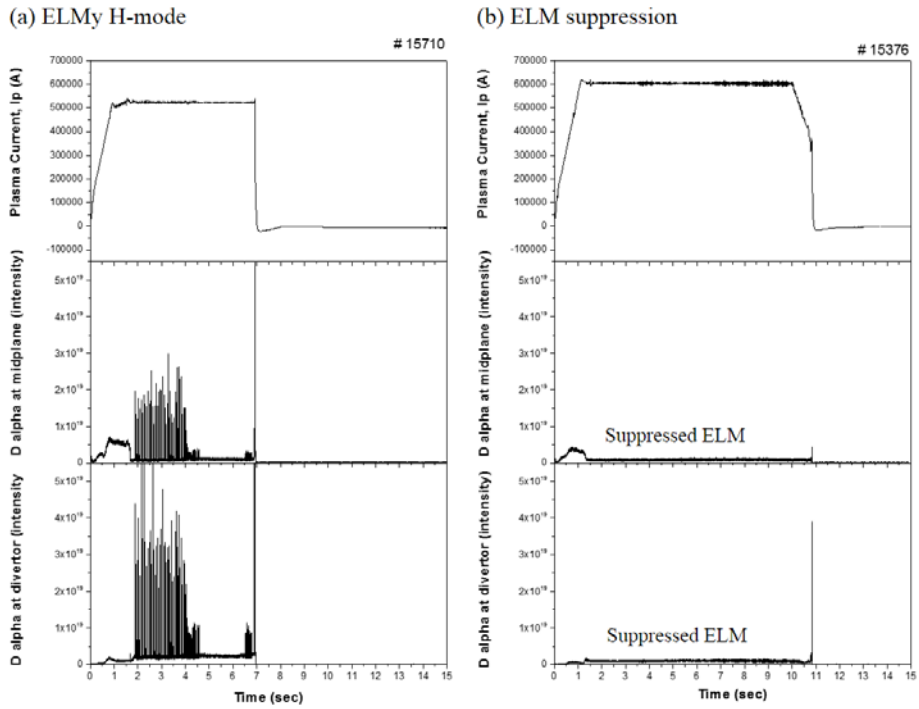

Figure 4-10. KSTAR shot information obtained during KSTAR 2016 campaign. The figures show shot of two different H-mode plasma condition including plasma current, D alpha signal from midplane channel, D alpha signal from divertor channel. (a) ELMy H-mode and (b) ELM-suppression condition.

Table 4-2 KSTAR shot information for present work.

Shot number, #	Shot characteristic	Wall temperature
15341-15379	H-mode plasma with suppressed ELM	Divertor: > 400 K Midplane: 300-400 K
15687-15721	ELMy H-model	Divertor: > 400 K Midplane: 300-400 K

Deuterium plasma irradiation onto tungsten was carried out with lab-scale electron cyclotron resonance plasma system of Seoul national university (SNU-ECR) after implantation of carbon impurities under carbon-mixed deuterium plasma of KSTAR. Tungsten samples were irradiated by deuterium plasma source with higher fluence (~10^{25} D/m^2) than KSTAR exposure (10^{23}~10^{24} D/m^2) to measurable retention amount in tungsten. The electron density and the temperature of the deuterium plasma near the target were measured by using a Langmuir probe and were estimated as 3.4 x 10^{17} m^{-3} and 5 eV, respectively. The ion flux on the tungsten target, which meets the Bohm flux condition [28], was analyzed as 2.8 x 10^{21} D_2^+/m^2s. The value is relevant to the ion flux of ~10^{21} D+/m^2s on the first wall of KSTAR [29]. Because the ion energy is proportional to the sheath potential, ~ 3.3 times the electron temperature T_e, the ion energy at KSTAR's first wall is estimated as ~55 eV/D+ for the measured electron temperature of ~ 17.5 eV [29]. Overall condition of plasma exposure in SNU-ECR is arranged in Table 4-3. All tungsten samples were irradiated with deuterium ion fluence of 4 x 10^{25} D/m^2. During exposure, the target temperature was fixed near 700 K by cooling system.

Table 4-3 Plasma exposure condition of SNU-ECR

Exposure condition	Value
Plasma density	~ 3.4 x 10^{17} #/m^3
Electron temperature	~ 5 eV
Incident ion energy	~ 100 eV/D_2+
Ion incident angle	90˚ (Normal direction)
Ion flux	~ 2.8 x 10^{21} D_2+/m^2-s
Ion fluence (exposure time)	~ 4.0 x 10^{25} D_2/m^2 (14400 sec)

4.3.3 **Impurity-induced volume retention reaction and corresponding desorption energy**

Implantation of chemical impurity was investigated indirectly with material analysis from surface to subsurface because the implantation profile is the trace of impurity implantation phenomenon. Tungsten samples irradiated by KSTAR deuterium plasma was firstly observed using FESEM to investigate changes of surface. Figure 4-11 shows the images for all samples with non-irradiated tungsten sample as a reference. For the tungsten installed at midplane, there is no remarkable difference on surface with respect to tungsten nevertheless plasma and carbon may be implanted onto tungsten. This observation implies there is change in subsurface rather than surface. Which implies that the ion implantation should be considered rather than co-deposition to understand the change of condition in subsurface. However, there is obvious difference on tungsten sample installed at divertor. Trace of carbon deposits on surface was observed for both of divertor sample. To investigate whether the samples are implant-dominant condition or deposition-dominant, energy-dispersive X-ray spectroscopy (EDS: Bruker, XFlash6) that is equipped at FESEM was applied on tungsten surface. Figure 4-12 shows the results of element fraction with weight percentage (*wt.%*) along tungsten (W), carbon (C), oxygen (O). It shows the results of element fraction with weight percentage (wt.%) along tungsten (W), carbon (C), oxygen (O). The tungsten data was measured just after surface polishing up to under 30 nm without installing into KSTAR, which shows lowest impurity concentration including carbon (~1%) and oxygen (~1%). While midplane samples show relatively lower carbon fraction, divertor samples show increased carbon up to 5 wt.%. These observations may indicate higher carbon impurity flux onto divertor samples than midplane samples regardless of same expose time during same shot.

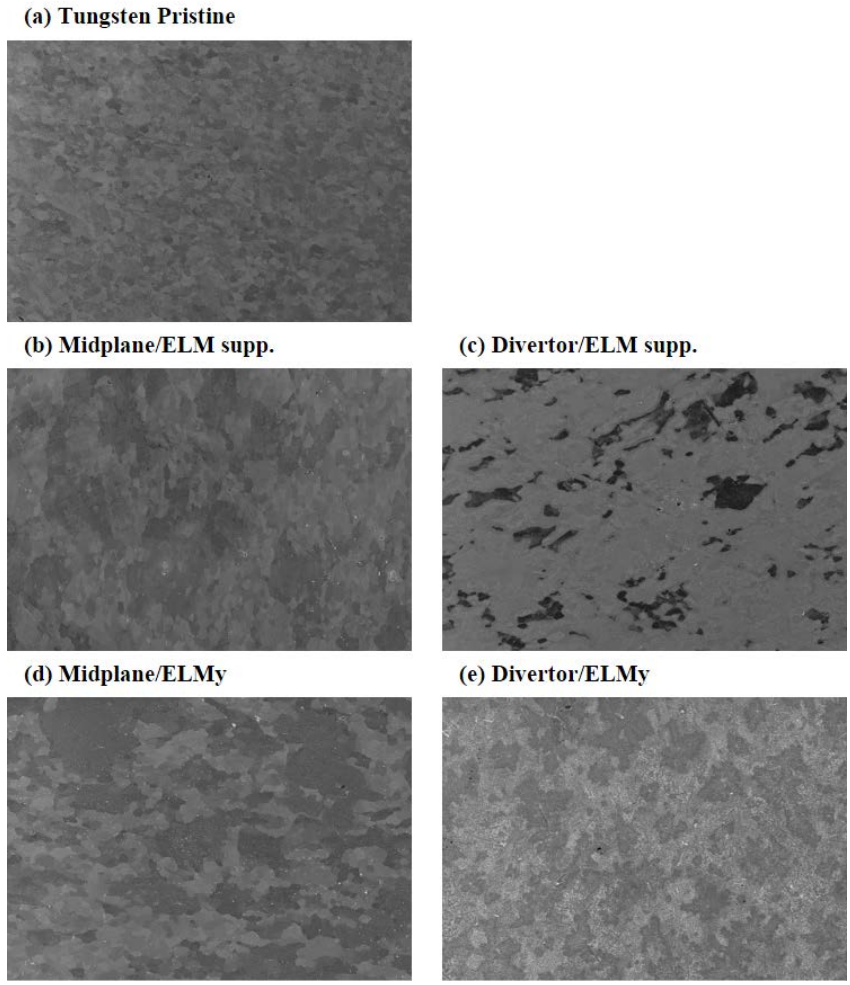

Figure 4-11. FESEM images for surface of all tungsten samples installed at KSTAR manipulator during 2016 campaign. (a) Tungsten pristine which is not irradiated by plasma, (b) Sample at midplane during ELM-suppression condition, (c) Samples at midplane during ELMy H-mode condition, (d) sample at divertor during ELM-suppression condition, (e) samples at divertor during ELMy H-mode.

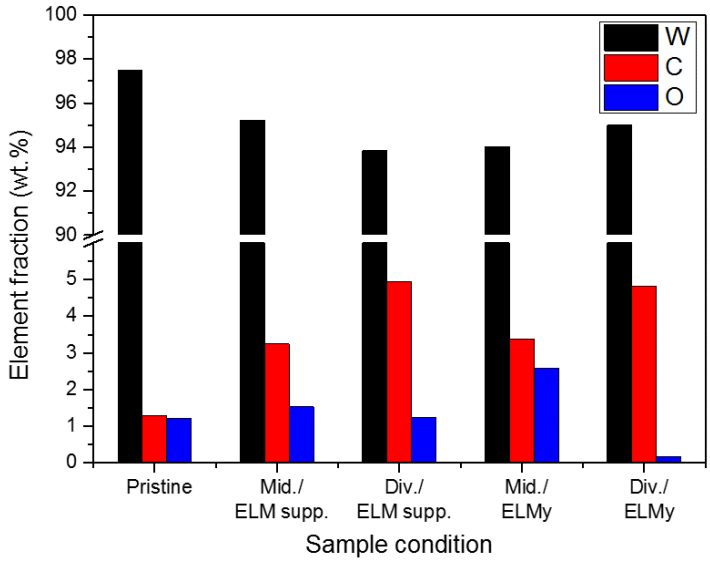

Figure 4-12. EDS data for surface of all tungsten samples installed at KSTAR manipulator during 2016 campaign. (a) Tungsten pristine which is not irradiated by plasma, (b) Sample at midplane during ELM-suppression condition, (c) Samples at midplane during ELMy H-mode condition, (d) sample at divertor during ELM-suppression condition, (e) samples at divertor during ELMy H-mode.

Table 4-4. KSTAR shot information for present work.

Shot number, #	Shot characteristic	Wall temperature
15341-15379	H-mode plasma with suppressed ELM	Divertor: > 400 K Midplane: 300-400 K
15687-15721	ELMy H-mode	Divertor: > 400 K Midplane: 300-400 K

To investigate subsurface change of tungsten samples, XPS analysis was performed as depth profiling from the surface (0 nm) to subsurface (60 nm). Figure 4-13 (a)-(c) show XPS spectra for tungsten irradiated by deuterium plasma using SNU-ECR and tungsten irradiated by D plasma of KSTAR. The spectra consist of intensity for each binding energy. The results were plotted divided into two range because carbon and tungsten are observed in different range of XPS spectra: 276-294 eV for *C1s*, 24-46 eV for *W4f*. Common characteristic in all spectra is that the subsurface near surface (0 nm) which approximately means the results from 0 nm to 10 nm show entirely different spectra with deep region (10-60 nm). The observation may indicate the change of subsurface chemistry is limited in very narrow region under 10 nm. The range like expected depth of carbon-ion implant range (~1.5nm).

Figure 4-14 (a) and (b) show corresponding peak types based on binding energy according to literature [41], [50]–[52] as arranged in Table 4-5. Considered binding types are along *C-C* (graphite, 284.2 eV), *W-W* (tungsten, 31.4 ± 0.1 eV), *W-C* (tungsten carbide, 283.1 ± 0.4 eV, 32.2 eV) and W_2C (tungsten carbide, 283.6 ± 0.2 eV, 31.8 eV), *W-O* (tungsten oxide, 36.8 eV in W4f range). Based on the Table 4-5, the binding types were classified as arranged in Table 4-6 for all samples. The table show that tungsten samples irradiated in KSTAR show *C-C* bond and *W-C* bond nevertheless the sample is tungsten. The observation firstly indicates the existence of carbon in tungsten. Existence of *C-C* even indicate fluent carbon, which can form graphite like bulk carbon region in tungsten. *C-C* bond was observed only for tungsten samples irradiated by KSTAR plasma during ELMy H-mode condition. Furthermore *W-C* bond in clearly formed in carbon-impurity-implanted tungsten as an evidence of sp^2 hybridization of tungsten subsurface. These overall results imply two possibilities: 1) carbon impurity was implanted into tungsten nevertheless fusion plasma is hydrogen plasma, 2) The condition of plasma-facing material could be changed by chemical impurity ion implantation. One thing clear in this section is that the implanted carbon impurity change chemistry in subsurface of

tungsten during KSTAR operation. The effect of this carbon impurity on deuterium retention will be discussed in next part using TDS results for the all samples.

Table 4-5. Binding energy of carbon and tungsten system.

Bind type	**Binding energy [eV]**		**Reference**
	C1s	*W4f*	
Graphite carbon (*C-C*)	284.2		[51]
Disordered carbon (*C*)	285.2 ± 0.1		[41], [51]
W-C	283.1 ± 0.4	32.2 ± 0.1, 32.2 ± 0.1 34.3 ± 0.1	[41], [51]
W_2C	283.6 ± 0.2	31.8	[41], [51]
W-W		31.4 ± 0.1,33.6 ± 0.1 35.6 ± 0.1	[51], [52]
W-O		36.8	[50]

Table 4-6. Classification of bind type in different W-C-D system.

Condition	***C-C***	***C***	***W-C***	***W_2C***	***W-W***	***W-O***
	(Graphite)				**(Tungsten)**	
Tungsten under D plasma		O			O	O
Midplane during ELM-suppression	O				O	O
Midplane during ELMy H-mode	O		O	O	O	O

(a) Tungsten under pure D plasma

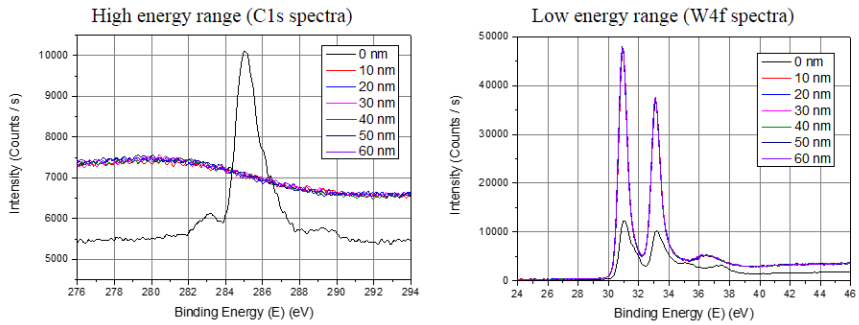

(b) Midplane during ELM-suppression

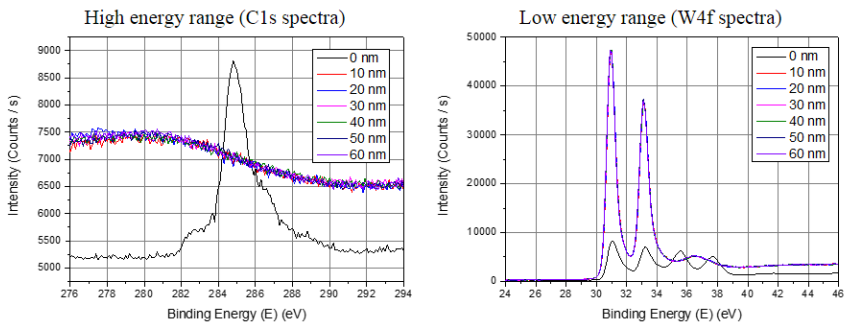

(c) Midplane during ELMy H-mode

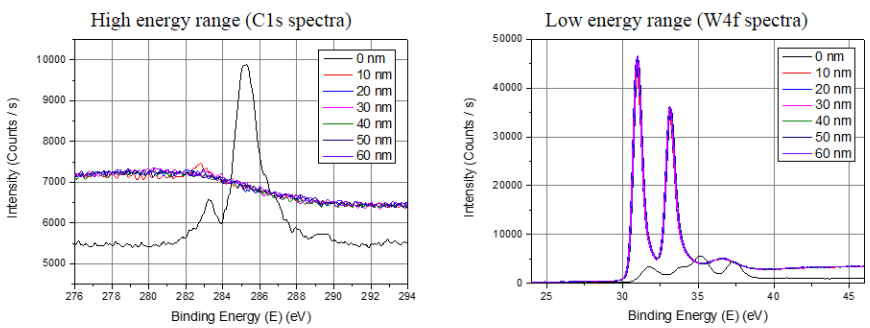

Figure 4-13. XPS raw spectra with depth-dependent data from surface (0 nm) to 60 nm: (a) tungsten under deuterium plasma, (b) tungsten samples at midplane during ELM-suppression condition, (c) tungsten samples at midplane during ELMy H-mode.

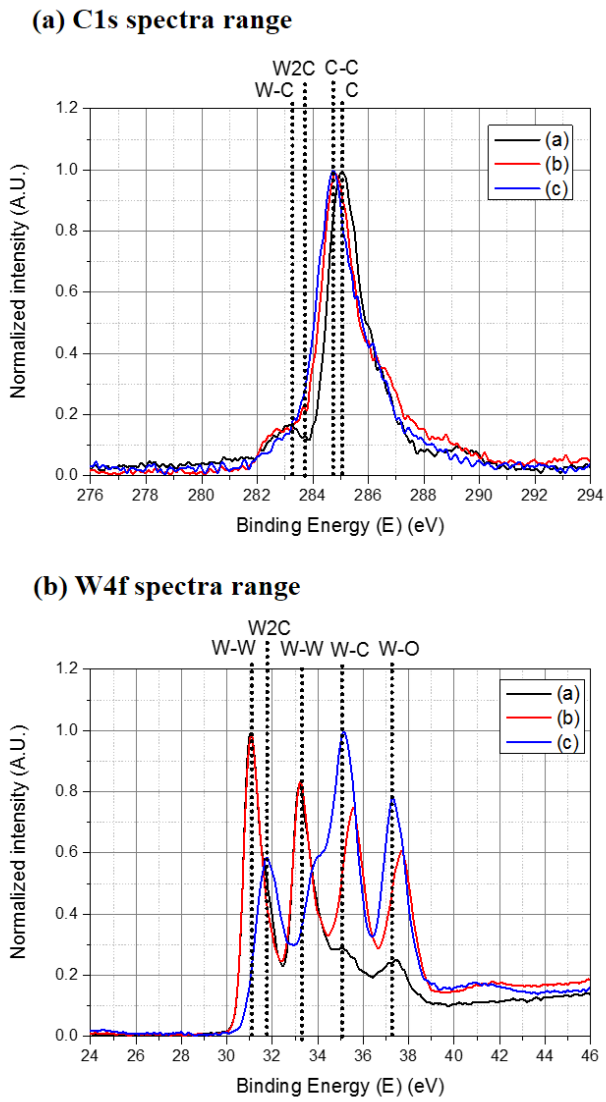

Figure 4-14. XPS spectra at subsurface (<10 nm) for all samples with indication for each chemical binding according to XPS binding energy data. The figure includes different tungsten condition with carbon impurity: (a) tungsten, (b) tungsten installed at midplane during ELM-suppression, (c) tungsten installed at midplane during ELMy H-mode.

Effect of impurity on deuterium retention in tungsten was observed as shown in Figure 4-15 (a)-(d). The figures show the TDS spectra for all samples irradiated under KSTAR D plasma with carbon-impurity implantation. When we consider detail for midplane cases ((a), (b)), significant difference between them is new peak (peak (3)) at highest temperature range (766 K) along all peaks. According to literature [18]–[20], [40], the peak temperature is not consistent to intrinsic peak in tungsten but it consistent to carbon-induced deuterium trapping (E_{des}=2.0 eV [20]) which generally observed in graphite. The observation means that the carbon impurity form *C-D* trapping in tungsten nevertheless the matrix material is tungsten. The peak area is not negligible in terms of area that means the implanted carbon significantly changes deuterium retention in tungsten. Peak area in TDS spectrum represent retention amount. The fact supports the phenomenon is resulted from implanted carbon impurity that the new peaks were formed in tungsten samples installed at ELMy H-mode of KSTAR. This characteristic is consistent to previous XPS and SIMS results. In present work, the two position represents different plasma-facing conditions as a closed-flux surface (detached from wall) and open-flux surface (attached to wall), respectively. According to Figure 4-15 (c) and (d), unlikely to midplane results (Figure 4-15 (a) and (b)), divertor show significant new peak in TDS for both ELM-suppression condition and ELMy H-mode condition. The phenomena can be explained with tokamak characteristic, which has magnetic field configuration with divertor. Contrary to midplane that faces last-closed flux surface (LCFS), divertor faces open flux surface with striking point as ‘plasma-wetted area [53]’. The open flux surface is path of impurity transport to divertor since most of impurity ionized in scarp-off layer (SOL) region [37], [54]. Hence, carbon impurities finally implant into divertor that is the reason why both cases show new peaks in TDS, not depending on ELM suppression. This is the cause of cross-contamination between plasma-facing materials from first wall to divertor. In the point of view with time scale, the phenomenon is relatively short-term phenomenon since all the results was obtained for only 1-day expose for

tungsten samples. The phenomenon can occur day-by-day regardless of wall conditioning. This phenomenon also spatially-limited phenomenon since the impurity implantation range (~nm) is very shallower than a dimension of tungsten tile (mm) of plasma-facing monoblock. The facts mean that the phenomenon will be transient since wall erosion during operation will remove the impurity-implanted tungsten layer, competing impurity implantation. When we compare it with long-term damage process of tungsten divertor in ITER, the effective damage to increase tungsten retention is at least 0.1 dpa, which is consistent to 5 months of operation [55].

In conclusion of section 4.3, chemical trapping of deuterium by implanted reactive chemical impurity was investigated as dominant volume retention reactions under plasma with impurity ions. The cause of chemical impurity trapping is the higher desorption energy of deuterium to trapping site for the case of impurity that has high hydrogen affinity. For the case of carbon as a chemical impurity source, the dominant retention reaction occurs by *C-D* chemical trapping with higher desorption energy (E_{des}=2.33 eV) than intrinsic dislocation-D trapping in tungsten (E_{des}=0.89 eV). By including the dominant retention reactions of chemical impurity trapping ($E_{des,3}$=2.33 eV), for plasma with carbon impurity ion, the volume retention reactions consist of hydrogen solution ($E_{des,0}$=0.75-0.95 eV), oversaturation-induced vacancy trapping ($E_{des,1}$=1.84 eV), implanted carbon-induced chemical tapping ($E_{des,3}$=2.39 eV).

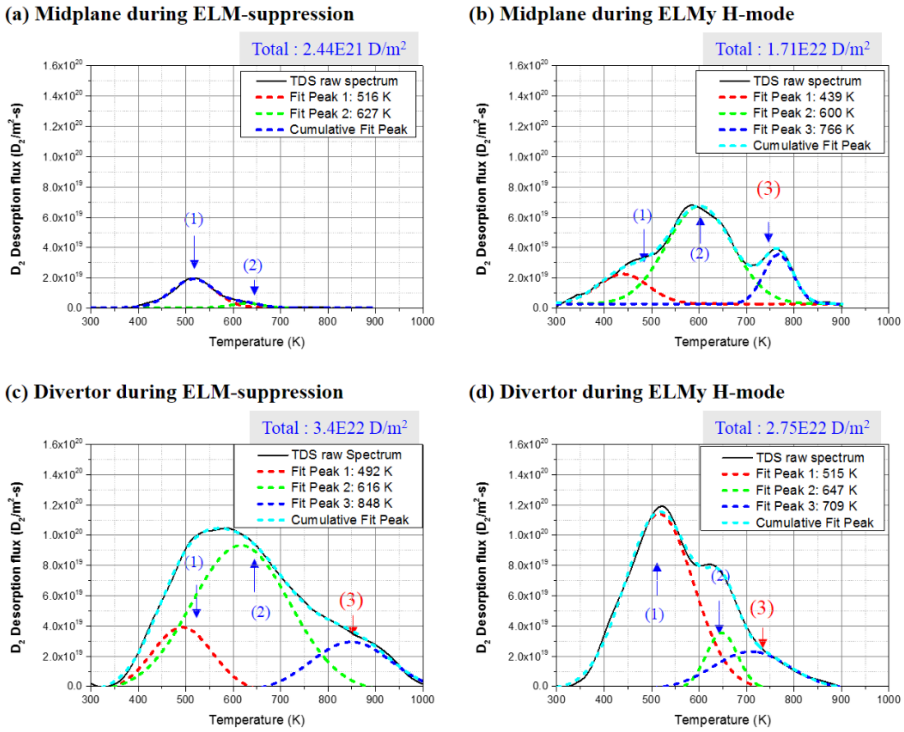

Figure 4-15. TDS spectrums for all tungsten samples installed in KSTAR during 2016 campaign. (a) Sample at midplane during ELM-suppression condition, (b) Samples at midplane during ELMy H-mode condition, (c) sample at divertor during ELM-suppression condition, (d) samples at divertor during ELMy H-mode. In figures, (1)-(3) peak indicates corresponding trapping.

4.4 Physical damage-induced long-term volume retention: defect cluster trapping ($E_{des,3}$)

4.4.1 **Introduction**

To investigate physically damage-induced extrinsic volume retention reaction, TDS experiment was performed for the condition of deuterium plasma exposure onto defect-formed tungsten.

Much research has suggested that the tritium retention in ITER will exceed the safety limit (700 g/year) before the ITER lifetime, if cascade damage totally changes the intrinsic retention properties of tungsten during operation [35], [56], [57]. From the experimental observation of the quantitative retention increment of cascade-damaged tungsten, it was known that the increase of retention is dominated by only the cascade damage itself. In fusion operation, however, the tungsten exposes to the high fuel-ions, the fast neutrons, and the self-ion irradiations, simultaneously. These several particle irradiations make increase of damage through the defects transforms into the defect clustering, resulting in the enhancement of fuel retention on the fusion plasma facing material.

Mechanism of defect clustering in the damaged metal was proposed by Foreman *et al.* [58]. The paths of defect clustering in a solid under the irradiated cascade damage are; (1) defect clustering by sufficient defect population with sufficiently high temperature for defect mobility, and (2) defect clustering by agglomeration of defect with gas particle, which is independent of temperature. For the fusion-relevant condition, the latter path is more likely to occur on the tungsten divertor where will be exposed to high fuel plasma irradiation at the mediate temperature under the re-crystallization temperature (~1,000 °C) so it draws our attention.

Some studies on the fuel gas retention enhancement by defect was carried out by using thermal

desorption spectroscopy (TDS) measurement, revealing a remarkable characteristic of retention enhancement of damaged tungsten at the highest temperature peak (~800 K) in TDS. The result is newly observed on the tungsten samples irradiated by high energy ion irradiation with following deuterium plasma irradiation. Markina *et al.* (experimental conditions: 2.0 MeV W ion irradiation, 0.9 dpa), Roszell *et al.* (100-500 eV D ion) and Hatano *et al.* (neutron, 0.3 dpa) [59]–[61] reported the existence of the highest temperature peak for the damaged poly-crystalline tungsten with a dynamically increased retention amount. It also suggests that the peak is harder to be removed than an intrinsic low energy trapping source, such as dislocation (corresponding binding energy, E_b ~ 0.89 eV) or vacancy (E_b ~ 1.45 eV). Here the highest TDS peak does not correspond to the low energy trapping of point defect. There are some remained questions on how it increases the high energy trapping of deuterium in the damaged tungsten. According to Foreman's second hypothesis, we can develop a possible scenario that the defect clustering will occur through the cascade damage agglomeration by the retained hydrogen isotope on the damage site. This also explain that the pre-formed defect would be transformed into cluster by the low energy deuterium irradiation.

This study focused on this phenomenology of defect clustering induced by fuel gas irradiation in the tungsten. In addition, we try to explain the retention increment observed at the highest binding energy to hydrogen (E_b~1.85 eV) larger than the point defects (E_b ~0.83-1.45 eV) in the previous TDS measurements. Thus, the experiments are organized to investigate the mechanism of retention enhancement on tungsten due to the agglomerated defects and, especially, the effect of the low energy-irradiated fuel gas effect on the defect clustering. For this purpose, it was chosen the grain elongated polycrystalline tungsten for which controls the grain direction with respect to the surface plane of tungsten sample that is normal to the direction of ion irradiation. In addition, the damage property was compared to the single-crystalline tungsten. The investigation of the progress of defect clustering with sequential irradiation of self-ion and

deuterium irradiation was carried out by using all-step transmission electron microscopy (TEM) analysis as described in section 2. TEM measurements were performed for ‘self-ion + deuterium ion irradiated case’ as well as ‘self-ion only irradiated case’. In section 3, the transformation of the defect by deuterium is observed near the grain boundary in the polycrystalline tungsten, discussing how it enhances the retention for the damaged tungsten and defect clustering with corresponding the highest temperature peak on the TDS observation. The dependency of grain elongation with respect to tungsten surface provides another clue to accept the Foreman’s hypothesis to form a defect clustering. Finally, the conclusion is in section 4. Through this chapter, the volume retention reactions and corresponding desorption energies will be revealed for deuterium plasma-facing tungsten with the effect of high energy ion.

4.4.2 **Experimental setup**

Overall experiment was performed with series procedure: 1) irradiation of tungsten ions onto tungsten to form lattice damage, 2) deuterium plasma irradiation on tungsten by ECR plasma system, 3) retention characterizing by TDS, 4) the other post-mortem analysis. As mentioned in previous part, setup for TDS is omitted.

The experiment was carried out strategically to understand the cause of phenomena by investigating the phenomenal difference between the self-ion effect and the deuterium ion effect. Figure 4-16 shows that TEM analysis was performed for self-ion (W^{2+}) irradiated tungsten, and both-ions (W^{2+} and D_2^{+}) irradiated tungsten. TDS measurements for damaged tungsten were performed. The experimental details are arranged in this subsection and experimental flow is summarized in the chart shown in Figure 4-16.

All experiments were performed with 3 different tungsten samples: 1) poly-crystalline tungsten with vertically elongated (named as PCW (v); ITER-grade, Plansee), 2) poly-crystalline tungsten with parallel-elongated (PCW (p); ITER-grade, Plansee), and 3) single-crystalline tungsten with (110) orientation (SCW; W 002060/6, Goodfellow). Comparison between PCW (v) and PCW (p) is done for investigating the grain elongation direction effect on defect clustering while the reference of excluding grain boundary effect provided by SCW sample. The direction is defined with respect to the top surface plane of sample according to general definition. Figure 4-17 shows the top surface of different tungsten samples and the characteristic of elongated grain boundary. All tungsten samples were mechanically polished and had 99.96% purity. The samples were prepared with 6 mm diameter and 1 mm thickness, being pre-annealed at a mid-temperature (1,273 K) for 12 hours to reduce the initial fabrication-induced defects without recrystallization.

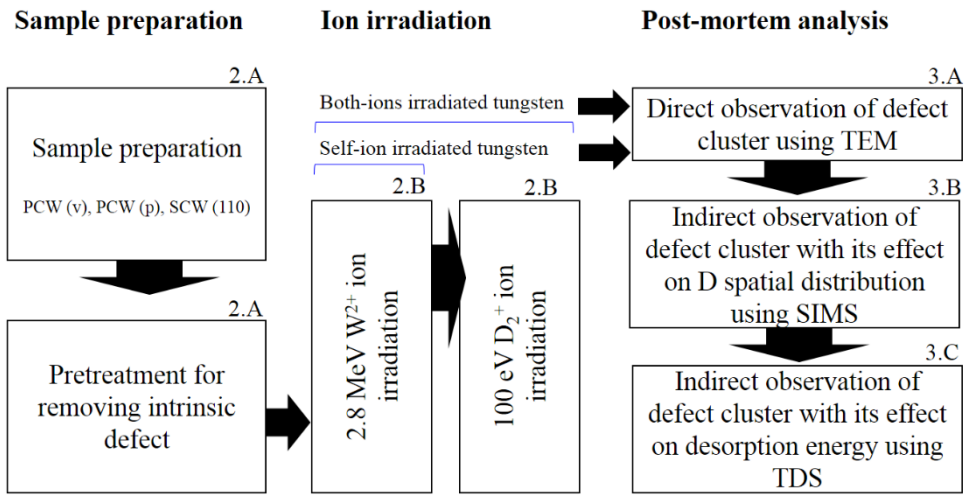

Figure 4-16. Flow chart of the present paper: sample preparation, ion irradiation, and post-mortem analysis.

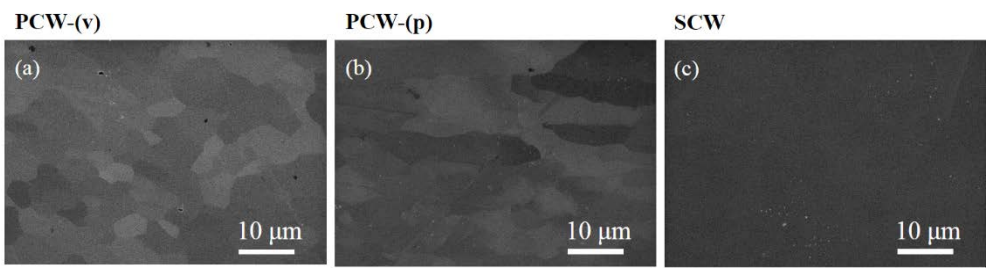

Figure 4-17. FESEM images of top surface of various tungsten samples: (a) vertically-elongated poly-crystalline tungsten (PCW (v)), (b) parallel-elongated poly-crystalline tungsten (PCW (p)), (c) single-crystalline tungsten.

Figure 4-18 (a)–(f) show the suitability of the pre-annealing condition of the present work (named as PCW-Mid T) and the unchanged average grain size (4–5 μm) with respect to the as-fabricated tungsten (PCW-non). The high temperature annealed (PCW-High T) sample shows the increased grain size up to 20–30 μm, implying crystallinity is changed by grain growth and recrystallization, not just intrinsic defect. Figure 4-18 (d)–(f) show the X-ray diffractometer (XRD; D8-Advanced, Bruker Miller Co.) measurements, estimating the relative intrinsic defects amount using full width at half maximum (FWHM) for PCW-non (FWHM=0.1131), PCW-Mid T (FWHM=0.1037), and PCW-High T (FWHM=0.0624) in 2 theta axes, respectively. The results imply that the annealing of the present work (PCW-Mid T) reduces the intrinsic defect effectively without recrystallization. XRD results commonly guarantee the depth of a few μm, due to the X-ray penetration depth in the material. Consequently, the intrinsic defect is reduced to at least a few μm scale, which is larger than the range of ion damage in present work.

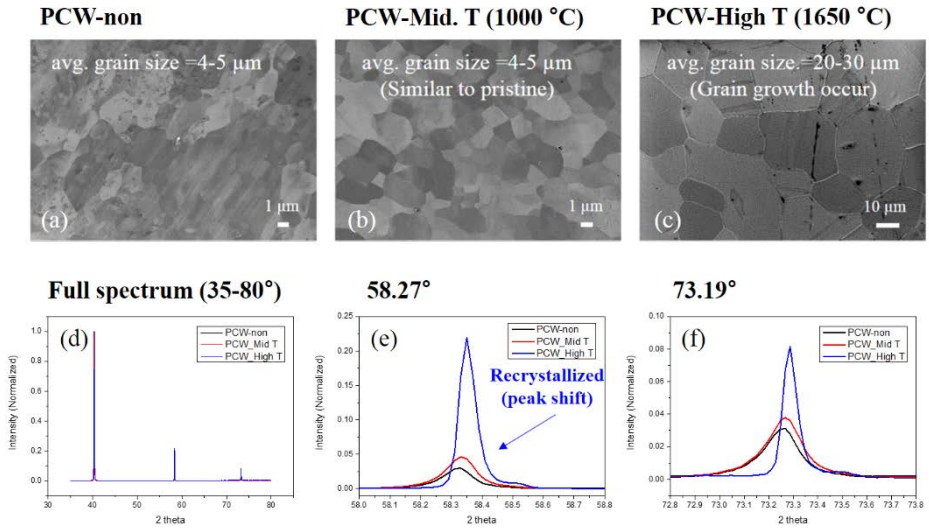

Figure 4-18. (a)–(c) FESEM imagery of the tungsten surface, and (d)–(f) XRD spectra, for pre-annealed tungsten samples and reference samples. PCW-non, PCW-Mid T, and PCW-High T stand for Polycrystalline tungsten without annealing, Polycrystalline tungsten with annealing at mid-temperature (1,000 °C), and Polycrystalline tungsten with annealing at high-temperature (1,650 °C), respectively. Note that the scale bars for (b) and (c) are different, due to the large difference of scale. XRD full spectrum (d) is represented with normalized intensity to compare the peak sharpness. Two peaks (58.27°, 73.19°) of polycrystalline tungsten are selected for relative comparison for sharpness.

W^{2+} ion irradiation on tungsten was performed using the high fluence irradiation facility (HIT) in Tokyo University. The ion irradiation causes cascade damage into tungsten without transmutation. The damage is closer to self-ion damage than neutron damage, but it indirectly causes surrogate neutron damage. Figure 4-19 shows damage value to calculate theoretical damage for the HIT experiment condition by SRIM [11] simulation. Table 4-7 summarizes the details of the simulation condition and the results.

Table 4-7. Condition and result of SRIM calculation for the HIT experiment.

Property	Condition
Irradiation ion species	W^{2+} ion
Ion energy	2.8 MeV
Incident angle	75° from surface (15° tilt from normal)
Target temperature	300 K
Damage level	0.7 dpa
Peaked damage region	150–200 nm
Defect generation rate of target displacement	70959/W Ion
Defect generation rate of target vacancies	60361/W Ion
Damage rate	0.3-0.6 [dpa/hr.] for tungsten ion current of 1-2 nA

The peak damage region is located at 150–200 nm having a point defect generation rate of displacement (70,959 displacements per *W* ion), and vacancy (60,361 vacancies per *W* ion). According to the defect generation rate per incident W ion, the damage level for 2.8 MeV W^{2+} ion irradiation was estimated as 0.7 dpa, which is comparable to the accumulated damage value of the ITER divertor for 3 years operation [58]. During W ion irradiation, the uniformity of irradiation was sustained as > 90 % and the tungsten bulk temperature was set as 300–310 K. Notes that the temperature effect on the defect formation on the target tungsten is excluded in the further investigation.

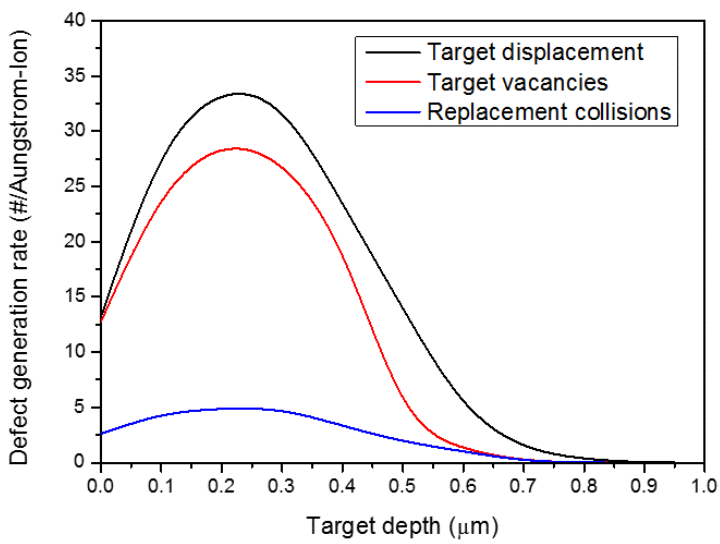

Figure 4-19. Ion-induced damage profile by 2.8 MeV W^{2+} ion calculated by SRIM-2013. The figure consists of target depth from surface along the x-axis, and defect generation number along the y-axis. The defect types are displacement and vacancy as results of Frenkel pair formation by cascade collisional damage.

After W^{2+} ion irradiation, the tungsten target samples were irradiated by deuterium ion in an electron cyclotron resonance (ECR) plasma system at an ion energy of 100 eV/D_2^+, a target bias of -87 V, and a plasma potential of 13 V in D_2^+ dominant plasma [34]. The corresponding sheath energy is 100 V, which is the energy of irradiated deuterium ion on the target. The electron density and the temperature of the deuterium plasma near the target were measured by using a Langmuir probe, estimated as 3.4 x 10^{17} m^{-3} and 5 eV, respectively. The ion flux on the tungsten target which is assumed to satisfy the Bohm flux condition, was analyzed as 2.8 x 10^{21} D_2^+/m^2s. During the deuterium-ion irradiation, the temperature of tungsten species increases due to the irradiated ion energy, but the temperature of bulk W kept controlled at 700–800 K by using an active cooling system. For a convenience, hereafter we will distinguish the self-ion irradiation only case, and the both self-ion and deuterium-ion irradiation case which called as 'self-ion irradiated tungsten (ex) PCW (v)_W)' and 'both-ions irradiated tungsten (ex) PCW (v)_W+D)', respectively.

TEM analysis is most appropriate method to observe lattice site directly and it was carried out before and after the deuterium irradiation onto self-ion damaged tungsten. To ensure no property change during sampling for TEM such as sample oxidation, the specimens were made with the focused ion beam (FIB) milling before measurement. Then measurements carried out with following standard procedure as the selected area, the focused on the cross-section of tungsten and the measured with the nearest zone axis, sequentially. To observe the different scale defects, the required resolution of TEM and STEM mode were chosen. Secondary ion mass spectroscopy (SIMS: TOF-SIMS-5, ION-TOF) was used to resolve the depth profile of the retained deuterium in the damaged tungsten. After the SIMS measurements, an alpha stepper (DXT-A, Bruker) was used to calibrate the sputtered depth.

4.4.3 **Cascade collisional damage-induced volume retention reaction and corresponding desorption energy**

The microstructural change was observed by TEM and its effect on retention as spatial distribution was investigated by SIMS. Then its desorption energies are analyzed from TDS data. Figure 4-20 (a)–(f) show high magnification TEM images for the undamaged poly-crystalline tungsten and the self-ion irradiated poly-crystalline tungsten (PCW (v) _W): (a)–(b) undamaged PCW (v) and (c)–(d) self-ion irradiated PCW (v), respectively. The images show both bright-field image (BF) and dark-field image (DF). In general, the bright region in DF TEM images can represent the vacancy or the vacancy cluster because the vacancy region has higher transmittance than the tungsten intrinsic lattice. Figure 4-20 (e)–(f) shows the vacancy loops having a shape of sliced circles. Notes that the FIB damage occurs as circular shapes, which may come from the focused ion beam (FIB) milling for TEM sampling. Evidently, there is no noticeable vacancy loop observed in the undamaged PCW (v). The images of PCW (v)_W show vacancy loops in the shape of sliced circles near the grain boundary which developed from the point defects such as free vacancy by transforming into loop near grain boundary.

Figure 4-21 (a) and (b) show the low magnification TEM imagery of PCW (v) for the self-ion irradiated tungsten (PCW (v) _W) and both-ions irradiated tungsten (PCW (v) _W+D). Because the scale of defect cluster as a form of vacancy cluster is much larger than the point defect, low magnification images are more appropriate to observe defect clusters, unlike point defects or loops. From the high magnification of TEM, the bright region in BF images is easily recognized the difference between PCW (v) _W and PCW (v) _W+D. Figure 4-21 (a) of PCW_W shows the dislocation but no clear cluster formation. Figure 4-21 (b) of PCW (v) _W+D shows clear vacancy cluster. Notes that the position of the vacancy cluster is near the grain boundary. The depth of 100–200 nm from the surface is consistent with the peak region

of the 2.8 MeV W self-ion induced cascade damage (100–200 nm).

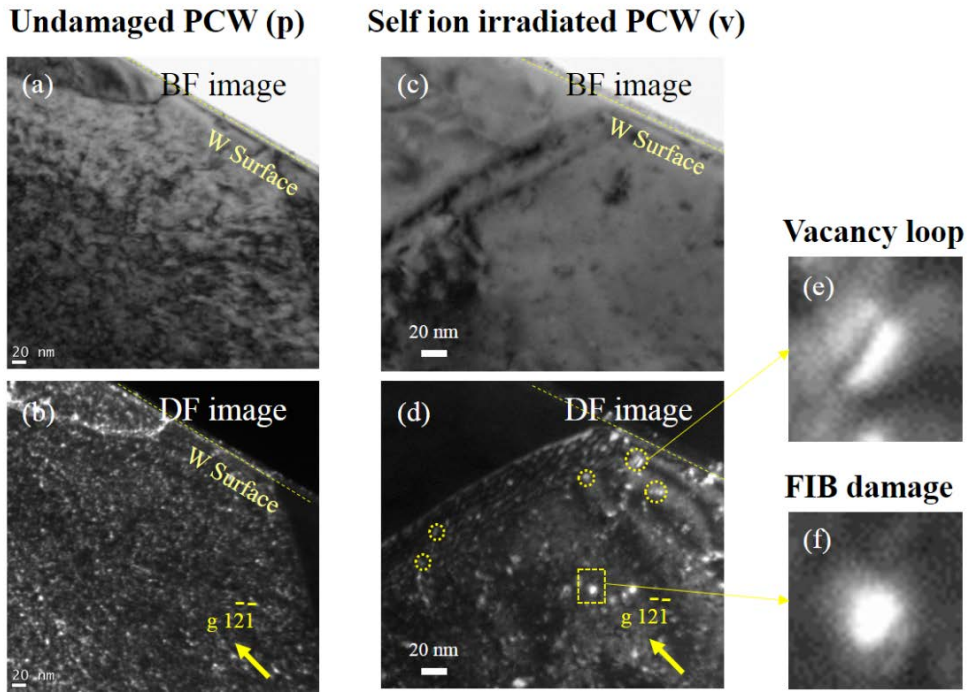

Figure 4-20. High magnification TEM imagery of PCW (v) cross-section: (a)–(b) undamaged PCW (v), and (c)–(d) Self-ion irradiated PCW (v). (a) and (c) are bright-field (BF) images, while (b) and (d) are dark-field images. (e) and (f) show amplified images of shapes of a vacancy loop and FIB damage in (d). Yellow dashed-line indicates the surface of tungsten samples.

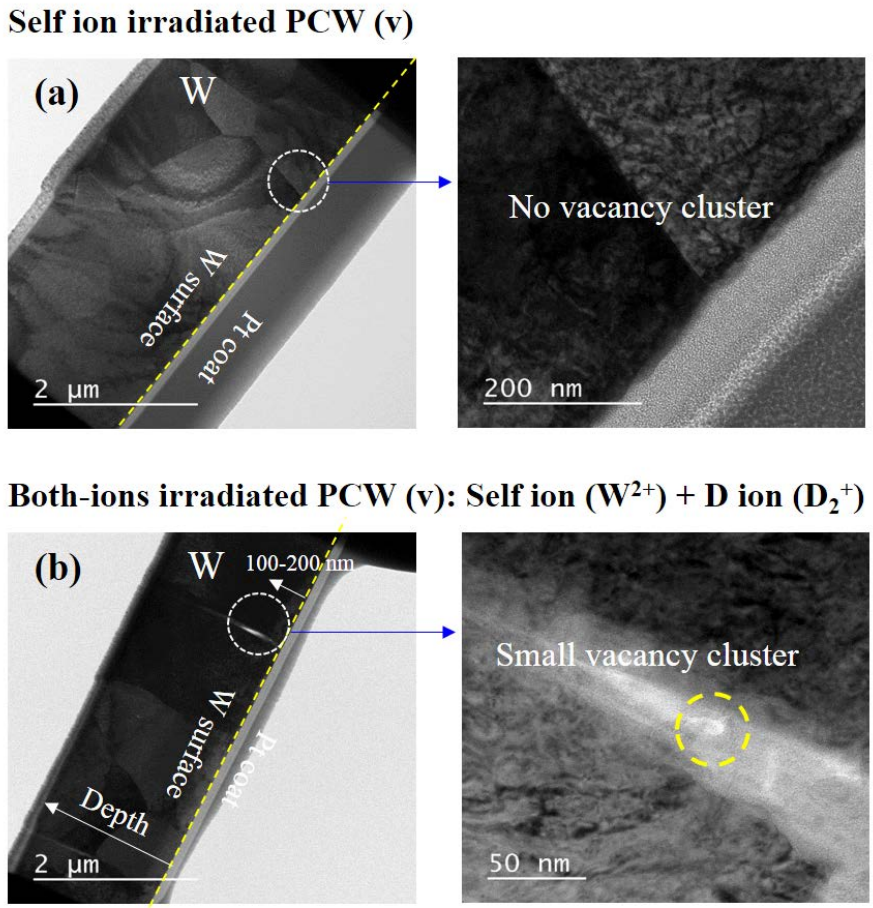

Figure 4-21. Low magnification TEM images of PCW (v): (a) PCW (v)_W, and (b) PCW (v)_W+D. Dashed circles indicated the magnified region where there is a defect cluster.

Here we consider cause of defect clustering on the both-ions irradiated poly-crystalline tungsten. The region of defect clustering is observed near the grain boundary, expecting that the diffused deuterium from the grain boundary contribute to clustering of defects. Self-ion irradiation damage contributes to inducing the formation of point defects (Frenkel pair = vacancy + interstitial) which has dispersed distribution and the peaked damage region in depth, without dependency of grain boundary. This point defect is immobile because the defect such as vacancy is immobile under 900 K [62]. Remind this temperature is higher than the self-ion irradiation condition (300K) and deuterium irradiation condition (700-800 K). Then point defects near grain boundary form loop as a group of vacancy because the grain boundary provides potential well where point defects can agglomerate easily. However, the loop is not a complete defect cluster and it only increase the size of cascade defect. For the condition of introducing the deuterium irradiation, its concentration easily increases near the grain boundary region rather than grain lattice site and it diffuses into the grain because the activation energy for diffusion is higher at the grain boundary (E_a=0.39-0.4 eV [63]) than at the grain lattice site (E_a=0.25 eV [63]). Then at the region near grain boundary, the defect loops are existed, and the deuterium is concentrated. When deuterium concentration is sufficient, the agglomeration between loop and deuterium makes the defect cluster as following the Foreman's hypothetic path. It can explain why the defect clustering occurred near the grain boundary not in the bulk lattice of tungsten. This scenario depicts in Figure 4-22. Notes that this defect clustering occurred by agglomeration between concentrated deuterium and immobile defect loop at a low temperature condition. Thus, the threshold of deuterium-defect agglomeration will be dominated by the incident deuterium fluence and the given defect population and this deuterium-defect agglomeration becomes important in the long-term plasma operation.

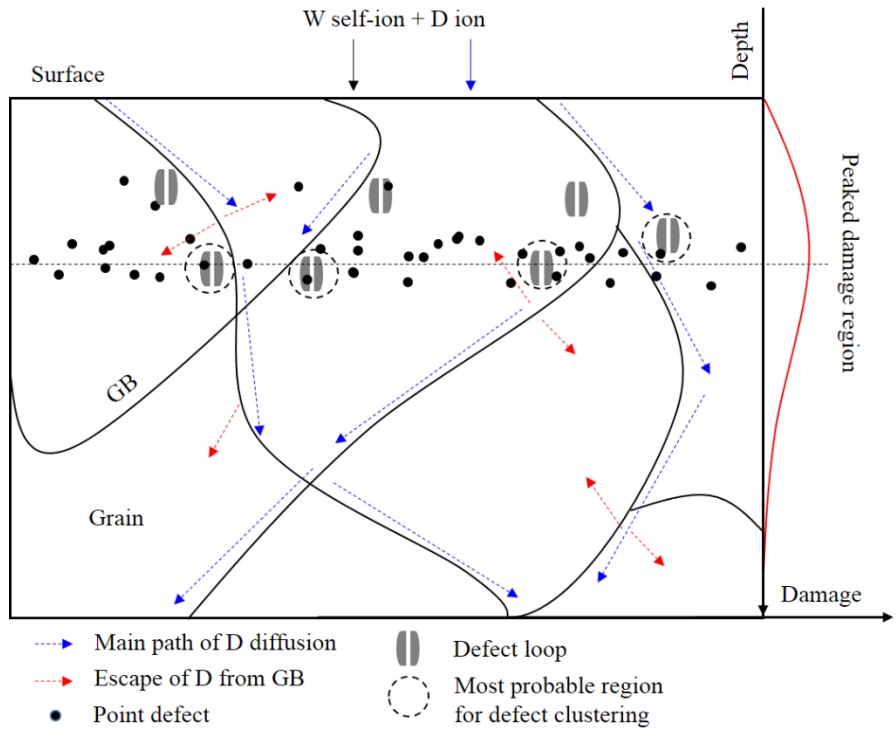

Figure 4-22. Description of the most probable region for defect clustering.

To investigate the effect of defect clustering on deuterium retention, both SIMS and TDS measurements were performed. SIMS informed the defect clustering effect on the spatial distribution of deuterium retention and TDS shows the defect clustering effect on both the retention amount and desorption energy. Because the hydrogen isotope retention is strongly dependent on the defects due to the deuterium trapping of defects which arranged in the Tanabe's review [3], the spatial distribution of D retention in damaged tungsten can be observed by SIMS. For the present work, the standard SIMS yield for deuterium to tungsten matrix is arranged for D fraction in W (C_D) as described in early .

Figure 4-23 (a)–(b) represent SIMS data of PCW irradiated only by deuterium and PCW (v) _W+D, respectively. It clearly shows the spatial distribution of deuterium retention

from the surface (0 nm) to 1,000 nm as the form of D fraction in PCW (v)_W+D. The fractions were quantified with the secondary ion yield as used in our previous work [13]. As shown in Figure 4-23 (a), in general, there are typically 3 peaks for deuterium retention in undamaged tungsten; (1) the surface adsorption at the surface (~0 nm), (2) oversaturation-induced vacancy-D trapping as observed in [13], and (3) the diffusion-induced hollow peak at the deep region (from μm to mm scale). If there are other peaks in the spatial distribution, it can be assumed that there is a strong trapping of D resulting from the newly induced defect or defect cluster. Remarkably, Figure 4-23 (b) of PCW (v) _W+D has an intense peak at the cascade damage peak region (~200 nm) with a suppressed diffusion–induced hollow peak (~μm). It implies that the self-ion induced defect formation clearly changed this spatial distribution of deuterium retention because of its high trapping energy [17]. The value of energy will be discussed in next section.

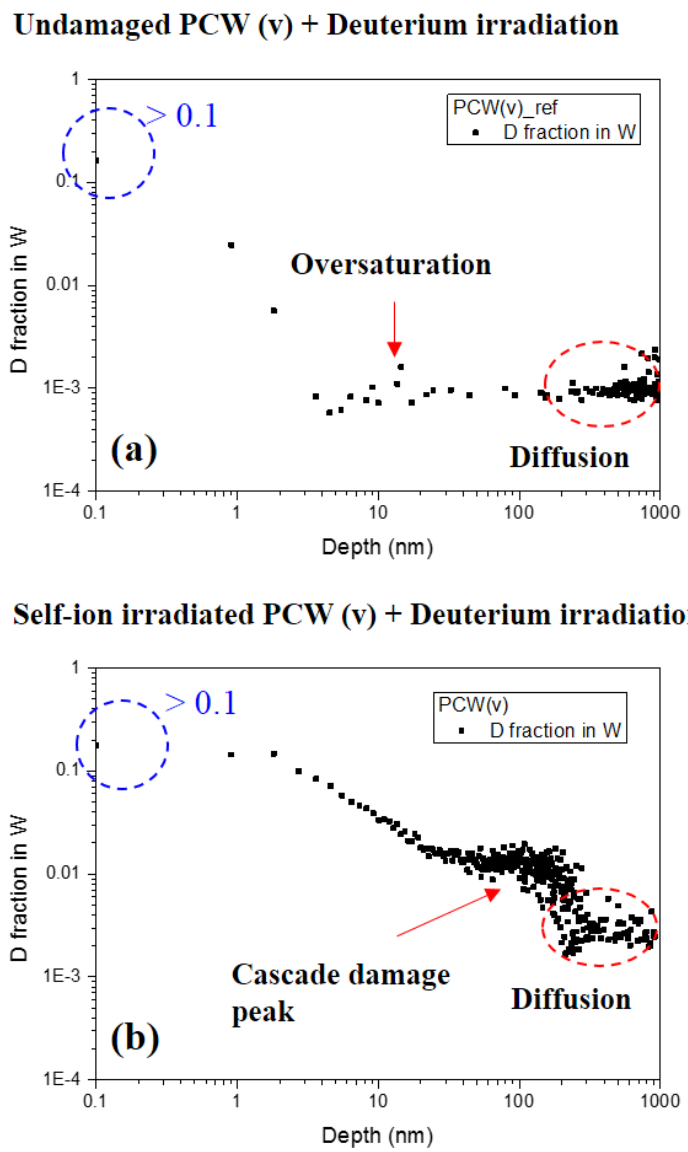

Figure 4-23. SIMS depth profiles of deuterium fraction in tungsten: (a) undamaged PCW (v), and (b) self-ion irradiated PCW (v). SIMS measured both cases after additional deuterium irradiation. Blue dashed line indicates the comparable surface adsorption, while red dashed line represents the diffusion-induced hollow contribution of deuterium.

Figure 4-24 (a)–(b) show the TDS spectrum and retention amount of the damaged and the undamaged PCW (v) with taking an approximated peak deconvolution based on Gaussian fitting function. Note that they give not an absolute value but an approximated value for being able to comparison. For desorption energy extraction with TDS deconvolution, the effect of spatially-distributed defect was not considered because the dimension of depth of trapping site (<1000 nm) is too shallow to induce the spatial effect such as delayed diffusion in this study. Thus, we can assume neglect the small peak shift or broadening in TDS spectrum. The typical desorption energy and corresponding peak temperature for using the peak energy analysis are arranged in Table 3-3. As a typical case, undamaged PCW (v) shows an intrinsic dislocation-induced trapping peak at 461 K (corresponding the desorption energy E_{des}~0.85 eV and corresponding peak temperature Tpeak~350–550 K) and the oversaturation-induced vacancy trapping peak at 638 K (corresponding E_{des}~1.84 eV, Tpeak~566–666 K). Note that the intrinsic dislocation-induced trapping peak comes from the remained fabrication-induced defect, which could occur even though the minimization through pre-annealing. However, it does not mean the ineffectiveness of pre-annealing because the peak area is clearly smaller than one of the plasma-caused oversaturation-induced vacancy trapping. For PCW (v)_W+D, it shows a clear highest temperature peak at 799 K as an additional peak with expected intrinsic two peaks at 496 K (dislocation-induced peak) and 664 K (vacancy-induced peak). The new peak implies new trapping source including in the damaged tungsten and it expect to correspond to the defect cluster because the results from TEM and SIMS indicate the existence of defect cluster in PCW (v)_W+D. By approximating the temperature with the Redhead approximation of equation (3.1), the highest peak at 799 K corresponds to the desorption energy of deuterium from trapping of defect cluster (E_{des} ~ 2.33 eV). It takes account for the highest temperature peak of the defect clustering in poly-crystalline tungsten. The increase of desorption energy was previously explained with the theoretical calculation. The binding energy is proportional to the number of

point defects as a form of cluster dues to the potential well change in the energy diagram [64]. Remind that the defect clustering initiated by the diffusion of hydrogen rather migration of defect as mentioned earlier, it can be expected that the defect clustering also can occur for the low deuterium irradiation temperature condition (< 573 K). Figure 4-25 shows the TDS spectrum of PCW (v) _W+D irradiated by deuterium at low tungsten target temperature (~400 K). It clearly shows the highest peak at 791 K that is an evidence of defect clustering. The results support that the 'plasma-induced defect clustering with trapped hydrogen at defect cluster'.

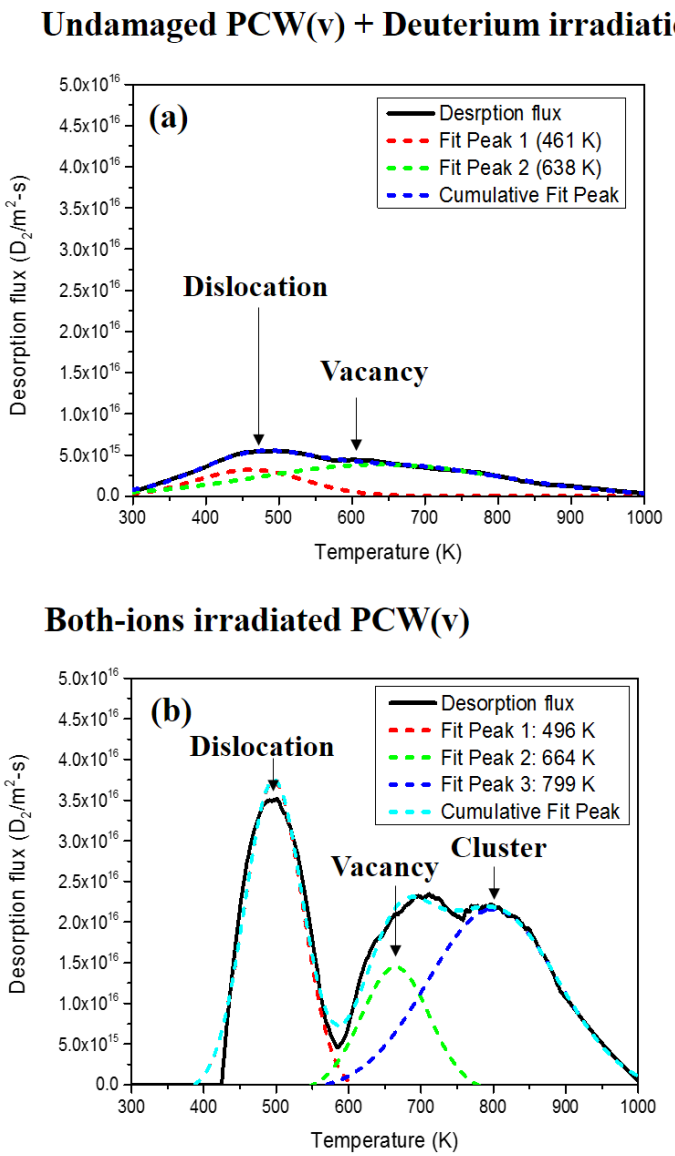

Figure 4-24. TDS results for (a) undamaged PCW (v), and (b) self-ion irradiated PCW (v). Both cases were measured by TDS after additional deuterium irradiation.

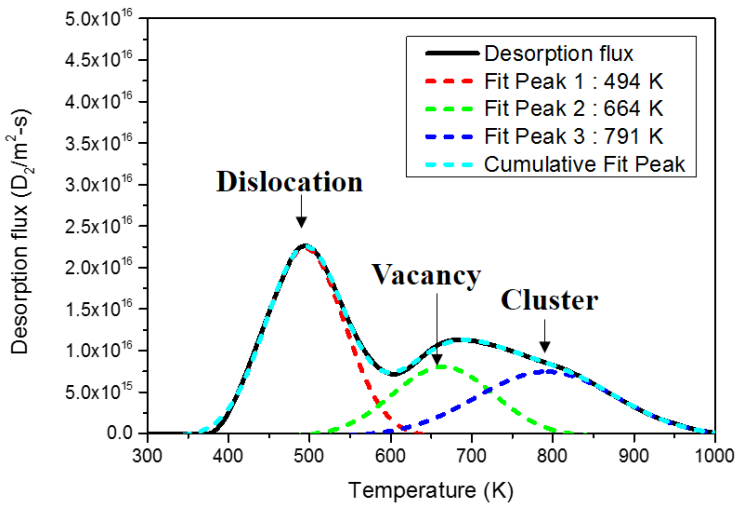

Figure 4-25. TDS results for self-ion irradiated PCW (v) at low deuterium-ion irradiation temperature (~ 400 K).

Results of fitted value in Figure 4-24 and Figure 4-25 represent the retention enhancement of damaged tungsten. The desorption temperature of the defect cluster is much higher than the dislocation induced peak. It deduces that the defect cluster-induced retention is harder to be recycled than dislocation-induced retention. To understand effect of defect cluster as high energy trapping source, the recycling flux is approximated with desorption rate equation. The definition of recycling flux is that the neutral D_2 flux from tungsten after de-trapping from trapping site and recombination on tungsten surface (2D ➔ D_2), which depends on desorption rate of deuterium from specific trapping site. If the recycling flux is lower than intrinsic tungsten due to higher activation energy for desorption, we can expect that the steady-state retention rate will be increased. According to the desorption energy calculated from our TDS results and the Redhead approximation (equation (3.1)), it can be written as equations (4.2) and (4.3) as following.

$$K_{dislocation}(T) = 8.4 \times 10^{12} \times \exp\left(-0.85eV / \mathrm{k}T\right) \quad (4.2)$$

$$K_{cluster}(T) = 8.4 \times 10^{12} \times \exp\left(-2.33eV / \mathrm{k}T\right) \quad (4.3)$$

According to the equations, desorption flux ratio of defect cluster and point defect (dislocation) varies from ~10^{-26} to 10^{-8} for the temperature range from 300 to 1,000 K. The ratio is far from 1 and it implies that the desorption rate of hydrogen from the defect cluster is negligible with respect to that of the point defect. The result of the defect clustering peak in TDS is consistent with the TEM results and SIMS results, which supports the existence of defect clusters in poly crystalline tungsten. Thus, our observation provides the evidence of a defect-deuterium agglomeration in damaged tungsten irradiated with deuterium, and also it can be regarded as a validation experiment of the defect clustering mechanism of Foreman *et al.* [58], [65].

Effect of grain boundary on the defect clustering was investigated with consideration of two proposition: (1) Negligible formation of vacancy loop in no-grain-boundary condition such as single-crystalline tungsten. (2) No defect clustering in the same condition regardless of deuterium irradiation. The irradiation condition for single-crystalline tungsten was chosen for that of poly-crystalline tungsten. In addition, dependence of elongation direction was also considered because it can change the deuterium diffusion in tungsten. Then the parallel-elongated poly-crystalline tungsten (PCW (p)) are adopted to investigate the agglomeration, comparing to the PCW (v) results.

First, the loop formation near grain boundary was investigated in PCW (p) and SCW after self-ion irradiation. Figure 4-26 (a) and (b) show high magnification of TEM images for the different crystalline tungsten samples, which carrying the same measurement details of PCW (v). The damage level and irradiation temperature are the same with PCW (v) as 0.7 dpa and

the process temperature kept at 300 K, respectively. Figure 4-26 (b) for PCW (p) _W shows the vacancy loop as the same for the case of PCW (v) _W. However, Figure 4-26 (d) for SCW_W shows no distinguishable evidence of vacancy loop, except only trace of FIB damage. This clear evidence of the grain boundary of poly-crystalline tungsten makes the defects to be concentrated and provides the location of deuterium-defect agglomeration to form loops.

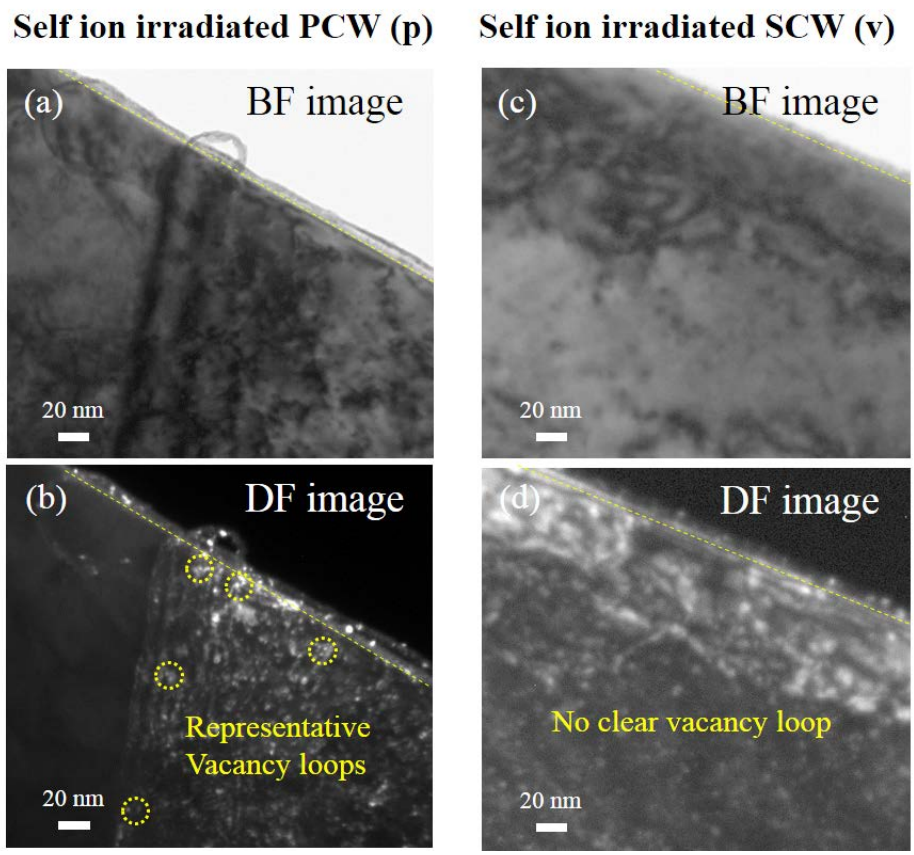

Figure 4-26. High magnification TEM imagery of cross-section for (a)–(b) PCW (v) undamaged, and (c)–(d) PCW (v) damaged up to 0.7 dpa by 2.8 MeV W^{2+} self-ion irradiation. (a) and (c) are bright-field (BF) images, while (b) and (d) are dark-field images. Yellow dashed-line indicates the surface of tungsten samples.

The defect clustering was investigated after additional deuterium ion irradiation on the damaged PCW (p) and SCW (PCW (p)_W+D, SCW_W+D). Figure 4-27 shows deuterium depth profile obtained from SIMS measurement with same experimental details of PCW (v) _W+D. Because the loop has a stronger attracting force than a point defect [64] as mentioned earlier, the loop could be the pre-cursor of a defect cluster. Figure 4-27 (a) shows that retained-D depth profile of PCW (p)_W+D which is analogous to that of PCW (v)_W+D including highly peaked distribution near cascade damage peak (100-200 nm). Hence, there is no difference between PCW (v)_W+D and PCW (p)_W+D. Those two are structurally corresponding to each other in spatial distribution. It implies no significant effect of grain elongation direction on the subsurface retention. In contrast to poly-crystalline tungsten (PCW (v) and PVW (p)), SCW_W+D case in Figure 4-27 (b) shows a relatively less peaked region at the cascade damage peak (100-200 nm) with an enhanced diffusion-induced hollow peak at the deep region (~μm). The peak in deep region (500-1000 nm) can be interpreted that the enhanced diffusion due to low activation energy for diffusion in grain-boundary-less tungsten as discussed in previous part. Thus, it takes account for no severe formation of defect cluster, which can form peaked region due to high energy trapping (E_{des}=2.33 eV).

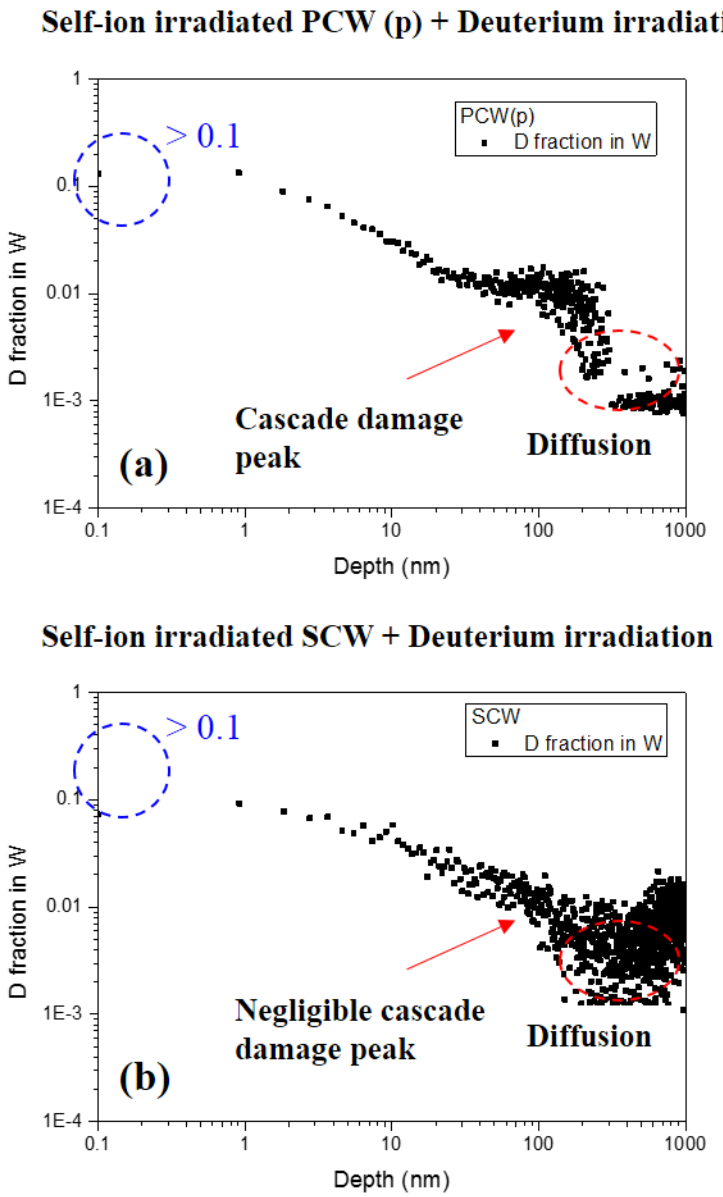

Figure 4-27. SIMS depth profiles of deuterium fraction in tungsten: (a) PCW (p)_W+D, and (b) SCW_W+D after sequential irradiation of 100 eV D_2^+ ion irradiation. Blue dashed line indicates the comparable surface adsorption, while red dashed line represents the diffusion-induced hollow contribution of deuterium.

Because only SCW case shows difference with PCW (v) in SIMS data, TDS spectrums were obtained for undamaged and damaged SCW to investigate the effect of grain boundary, excepting PCW (p) case. We can expect that the same TDS spectra of PCW (p) with PCW (v) due to same SIMS data. Figure 4-28 (a) and (b) show the TDS spectrum for undamaged and damaged SCW_W+D. Figure 4-29 shows the contribution of each defect type to the retention amount of undamaged SCW, undamaged PCW(v), damaged SCW, and damaged PCW(v), respectively. For quantitative discussion in terms of retention enhancement for different crystalline tungsten, TDS peaks deconvolution was performed to approximate the quantitative contribution of each defect type for dislocation, vacancy, and defect cluster (vacancy cluster). The approximated retention amount for each defect type can be calculated from the area of the TDS spectrum, since the x-axis is time, which was converted into temperature for the linear heating scheme of TDS. According to Figure 4-28 (a), undamaged SCW_W+D shows similar spectrum with undamaged PCW (v). The only thing to note is that the undamaged SCW shows less retention amount than undamaged PCW (v). This is understandable because the SCW has less trapping site such as fabrication-induced dislocation and grain boundary. TDS spectrum for damaged SCW in Figure 4-28 (b) shot that a negligible peak of cluster-induced at highest temperature (700-800 K) region unlikely to damaged PCW (v). The difference between undamaged SCW and damaged SCW seems only the number of point defect but not defect cluster. Thus, the defect clustering in SCW is negligible.

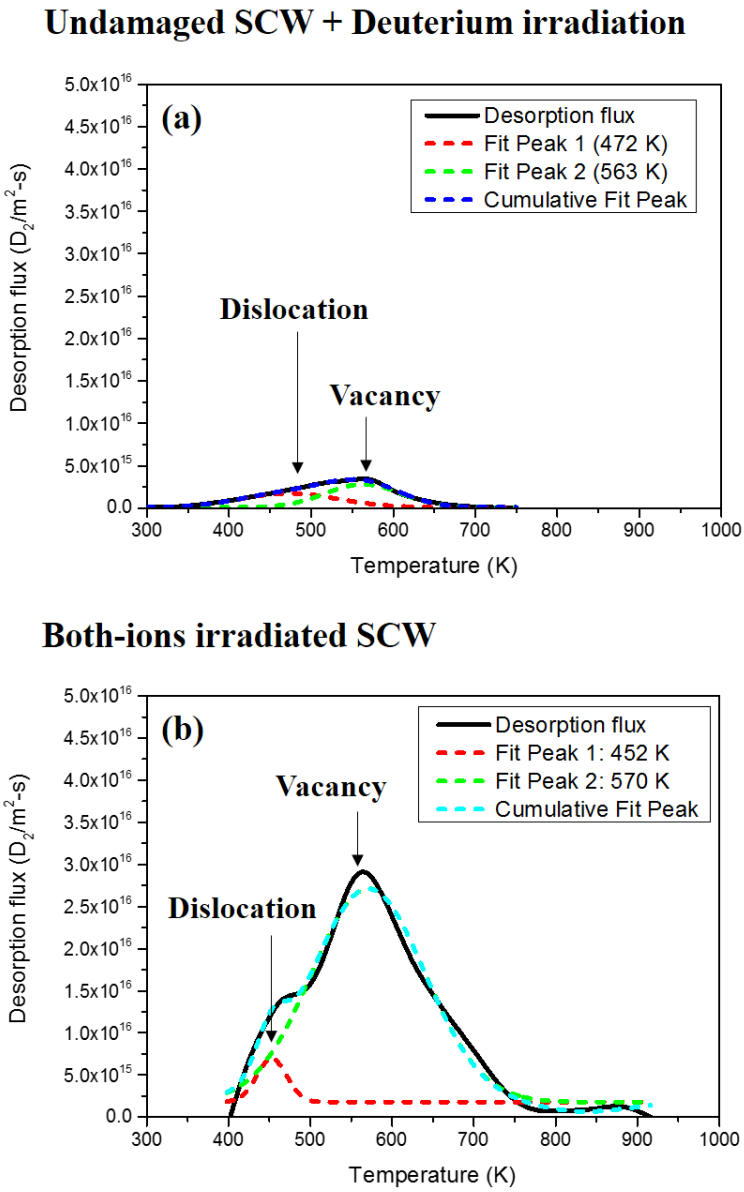

Figure 4-28. TDS spectrum for (a) undamaged SCW and (b) damaged SCW after sequential irradiation of 100 eV D_2^+ ion irradiation.

Figure 4-29 clearly shows that most of the increased retention amount for damaged PCW is caused by the contribution of deuterium trapping of the defect cluster, rather than increased point defects (dislocation, vacancy). These results are consistent with previous TEM observation and SIMS results that there is no defect clustering in SCW. The quantitative retention enhancement of the damaged PCW is about 500% with respect to the undamaged PCW. The conclusion to be drawn here is that previous results for PCW showing higher retention than SCW clearly arise from the defect clustering by defect-deuterium agglomeration in PCW, which does not dominantly occur in SCW.

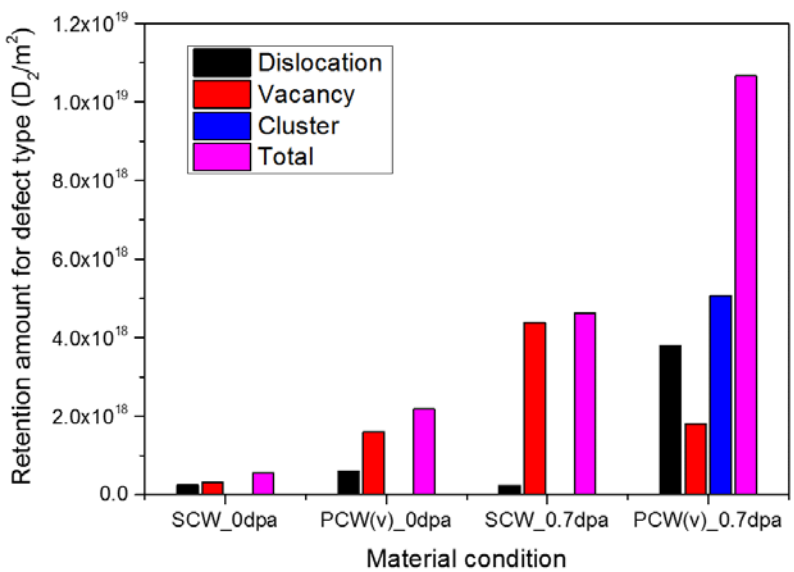

Figure 4-29. The total retention amount for undamaged SCW, undamaged PCW (v), PCW (v)_W+D, and SCW_W+D. Each bar means the quantitative contribution of defect types approximated by peak area after TDS peak deconvolution.

In conclusion of section 4.4, the retention enhancement for the poly-crystalline tungsten in the presence of both cascade damage (by self-ion irradiation) and hydrogen isotope plasma exposure is investigated experimentally. The defect cluster trapping of deuterium ($E_{des,3}$=2.39 eV) occurred through the defect clustering by the defect-deuterium agglomeration when the sufficient deuterium concentrates on the immobile defect loop. The phenomenon provides a high probability to occur at superposition region between deuterium and defect, so the defect clustering observed near the grain boundary region of damaged poly crystalline tungsten. By including the dominant retention reactions of defect cluster trapping ($E_{des,3}$=2.39 eV), for plasma with high energy ion, the volume retention reactions consist of hydrogen solution ($E_{des,0}$=0.75-0.95 eV), oversaturation-induced vacancy trapping ($E_{des,1}$=1.84 eV), defect cluster tapping ($E_{des,3}$=2.39 eV).

4.5 Variation of retention by fusion-relevant effect

4.5.1 **Introduction**

Up to previous section, the retention was investigated concentrated on long-term volume retention reactions, which will occur intrinsically under hydrogen plasma operating condition without consideration of fusion-relevant additional operation strategy such as gas puffing and high heat flux. Those two conditions are infrequently occurred for process plasma, but they can be frequently occurred for fusion plasma circumstance. To consider application of developed hydrogen retention model for fusion plasma, this study includes fusion-relevant effects. Thus, if we consider fusion-relevant study for hydrogen retention model, the effect of Ar puffing gas and He ash should be investigated whether it change desorption energy or retention amount. To investigate the effect of Ar puffing gas and He ash indirectly in lab-scale plasma system, admixing condition was applied to deuterium plasma with varying partial pressure for consistent pressure of deuterium. In addition, we also study for the effect of tungsten recrystallization as a material condition change by heat flux in fusion reactor. This effect should be considered for fusion application because the plasma-facing material exposed to heat flux as well as particle flux. To investigate the effect of heat flux, recrystallization depth was considered as variable which can be changed by exposure time of heat flux. In summary, the experiment conditions consist of gas-admixed deuterium plasma exposure onto tungsten, deuterium plasma exposure onto recrystallized tungsten.

4.5.2 **Experimental setup**

In terms of variation effect in fusion-relevant condition, both He ash and Ar puffing gas effects were indirectly understood by using admixing condition for deuterium plasma. The experiment for admixing gas effect is carried out with the same plasma irradiation facility, SNU-ECR plasma system. Nevertheless, it is not the same condition for fusion-relevant condition, it is effective to distinguish controlled effect of specific gas as a variation from the reference condition. By using the strategy, we can clearly investigate the change of desorption energy and the change of retention amount. Admixing conditions consist of partial pressure ($P_{He\,or\,Ar}$) range from 0% to 20% for the consistent deuterium plasma condition. Because the admixing gas change the plasma property, the deuterium ion fluence was changed. It is not the problem to investigate the change of desorption energy because it does not depend on fluence effect. While, it can be not negligible to compare quantitatively. Thus, we can discuss mainly for desorption energy, and discuss quantitatively variation of retention amount with respect to variation of the ion fluence. If the variation of retention amount is larger than variation of ion fluence, the variation effect of admixing gas clearly makes the difference.

4.5.3 **Variation of volume retention reactions by He ash gas and Ar puffing gas effects**

To quantitatively estimate the variation, the variation of plasma property by admixing gas into deuterium plasma was firstly analyzed. The selected admixing gases (He, Ar) stand for He ash and argon puffing gas in fusion plasma reactor. For partial pressure ($P_{He\ or\ Ar}$) range of admixed gas from 0% to 20%, the variation was arranged with plasma density (n_e) and electron temperature (T_e). The degree of variation was observed as low as under 20% for plasma density and 10% for electron temperature. The detail of the plasma properties is arranged in Figure 4-30. Based on the results, if the variation of retention amount for admixing gas is over the variation of plasma density, we can conclude that the variation of retention is not resulted from variation of ion fluence but the variation effect of admixing gas.

To expect effect of admixing gas irradiation on tungsten, SRIM calculation was carried out to estimate sputtering yield and defect generation rate by He and Ar. The ion range implies the depth that can be affected by incident admixing gas. The sputtering yield implies the possibility of erosion. In addition, defect generation rate is the possibility of additional E_{des} by physical defect. Figure 4-31 show the results that the He is ineffective to make defect or to sputter tungsten while Ar induce significant sputtering and defect generation rate. According to that, we can expect that the He effect on tungsten will be limited in surface while Ar effect can occur within subsurface. However, Ar effect cannot be observed when the sputtering overwhelms the defect generation.

For the same condition of admixing gas, plasma exposed tungsten samples were measured by TDS to investigate the amount of retention and corresponding retention volume reactions with the same condition of TDS.

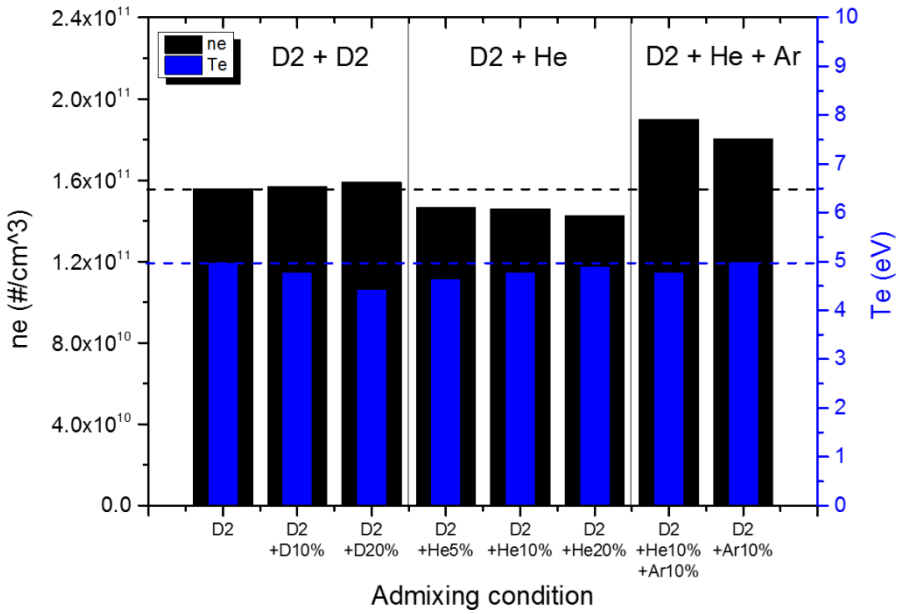

Figure 4-30. Plasma properties for different admixing gas condition. Left axis stands for the plasma density while right axis stands for the electron temperature. The admixing conditions including D plasma, D plasma with additional D pressure, D plasma with 5% of He pressure, D plasma with 10% He pressure, D plasma with 20% of He pressure, D plasma with 10% of Ar pressure, D plasma with both 10% of Ar and 10% of He pressure.

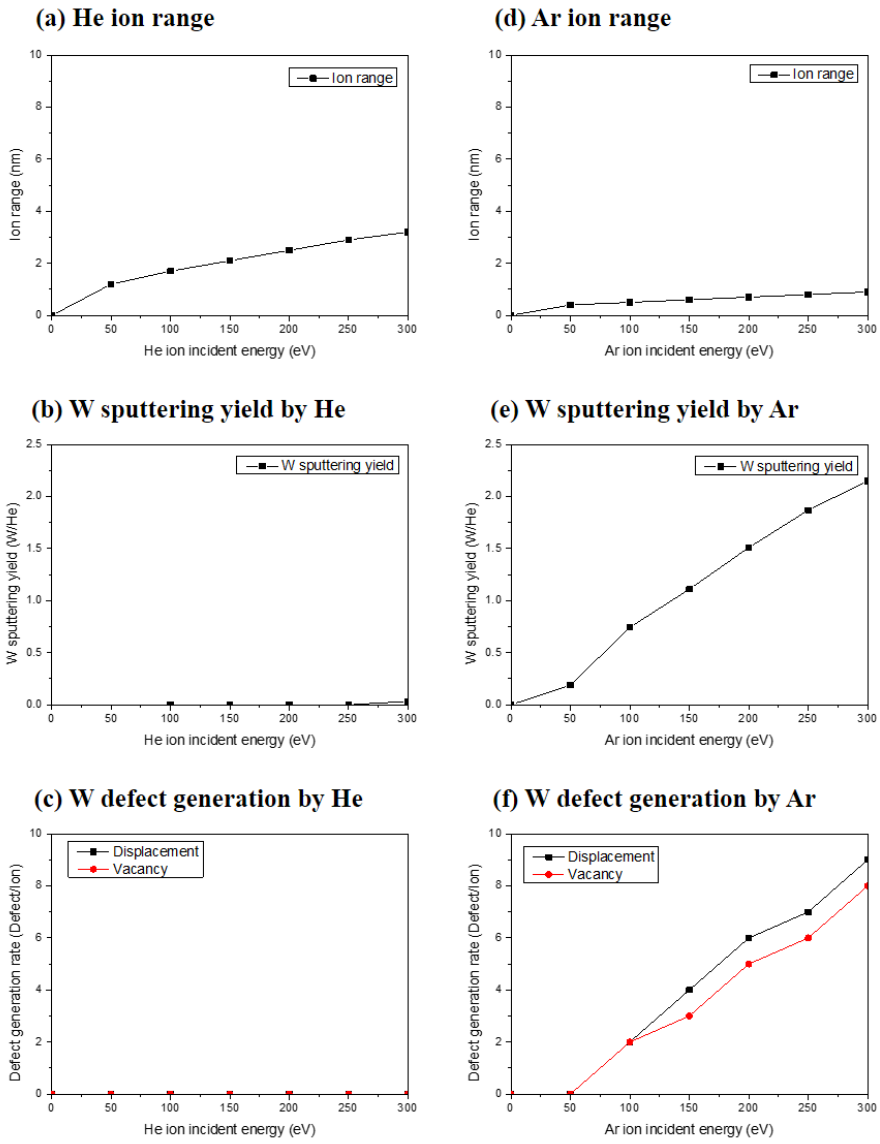

Figure 4-31. SRIM calculation results for tungsten under irradiation of He and Ar. The range of incident ion energy is from 0 to 300 eV, which cover expected ion incident energy in fusion reactor excepting transient event. (a) He ion range, (b) W sputtering yield by He, (c) W defect generation by He, (d) Ar ion range, (e) W sputtering yield by Ar, (f) W defect generation by Ar.

The first effect is helium-induced nano-structure on tungsten surface under helium-admixing deuterium plasma irradiation. According to Figure 4-32, the results show that relatively decreased total retention amount and effectively reduced oversaturation-induced vacancy trapping. The reduction of oversaturation-induced vacancy trapping is more obvious than fabrication-induced dislocation trapping. According to Figure 4-33, the results are observed clearly by contribution of each volume retention reaction. This effect can be explained by surface change of tungsten under helium-admixing deuterium plasma irradiation. Figure 4-34 shows that the FESEM image of tungsten surface after irradiation. It shows that the helium-induced nanostructure onto tungsten surface, which is previously reported that it can reduce deuterium diffusion into tungsten during plasma irradiation. Thus, the phenomenon can be defined as ‘diffusion barrier effect’. With the point of view, we can understand that the reduction of oversaturation-induced vacancy trapping is resulted from the reduction of deuterium diffusion into tungsten due to ‘diffusion barrier effect.

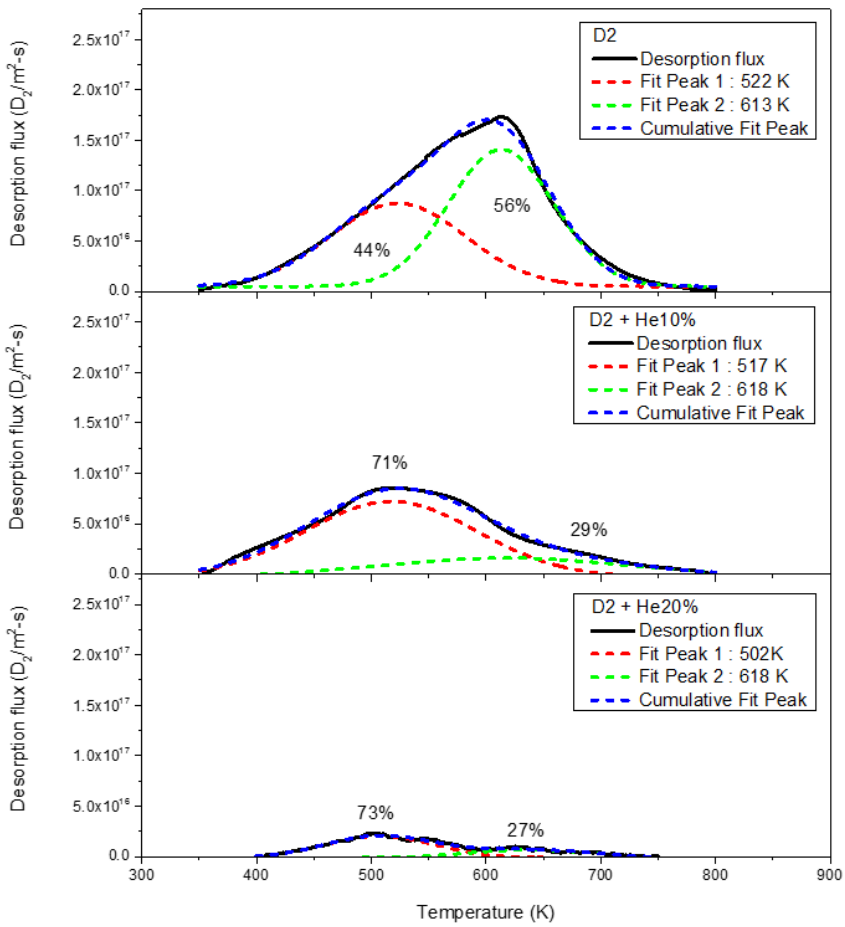

Figure 4-32. TDS spectrums for tungsten irradiated by deuterium plasma with helium-admixing condition. The fractions of helium pressure are 0%, 10%, 20% with respect to deuterium pressure (2.25 mTorr). X-axis denotes desorption temperature while Y-axis stands for desorption flux as functions of desorption temperature. Peak deconvolution for all TDS spectra were performed with Gaussian fit with fabrication-induced dislocation trapping peak (350-550 K) and oversaturation-induced vacancy trapping peak (566-666 K).

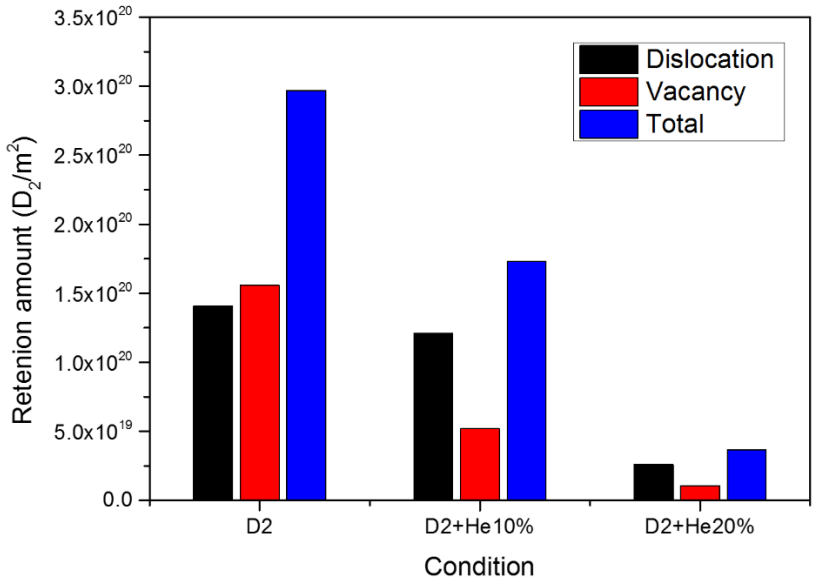

Figure 4-33. Retention amount for each admixing condition with detailed contribution of specific type of trapping site. The conditions are consisting of D plasma, D plasma with 10% of He, D plasma with 20% of He. The type of trapping site consists of fabrication-induced dislocation and oversaturation induced vacancy. Total deuterium retention amount also estimated with dependence on admixing condition.

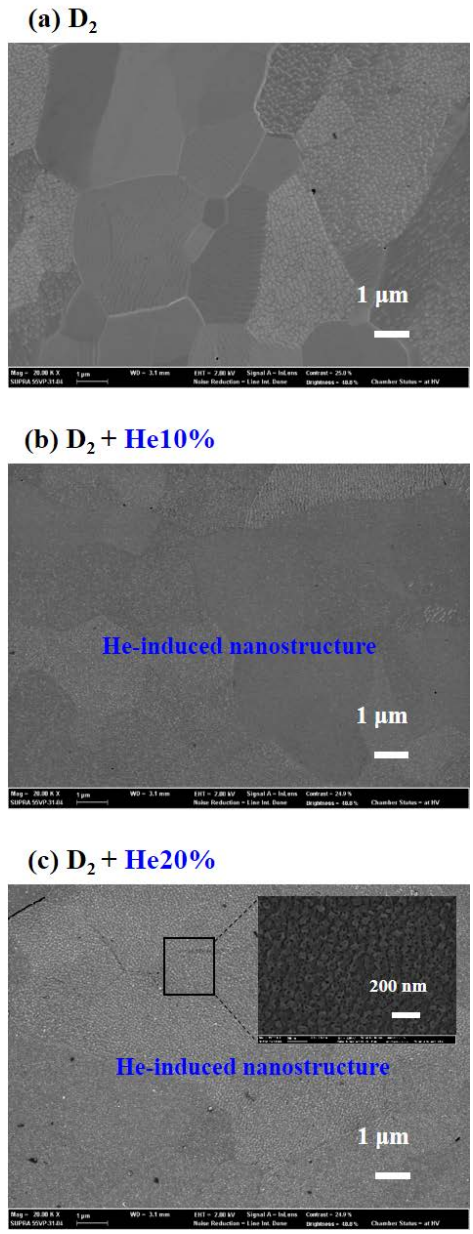

Figure 4-34. FESEM images of tungsten surface irradiated by helium-admixing deuterium plasma with different composition: (a) D_2, (b) D_2 + He 10%, (c) D_2 + He 20%.

The other effect is argon-induced surface sputtering on tungsten surface under argon-admixing deuterium plasma irradiation. According to Figure 4-35, the results also show that relatively decreased total retention amount and effectively reduced fabrication-induced dislocation trapping. The reduction of fabrication-induced dislocation trapping is more obvious than oversaturation-induced vacancy trapping. According to Figure 4-36, the results are observed clearly by contribution of each volume retention reaction. This effect can also be explained by surface change of tungsten under argon-admixing deuterium plasma irradiation. Figure 4-37 shows that the FESEM image of tungsten surface after irradiation. It shows that the argon-induced sputtered tungsten surface because the grain boundary is observed with more clear contrast, which can be the cause of the reduction of fabrication-induced dislocation within tungsten near-surface region. Thus, the phenomenon can be defined as ‘surface sputtering effect’. With the point of view, we can understand that the reduction of fabrication-induced dislocation trapping is resulted from the reduction of near-surface dislocation due to ‘surface sputtering effect of argon (Mass=40 amu), which has higher momentum to sputter tungsten atoms than deuterium atom (Mass=2 or 4 amu).

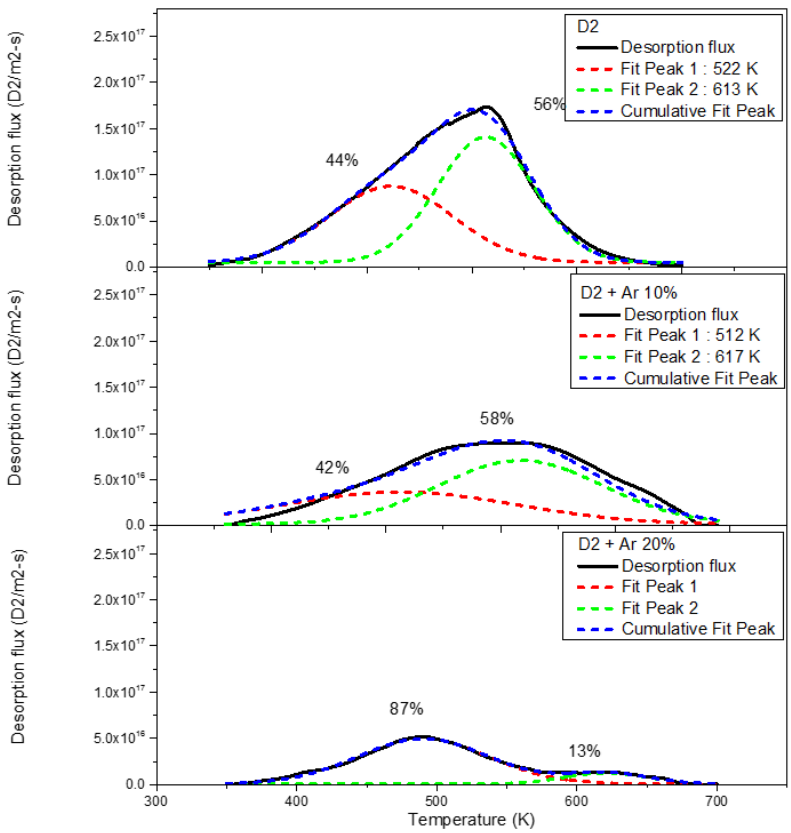

Figure 4-35. TDS spectrums for tungsten irradiated by deuterium plasma with argon-admixing condition. The fractions of admixing argon pressure are 0%, 10%, 20% with respect to deuterium pressure (2.25 mTorr). X-axis denotes desorption temperature while Y-axis stands for desorption flux as functions of desorption temperature. Peak deconvolution for all TDS spectra were performed with Gaussian fit with fabrication-induced dislocation trapping peak (350-550 K) and oversaturation-induced vacancy trapping peak (566-666 K).

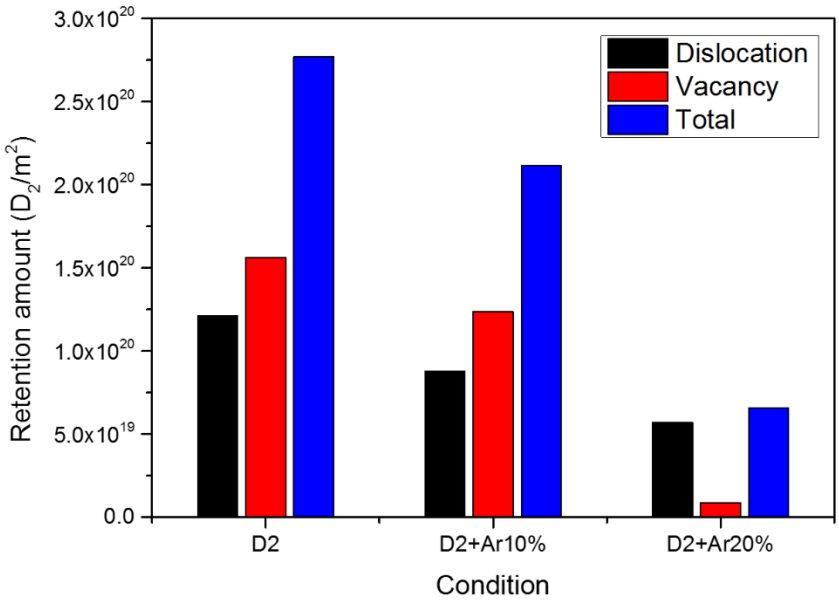

Figure 4-36. Retention amount for each admixing condition with detailed contribution of specific type of trapping site. Admixing conditions are consisting of D plasma, D plasma with 10% of Ar, D plasma with 20% of Ar. The type of trapping site consists of fabrication-induced dislocation and oversaturation induced vacancy. Total deuterium retention amount also estimated with dependence on admixing condition.

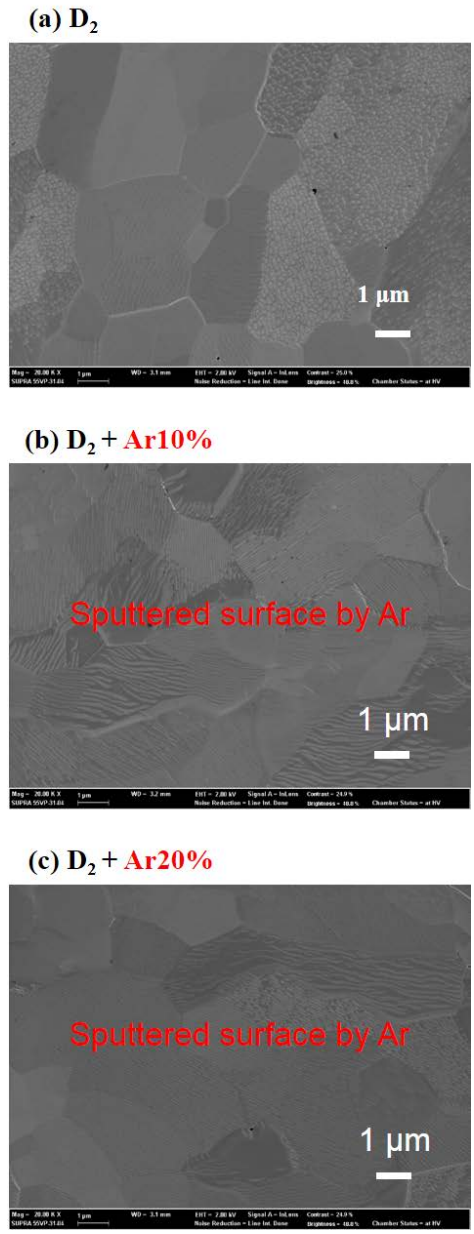

Figure 4-37. FESEM images of tungsten surface irradiated by argon-admixing deuterium plasma with different composition: (a) D_2, (b) D_2 + Ar 10%, (c) D_2 + Ar 20%.

In conclusion of section 4.5, as a variation effect of between fusion-relevant gas, the effect of helium and argon on tungsten under both helium and argon admixing deuterium plasma irradiation. The results are arranged with individual effect and variation effect. As we can expect, the results also show that relatively decreased total retention amount as shown in Figure 4-38. The reduction is clearly due to the reduction of both oversaturation-induced vacancy trapping and fabrication-induced dislocation trapping. In other words, the retention amount is clearly reduced by helium-induced diffusion barrier effect and argon-induced surface sputtering effect. The variation effect is confirmed with SIMS data in Figure 4-39, which show the subsurface deuterium concentration with the spatial distribution. Figure 4-39 shows that the clearly reduced deuterium concentration in bulk region with concentrated deuterium in subsurface, which is corresponding to the thickness of helium-induced nano-structure. The results confirm the diffusion barrier effect. For the admixing gas case with the both of helium and argon, the diffusion barrier effect shows negligible effect due to sputtering of helium-induced nanostructure onto tungsten surface. Therefore, in fusion-relevant circumstance, the two effects will occur competitively depending on admixing condition of edge plasma region.

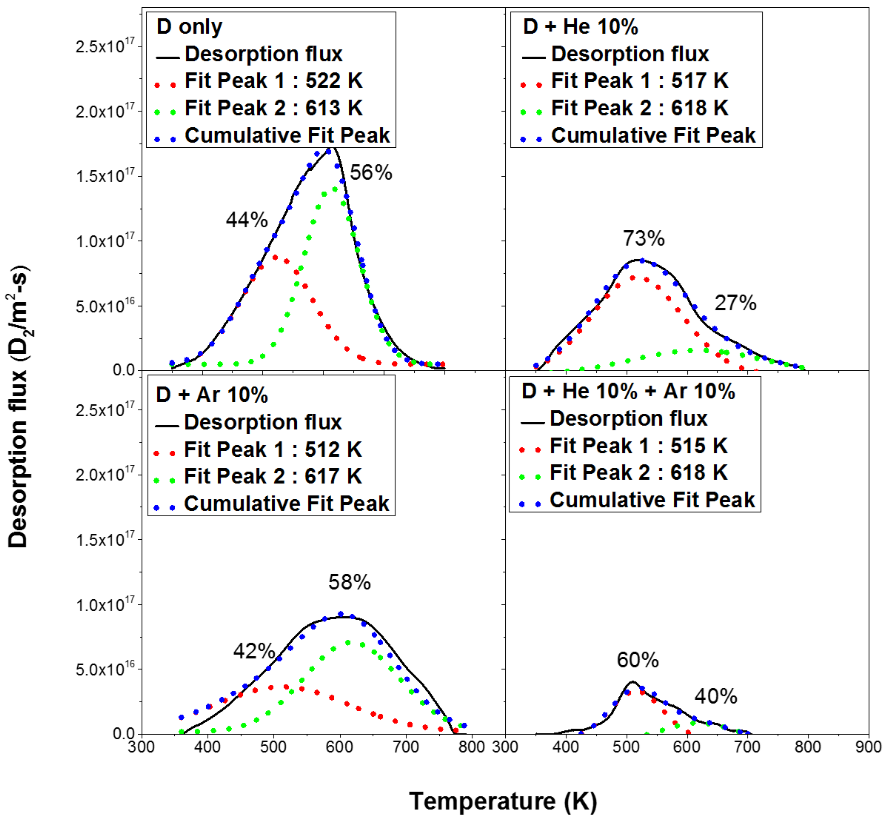

Figure 4-38. TDS spectrums for tungsten irradiated by deuterium plasma with both helium and argon-admixing condition. The fractions of admixing argon pressure are 10% and 20% with respect to deuterium pressure (2.25 mTorr). X-axis denotes desorption temperature while Y-axis stands for desorption flux as functions of desorption temperature. Peak deconvolution for all TDS spectra were performed with Gaussian fit with fabrication-induced dislocation trapping peak (350-550 K) and oversaturation-induced vacancy trapping peak (566-666 K).

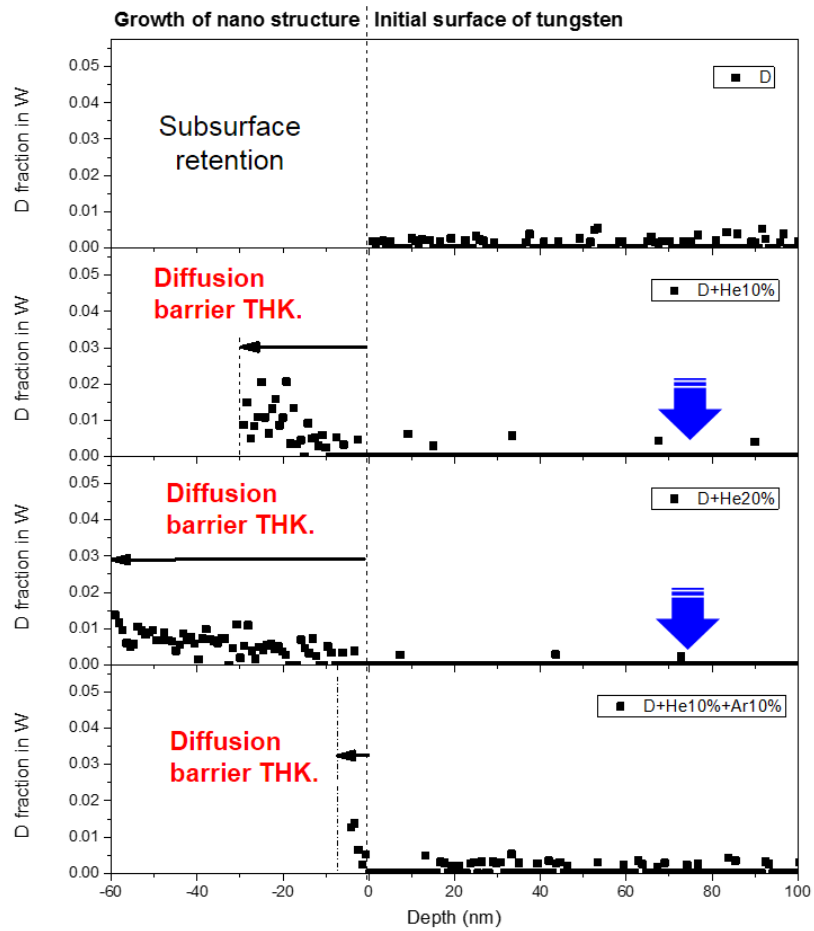

Figure 4-39. Spatial distribution of deuterium in tungsten measured by SIMS. Plasma exposure conditions are consisting of D plasma, D plasma with 10% of He, D plasma with 20% of He, D plasma with 10% of He and 10% of Ar. Measured depth from tungsten surface is about 100 nm. D fraction in W was calibrated with SIMS yield for deuterium and tungsten.

4.5.1 Variation of volume retention by heat flux-induced tungsten recrystallization effects

The experiment to investigating variation effect of heat flux-induced recrystallization was carried out with firstly inducing heat flux onto tungsten surface. To expect effect of heat flux quantitatively, the variation was arranged with recrystallization depth as most severe effect of heat flux. By varying the time of heat flux exposure on to tungsten, recrystallization depth was changed from 0 mm, 0.1 mm, 1 mm. The value of 1 mm indicates full recrystallization of tungsten sample since the thickness of tungsten samples is 1 mm. The definition of recrystallization depth is depth from surface to where grain growth occurs. Nevertheless the grain growth is not exactly same with recrystallization, most of case accompanying grain growth in recrystallized layer [66]. The experimental condition and setup are arranged in Table 4-8. Figure 4-41 shows the thickness variation of recrystallized tungsten subsurface. The depth of recrystallization was defined with depth from surface to maximum thickness where the grain was growth as an indirect evidence of recrystallization. The upper images show high magnitude images to show grain growth while the lower images show lower magnitude to show full dimension of tungsten samples.

Figure 4-42 shows the TDS spectra of recrystallized tungsten after deuterium irradiation. The spectra show two peaks defined in previous parts. The first peak is fabrication-induced dislocation trapping of deuterium while the second peak is deuterium oversaturation-induced vacancy trapping of deuterium. The first peak shows variation depending on recrystallization depth that the higher depth the low peak magnitude, implying that the recrystallization reduced the retention amount resulted from the retention mechanism of first peak. This variation is well shown in Figure 4-42, which shows contribution for retention of each types of retention mechanism denoting with desorption energy. The reduction of fabrication-induced dislocation

trapping is clearly shown by reduction of retention amount for $E_{des,0}$. Because the mechanism is fabrication-induced dislocation trapping of deuterium, it is reasonable that the recrystallization reduces fabrication-induced defect in tungsten subsurface.

Table 4-8 Experimental conditions for differently induced recrystallization depth of tungsten under thermal plasma exposure.

Recrystallization depth	**0.1 mm**	**1 mm**
Surface temperature of tungsten	1480 °C	1680 °C
Steady-state heat flux	1 MW/m^2	5 MW/m^2
Exposure time	20 secs	20 secs

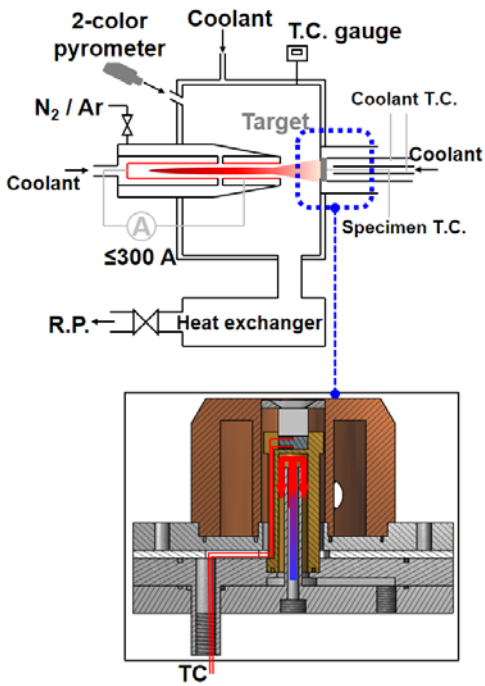

Figure 4-40 Experimental setup for heat flux exposure to inducing different recrystallization depth of tungsten from surface to bulk region.

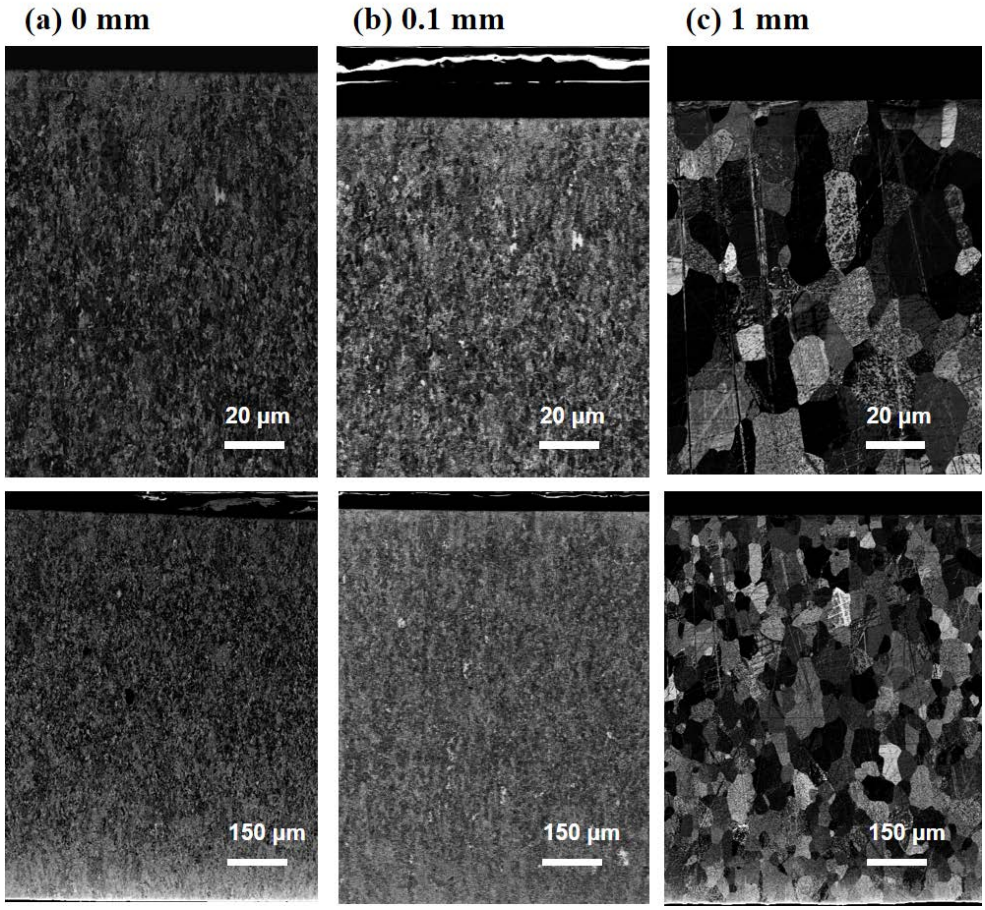

Figure 4-41. FESEM images of recrystallized tungsten subsurface. (a) recrystallization depth is 0 mm, (b) recrystallization depth is under 0.1 mm, (c) recrystallization depth is 1 mm. The depth of recrystallization was estimated by the depth that the grain growth occurs from surface to bulk of tungsten.

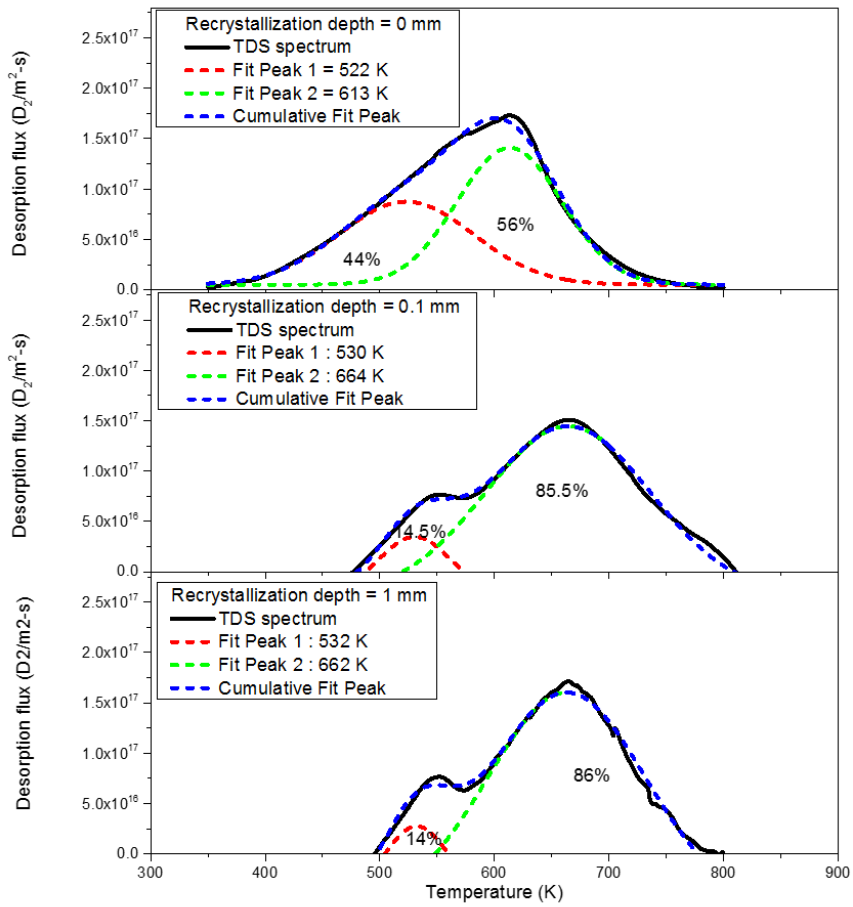

Figure 4-42 TDS spectrums for tungsten irradiated by deuterium plasma with heat flux-induced recrystallization of tungsten. The depths of recrystallization are 0 mm, 0.1 mm, 0.2 mm. X-axis denotes desorption temperature while Y-axis stands for desorption flux as functions of desorption temperature. Peak deconvolution for all TDS spectra were performed with Gaussian fit with fabrication-induced dislocation trapping peak (350-550 K) and oversaturation-induced vacancy trapping peak (566-666 K).

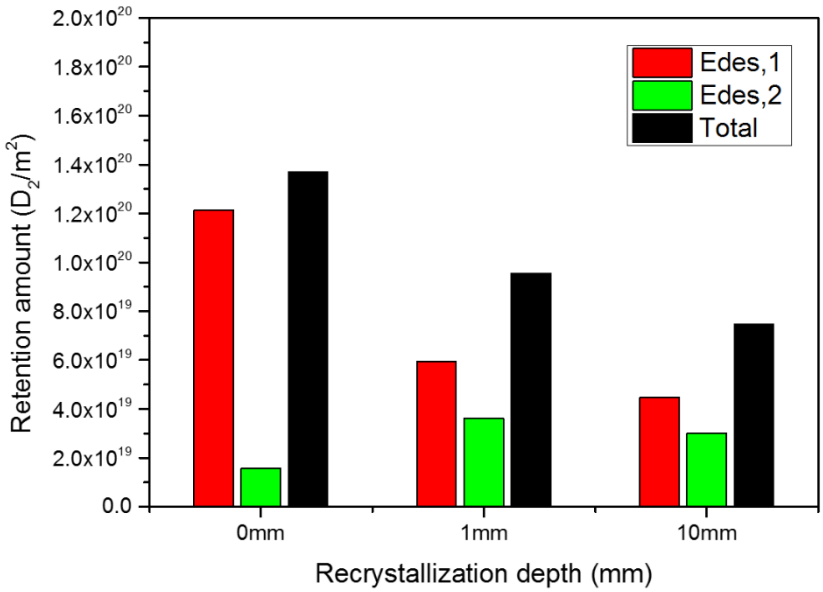

Figure 4-43. Retention amount for heat flux-induced recrystallized tungsten with detailed contribution of specific type of trapping site. The depths of recrystallization are 0 mm, 0.1 mm, 0.2 mm. Total deuterium retention amount also estimated with dependence on admixing condition.

4.6 Construction of hydrogen retention model including long-term volume retention

As a part of hydrogen retention model, the long-term volume retention reaction and variation effect were arranged, which has significance of importance reference data for hydrogen retention model because it dominates the wall recovery time depending on both retention amount and desorption energy. Because the variation effect does not change the desorption energy but change the amount only, the main reaction is long-term volume retention reaction with corresponding desorption energies. The main volume retention reactions consist hydrogen solution ($E_{des,0}$: 0.75-0.95 eV), hydrogen oversaturation ($E_{des,1}$: 1.84 eV), carbon impurity-induced chemical trapping ($E_{des,2}$: 2.33 eV), physical damage-induced defect cluster trapping ($E_{des,3}$: 2.39 eV). In terms of variation effect in fusion-relevant condition, both He ash and Ar puffing gas effects were indirectly understood by using admixing condition; by surface modification and sputtering, both gases reduce retention amount (ΔN_{wall}=50-90 %), which is over the density variation of admixed plasma (Δn_e=10-20%). However, both gases did not change the desorption energy ($\Delta E_{des,i}$=0). For the same point of view, the effect of tungsten recrystallization was also analysed that can reduce hydrogen retention amount (ΔN_{wall}=30-50%) due to reduced fabrication-defects but not change the desorption energy ($\Delta E_{des,i}$=0). The dimensions of volume retentions were extended from subsurface (nm ~ μm) to bulk (μm ~ mm) depending incident energy of implanted plasma ions (100 eV/D_2^+), impurity ions (300-400 eV/C^{4+}), and high energy ions (2.8 MeV/W^{2+}). The dimension of corresponding reactions will be effective variables for understanding the interaction between plasma and plasma-facing material during the operation because the plasma facing material experience the change of material and retention reactions from subsurface to bulk as a function of depth. Thus, the information can also be used to design plasma-facing component considering effective plasma

surface interaction such as radioactive tritium retention. In summary, both volume retention reactions and variation effects are arranged in Table 4-9. Along the hydrogen particle balance with plasma facing material including retention, recycling, permeation, the permeation of hydrogen crossing the tungsten material is not included in hydrogen retention model because 1) permeation is too small to change retention amount due to low hydrogen solubility in tungsten [3], 2) permeated hydrogen is not ejected to plasma in plasma system because permeated gas diffuse into structure material which bonded with plasma-facing material.

Table 4-9. Summary of long-term volume hydrogen retention and variation effects.

PWI condition	**Long-term volume hydrogen retention**		**Variation effects**		**Desorption energy (E_{des})**	**Dimension**
	Phenomenon	Effects	Phenomenon	Effects		
D plasma exposure onto W	Solution, Fabrication defects	*W-D* bond, Dislocation trapping			0.75-0.95 eV	Entire volume
D plasma exposure onto W	Oversaturation	Vacancy trapping			1.84 eV	Subsurface ~ few nm
D plasma exposure onto C-implanted W	Impurity implantation	Chemical impurity trapping			2.33 eV	Subsurface ~ nm-μm
D plasma exposure onto defect-formed W	Cascade collisional damage	Defect cluster trapping			2.39 eV	Volume ~ μm-mm
He gas-admixed D plasma exposure onto W			Variation: Diffusion barrier effect		Mainly 1.84 eV	Subsurface ~ few nm
Ar gas-admixed D plasma exposure onto W			Variation: Surface sputtering		All	Surface~ nm-μm
D plasma exposure onto recrystallized W			Variation: Recrystallization		Mainly 0.75-0.95 eV	Volume ~ μm-mm

Chapter 5 . Validation of Retention Model with Recycling-induced Plasma Variation

The temporal and spatial variation of hydrogen plasma by influx from tungsten wall to plasma were analyzed and expected with the hydrogen retention model and desorption energy data set of volume retention reactions. The influx is the function of desorption energy because the desorption energy is the activation energy for hydrogen desorption from trapped site. By adapting desorption energy and desorption rate equation into particle balance equation and by comparing it with experimental results as a point of wall recovery time, the hydrogen retention model can be verified, and the value of desorption energy will be confirmed as a reference data.

5.1 Wall recovery time: parameter to validate hydrogen retention model for expecting plasma variation

To validate the hydrogen retention model, formulation of influx equation was carried out by using desorption energy which was obtained from the study of volume retention reaction in previous section. To compare model with experiments, comparable variable is needed. Because recycling amount is hard to measure during plasma operation due to complex effect on plasma property not just proportional relationship, wall recycling time was selected as comparable variable, which can be observed by time axis. Thus, wall recovery time was defined and calculated with desorption energy and retention amount for each volume retention reaction.

As mentioned in earlier part, the definition of wall recovery time is that the time to consume

retention amount to be equilibrium in terms of wall, while, the definition of settling time of plasma property is that time to consume from onset of variation to end of variation of plasma property in terms of plasma. Intrinsically, the two types of time definitions are same. The wall recovery time obviously depends on type of retention reactions, which has different desorption energy as shown in Table 4-9. To estimate wall recovery time, two factors should be clearly defined including retention amount and corresponding desorption rate. Theoretical equation for recovery time is defined as equation (5.1) and equation (5.2). For the complete wall recovery condition, we can calculate approximate wall recovery time based on the desorption rate of each volume retention reaction from equation (5.3) to equation (5.6), which is estimated in present work. For the calculation, rate-determining step (RDS) should be considered that means lowest reaction rate governs total reaction rate because the recombination rate of hydrogen on tungsten is sometimes lower than the desorption rate, implying recycling flux is limited by recombination rate nevertheless desorption rate is sufficiently high. Hydrogen recombination rate is selected as value of Andrel *et al.* [67], [68] as most reliable value for polycrystalline tungsten. The recombination rate is as shown in equation (5.7). However, most of case of present work was done for the condition that desorption rate is lower than recombination.

The recovery time is calculated according to equation (5.1) or equation (5.2) depending whether the wall temperature is over boundary temperature or not. The boundary temperature is defined as the temperature that recombination rate become higher than lowest desorption rate along retention mechanisms. The higher the desorption energy, the lower the desorption rate. For the case of all reactions occur, the boundary temperature is about 1,350 K. Recovery time takes solution (equation (5.1)) for the wall temperature under 1,350 K while recovery time takes solution (equation (5.2)) for the wall temperature over 1,350 K. The difference between two solutions are not so much for the tungsten but it should be precisely defined for generalization of recovery time analysis. For present work, the wall temperature during wall recovery

experiment is about 780 K and the retention mechanisms takes all mechanism in Table 4-9. If we consider no chemical trapping, the boundary temperature is about 750 K.

$$\begin{aligned} t_{rec}(\text{influx} \to 0;\ \text{incomplete recovery}) &= \text{MAX.}\left[t_{rec}, i\right] \\ &= \text{MAX.}\left[N_{wall} / \left(C_{trap,i} \bullet K_{des}, i\left(E_{des,i}, T_{wall} \right) \right) \right] \end{aligned} \tag{5.1}$$

$$t_{rec}(\text{inf } lux \to 0;\ \text{complete recovery}) = \text{MAX.}\left[t_{rec}, i\right]$$

$$= \text{MAX.}\left[\frac{N_{wall} - C_{trap,i}\left(K_{trap,i}\left(T_{wall}, \text{outflux} \right) - K_{des,i}\left(E_{des,i}, T_{wall} \right) \right)}{C_{trap,i} \bullet K_{des}, i\left(E_{des,i}, T_{wall} \right)} \right] \tag{5.2}$$

$$\Gamma_H^{in,0} \times A = K_{des}^0(\mathrm{E}_{\mathrm{des},1}) = K_0 \bullet \exp\left(-0.89eV / kT\right) \tag{5.3}$$

$$\Gamma_H^{in,1} \times A = K_{des}^1(\mathrm{E}_{\mathrm{des},2}) = K_0 \bullet \exp\left(-1.84eV / kT\right) \tag{5.4}$$

$$\Gamma_H^{in,2} \times A = K_{des}^2(\mathrm{E}_{\mathrm{des},3}) = K_0 \bullet \exp\left(-2.33eV / kT\right) \tag{5.5}$$

$$\Gamma_H^{in,3} \times A = K_{des}^3(\mathrm{E}_{\mathrm{des},4}) = K_0 \bullet \exp\left(-2.39eV / kT\right) \tag{5.6}$$

$$K_{recomb} = 7.9 \times 10^{-15} \bullet \exp\left(-1.18eV / kT\right) \tag{5.7}$$

5.2 Temporally varying deuterium plasma with long-term volume hydrogen retention by deuterium recycling

Experiment for plasma variation due to wall recycling flux was performed with tungsten, carbon-impurity-implanted tungsten, and tungsten ion irradiated tungsten under deuterium plasma condition. The plasma variation was observed as increase of plasma density and decrease of electron temperature due to pressure increase effect near wall due to recycling of deuterium neutral gas from wall to plasma. The results were measured by Langmuir probe (LP) and thermo-couple. LP measured plasma density (n_e) and electron temperature (T_e) while thermo-couple measured target temperature. Targets consist of pristine tungsten, carbon-impurity-implanted tungsten, tungsten ion-irradiated tungsten. During recovery experiment, target tungsten temperature was sustained over the desorption temperature of hydrogen. Figure 5-1 shows that the temperature variation during recovery experiment.

The recovery time of wall is the time to complete recycling of deuterium from trapping site in tungsten. The value can be calculated by theoretical equation which is defined in this study. The equation is function of desorption energy, retention amount, and wall temperature including trapping site information such as fraction with respect to tungsten atom. However, only desorption energy is eigen value of specific retention reactions because the others such as retention amount can be varied depending on experiment condition. Thus, the wall recovery time needs desorption rate which is the function of desorption energy, which values were obtained from previous section by using TDS for specific plasma-tungsten interaction condition. The equation set show each desorption rate for different desorption energy. The wall recovery time can be compared to intrinsic diffusion time of deuterium from tungsten. It is the time to diffuse out of hydrogen from tungsten volume to outside. The value is a function of diffusion coefficient and the time as shown in equation (5.8)

$$\text{Diffusion length} = \sqrt{2Dt} \tag{5.8}$$

Thus, the characteristic diffusion length can be estimated as shown in Figure 5-2. In present work, all tungsten samples have thickness of 1 mm which is corresponding to ~ 1,000 sec of the characteristic diffusion time. Thus, if the recovery time scale is shorter than the characteristic diffusion, it will not be distinguished with characteristic diffusion time.

According to expected wall recovery time in Table 5-1, the recovery time for tungsten pristine will show indistinguishable wall recovery time because the wall recovery time is 0.0132 sec. It is because there is only intrinsic low desorption energy ($E_{des,0}$) for solution and D oversaturation induced vacancy trap ($E_{des,2}$). The time scale is shorter than characteristic time for diffusion (~1000 sec), thus, the wall recovery time will be measured as near 1,000 sec. While, the wall recovery time for tungsten with chemical trapping will show the long-term scale wall recovery time because there is higher desorption energy ($E_{des,3}$) as well as intrinsic desorption energies. Expected value is about 2,530 sec. Furthermore, the wall recovery time for tungsten irradiated by tungsten ions will show longest wall recovery time because there is highest desorption energy ($E_{des,4}$). The expected value is about 12,900 sec.

Figure 5-3 shows the experimental results of temporal plasma variation due to wall recycling effect. Firstly, case of tungsten pristine (black dot) shows very short wall recovery time scale about 1200 sec, implying that wall influx resulted from retention was consumed in short time scale. The maximum variation of plasma density is about 20% and the maximum variation of electron temperature is about 10%. Contrary to tungsten pristine case, tungsten with chemical trapping case (red dot) shows longer scale wall recovery during ~2,400 sec. The values correspond to theoretically expected value (2,530 sec) in Table 5-1. The maximum variation of plasma density is about 45% and the maximum variation of electron temperature is 20%. In

addition, the case of tungsten with defect trapping (blue dot) shows longest scale of wall recovery during ~ 12,600 sec. The maximum variation of plasma density is about 60% and the maximum variation of electron temperature is 25%. The value also corresponds to theoretically expected value (12,900 sec). Overall results indicate that the wall recycling flux changed near-wall plasma by neutral gas flux into plasma side. In addition, the recovery time is obviously depended on the volume retention reactions because it determines desorption rate and retention amount in tungsten.

Therefore, it can be understood that the plasma variation can be expected with wall volume reactions in long-term operation condition. In other words, plasma variation cannot be explained with particle balance between plasma to wall surface if the wall experience changes of volume reaction such as hydrogen retention.

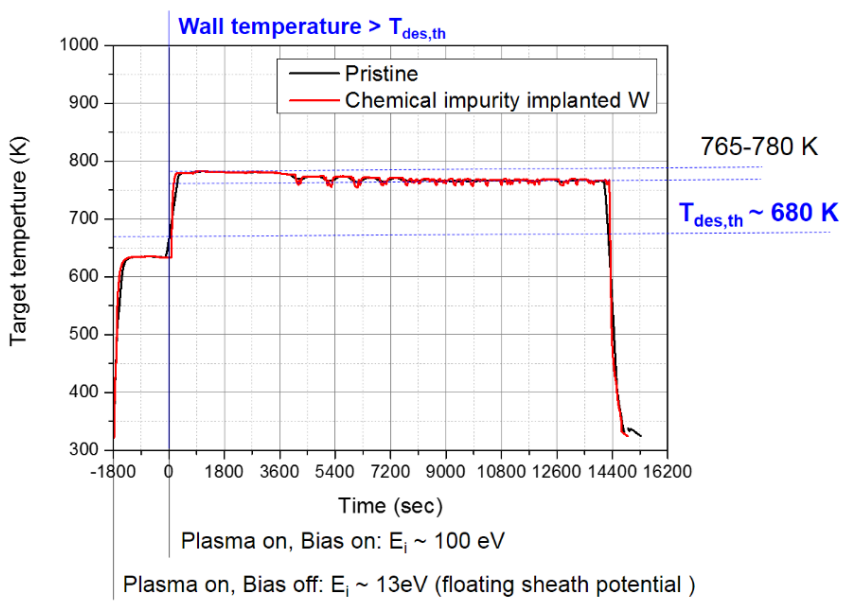

Figure 5-1. Variation of target tungsten temperature during recovery experiment. The target tungsten temperature is about 765-780 K which is over the minimum desorption temperature (680 K) of hydrogen from trapping site in tungsten.

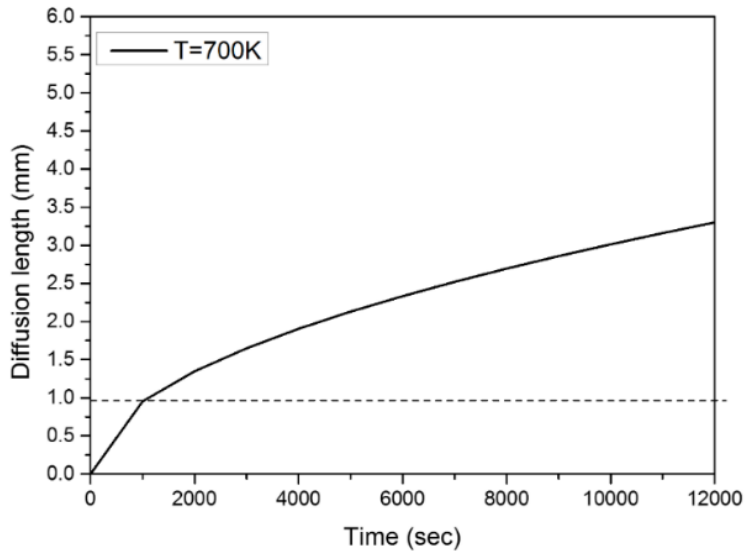

Figure 5-2. Characteristic diffusion time for deuterium in tungsten material at specific temperature condition. The value was calculated with analytical formula for 700 K, which temperature is corresponding with experimental condition. X-axis denotes the time of characteristic diffusion of deuterium in tungsten while Y-axis stands for deuterium diffusion length in tungsten, which is a function of time and temperature.

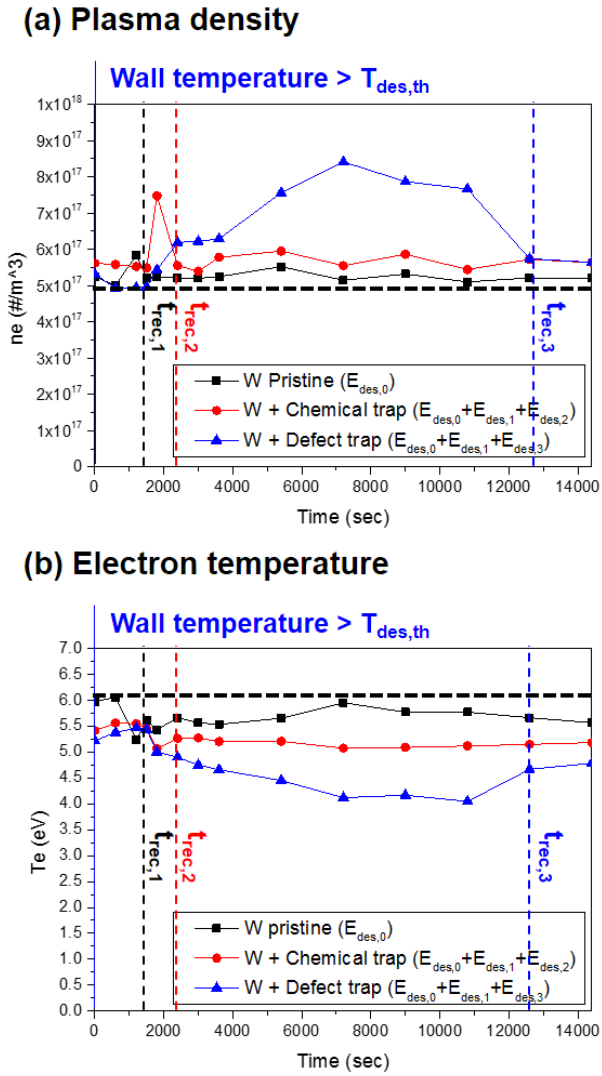

Figure 5-3. Temporally varying plasma property which facing tungsten target after deuterium plasma irradiation. Properties are consisting of (a) plasma density and (b) electron temperature. X-axis denotes the time from the onset of wall recovery under deuterium plasma irradiation after pre-irradiation. Two of Y-axis are stand for the plasma density and electron temperature. Recovery times are denoted by $t_{rec,1}$, $t_{rec,2}$, and $t_{rec,3}$ for each desorption energy ($E_{des,1}$, $E_{des,2}$, $E_{des,3}$)

Table 5-1. Expected and measured recovery time for specific tungsten condition after different plasma-tungsten interaction including long-term volume retention reaction (chemical trap, defect trap).

PWI conditions	**Expected wall recovery time (Model) = settling time of plasma property**		**Measured wall recovery time (Experiment)**
	$t_{rec,i}$ = f(retention parameter; $E_{des,i}$, $N_{wall,i}$ from TDS)	t_{rec} = Max [$t_{rec,i}$]	
Case.1 Deuterium plasma exposure onto tungsten ($E_{des,0}$ only)	$E_{des,0}$ (0.85 eV), $N_{wall,0}$ (2.13 x 10^{20}) ➔ 3.22 x 10^{-7} sec	$t_{rec,i}$ ~ 1,000 sec	$t_{rec,i}$ ~ 1,200 sec
	$E_{des,1}$ (1.84 eV), $N_{wall,0}$ (2.18 x 10^{20}) ➔ 1.32 x 10^{-2} sec		
	-		
Case.2 Deuterium plasma exposure onto carbon-implanted tungsten ($E_{des,0}$, $E_{des,1}$, $E_{des,2}$)	$E_{des,0}$ (0.85 eV), $N_{wall,0}$ (2.61 x 10^{21}) ➔ 3.95 x 10^{-6} sec	$t_{rec,i}$ ~ 2,530 sec	$t_{rec,i}$ ~ 2,400 sec
	$E_{des,1}$ (1.84 eV), $N_{wall,1}$ (1.12 x 10^{22}) ➔ 6.76 x 10^{-1} sec		
	$E_{des,2}$ (2.33 eV), $N_{wall,2}$ (4.60 x 10^{21}) ➔ 2.53 x 10^{3} sec		
Case.2 Deuterium plasma exposure onto defect-formed tungsten ($E_{des,0}$, $E_{des,1}$, $E_{des,3}$)	$E_{des,0}$ (0.85 eV), $N_{wall,0}$ (5.21 x 10^{20}) ➔ 7.88 x 10^{-6} sec	$t_{rec,i}$ ~ 12,900 sec	$t_{rec,i}$ ~ 12,600 sec
	$E_{des,1}$ (1.84 eV), $N_{wall,1}$ (2.53 x 10^{21}) ➔ 6.10 x 10^{-1} sec		
	$E_{des,3}$ (2.39 eV), $N_{wall,3}$ (1.01 x 10^{22}) ➔ 1.29 x 10^{4} sec		

5.3 Temporally varying deuterium plasma with fusion relevant admixing gas effects

The recovery time for admixing gas condition is hard to be observed by electrical Langmuir probe method because the additional gas ion current disturb the plasma density nevertheless the target to observe is only for deuterium plasma. Thus, the recovery time with variation effect case was observed by optical emission spectroscopy (OES) method, which is independent with perturbation of mixed ions, but it mainly depends on electron density and electron temperature. The full OES spectra of various hydrogen plasma are arranged in Figure 5-4 (a). The Figure 5-4 (b) shows the most significant line with high signal to noise ratio of HI line at 656.27 nm. The variation of HI line was considered as evidence of recycled hydrogen gas. The integration time (50 msec) and sampling (100) are consistent for all experiment.

The expected wall recovery time is arranged in Table 5-2. The expected time was estimated with different retention amount and consistent desorption energy because there is no additional desorption energy for tungsten irradiated with admixing gas condition. The observed recovery time for different condition show no significant difference between them. The results imply that the effect of fusion-relevant gas is effective on reduction of retention amount but it cannot change the recycling flux. For fusion application, we can conclude that the usage of admixing gas for advanced operating scenario is effective for stable operation with reducing wall tritium inventory.

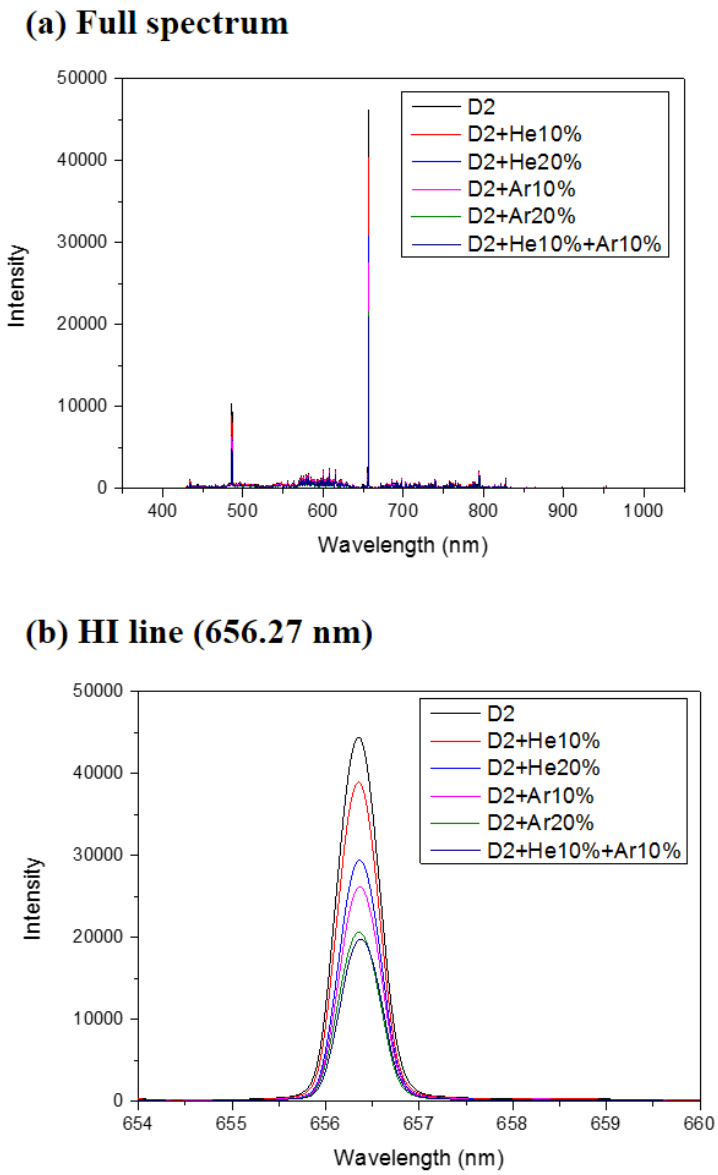

Figure 5-4. OES spectrum of hydrogen plasma with various admixing gas condition. The time of observation is at the starting time (~0 min) of recovery experiment. (a) full spectrum of OES spectra form various admixing condition, (b) Focused spectrum for HI line (656.27 nm).

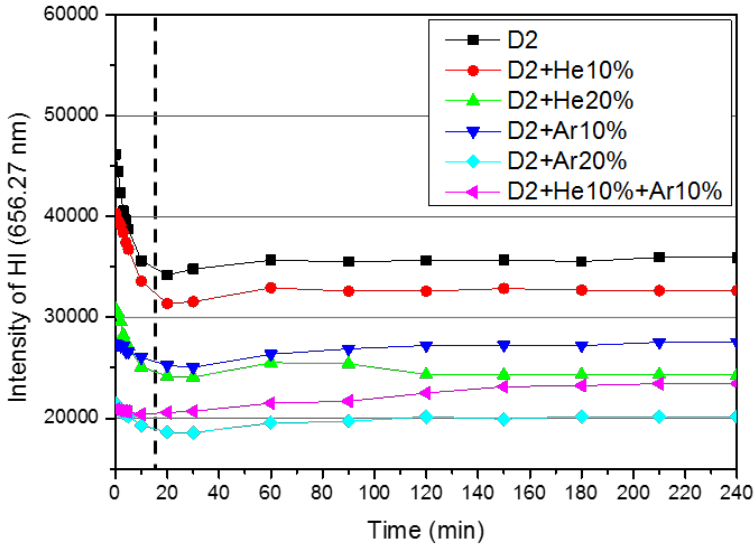

Figure 5-5. Time-varying intensity of OES for HI line (656.27 nm) for different admixing condition measured during recovery experiment. The integration time and the number of sample average are 100 msec and 50 samples.

Table 5-2. Expected and measured recovery time for specific tungsten condition after different plasma-tungsten interaction including admixing gas effect (Helium, Argon).

PWI conditions	**Expected wall recovery time (Model) = settling time of plasma property**		**Measured wall recovery time (Experiment)**
	$t_{rec,i}$ = f(retention parameter; $E_{des,i}$, $N_{wall,i}$ from TDS)	t_{rec} = Max [$t_{rec,i}$]	
Case.1 Deuterium plasma exposure onto tungsten ($E_{des,0}$ only)	$E_{des,0}$ (0.85 eV), $N_{wall,0}$ (2.13 x 10^{20}) ➔ 3.22 x 10^{-7} sec	$t_{rec,i}$ ~ 1,000 sec	$t_{rec,i}$ ~ 1,200 sec
	$E_{des,1}$ (1.84 eV), $N_{wall,0}$ (2.18 x 10^{20}) ➔ 1.32 x 10^{-2} sec		
	--		
Case.2 He (10%) gas-admixed deuterium plasma exposure onto tungsten (E_{des0}, E_{des1})	$E_{des,0}$ (0.85 eV), $N_{wall,0}$ (1.41 x 10^{20}) ➔ 2.13 x 10^{-7}sec	$t_{rec,i}$ ~ 2,530 sec	$t_{rec,i}$ ~ 2,400 sec
	$E_{des,1}$ (1.84 eV), $N_{wall,0}$ (5.20 x 10^{19}) ➔ 3.14 x 10^{-3} sec		
	-		
Case.3 Ar (10%) gas-admixed deuterium plasma exposure onto tungsten (E_{des0}, E_{des1})	$E_{des,0}$ (0.85 eV), $N_{wall,0}$ (8.79 x 10^{19}) ➔ 1.33 x 10^{-7} sec	$t_{rec,i}$ ~ 12,900 sec	$t_{rec,i}$ ~ 12,600 sec
	$E_{des,1}$ (1.84 eV), $N_{wall,0}$ (1.23 x 10^{20}) ➔ 7.43 x 10^{-3} sec		
	-		

5.4 Spatial region of varying plasma by recycled hydrogen flux

To understand the effect of wall recycling on edge plasma properties, spatial variation of plasma density and electron temperature were observed with tungsten target after pre-irradiation for deuterium retention. Before experimental measurement, theoretical value of specific length scale was calculated with physics basis. The theoretical values including *Child-Langmuir* sheath thickness (s) from equation (5.9), collisional sheath thickness (s') from equation (5.10), ion-neutral mean free path ($\lambda_{i\text{-}n}$) from (5.11), neutral-neutral mean free path ($\lambda_{n\text{-}n}$) from (5.12). The sheath thickness was selected as basic dimension scale of plasma while the mean free path was selected considering the wall recycling causes neutral gas flux from tungsten to plasma side. The corresponding equations and value are included in Table 5-3. The value of recycling length which means the length from target material to plasma which has varying properties during wall recovery. The recycling length is defined as the distance from tungsten target to the point which show distortion of plasma property with respect to initial plasma property when there is no recycling deuterium particle.

Figure 5-6 shows the variation of both plasma density and electron temperature with the spatial position as distance from target in z-axis. The results show the obvious inflection point near 15-20 mm for the case of retention. The case of no retention shows no clear inflection point. According to that, the recycling length (L) can be defined experimentally as the distance from tungsten target to inflection point. With experimental results, Table 5-3 also show the comparison between recycling length scale and the characteristic physical length scale. The table show that the distance from wall to plasma where the variation of plasma density occur by hydrogen recycling is comparable to mean free path (MFP) between neutral particles (D_2),

resulting in that increased electron-impact ionization due to increased neutral (D_2) density. This observation implies that spatial variation of plasma property near wall material can be dominated by collision between plasma and neutrals, which is the function of pressure where near wall material. This fact improves the understanding about the effect of wall recycling on the variation of plasma property in space as well as time scale. Furthermore, the observation means that the recycling makes boundary region between plasma and wall material collisional boundary, implying variation can occur for ion outflux to wall as well as neutral influx from wall.

In conclusion of section 5, overall reactions and admixing effects are arranged with its effect on recycling as shown in Table 5-4. The information can be used to operating scenario as well as plasma-facing component design considering effective plasma-wall interaction which results in neutral gas recycling from wall during long-term operation.

Table 5-3. The characteristic physical length scale calculated by specific physical variables including the definition of sheath thickness and particle mean free path.

Definition	Value	w.r.t. L
Recycling length, *L*	15-20 mm	-
C-L sheath thickness, *s*	0.2 mm $$s \approx \left(\sqrt{2}/3\right)\lambda_{Ds}\left(2V_0/Te\right)^{3/4} \quad (5.9)$$	<< L
Collisional sheath thickness, *s'*	< 0.2 mm $$s' \approx \left(\pi K^3\right)^{1/2}\lambda_{Ds} \quad (5.10)$$	<< L
Ion (D_2^+)-Neutral (D_2) mean free path, λ_{i-n}	> 12.7 mm $$\lambda_{i-n} = 1/\left(\sum_i n_{i,n}\sigma_{i-n}\right) \quad (5.11)$$	~ L
Neutral (D_2)-Neutral (D_2) mean free path, λ_{n-n}	12.7 mm $$\lambda_{n-n} = 1/\left(\sum_i n_n\sigma_{n-n}\right) \quad (5.12)$$	~ L

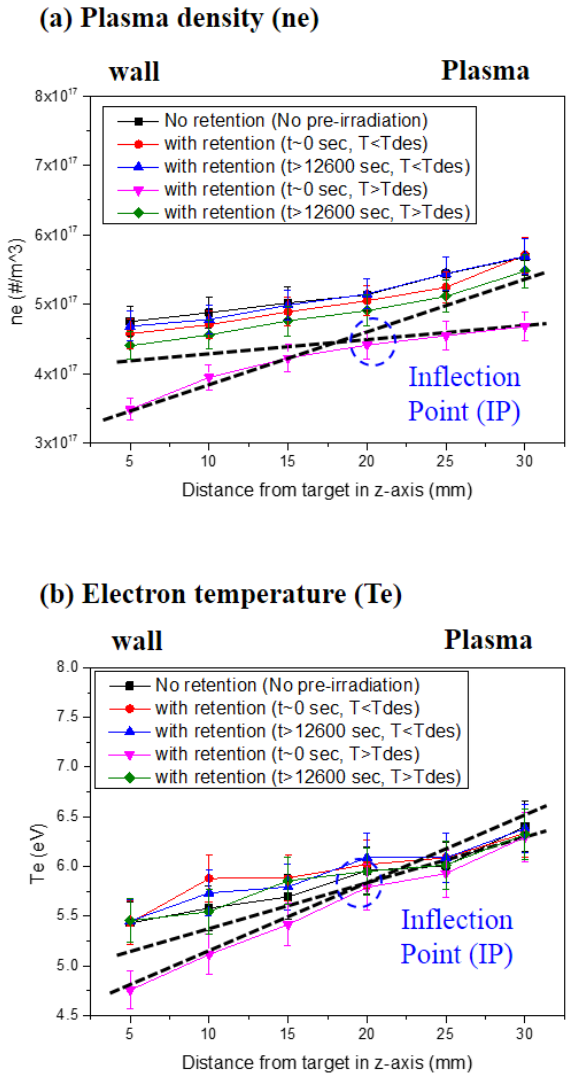

Figure 5-6. Spatial variation of (a) plasma density and (b) electron temperature measured by electrical Langmuir probe method. The condition consists of 1) no retention, 2) with retention (t~0 sec, $T<T_{des}$), 3) with retention (t>12,600 sec, $T>T_{des}$), 4) with retention (t~0 sec, $T>T_{des}$), 5) with retention (t>12,600 sec, $T>T_{des}$). The T denotes the temperature of tungsten target while the T_{des} is stands for the desorption temperature which is dependent on volume retention reaction.

Table 5-4 Summary of wall recovery experiment with dependence on volume retention reactions.

PWI conditions	**Long-term volume retention + variation effect**		**Recycling (Wall recovery)**		E_{des}	**Dimension**
	Phenomenon	Effect	t_{rec}	Effect		
D plasma exposure onto W	Intrinsic: Solution, Fabrication defect	W-D bond, dislocation trapping	< 1 sec	Short-term recovery	0.75-0.95 eV	Entire volume
D plasma exposure onto W (Fluence)	Extrinsic: Oversaturation	Vacancy trapping	< 1 sec	Short-term recovery	1.84 eV	Subsurface ~ few nm
D plasma exposure onto C-implanted W	Extrinsic: Impurity implantation	Chemical impurity trapping	~2,530 sec	Long-term recovery	2.33 eV	Subsurface ~ nm- μm
D plasma exposure onto defect-formed W	Extrinsic: Cascade collisional damage	Defect cluster trapping	~12,900 sec	Long-term recovery	2.39 eV	Volume ~ μm-mm
He gas-admixed D plasma exposure onto W	Variation: Diffusion barrier effect	Vacancy trapping, No ΔE_{des}	< 1 sec	Negligible	1.84 eV	Subsurface ~ few nm
Ar gas-	Variation:	All	< 1 sec	Negligible	all	Subsurface ~

admixed D plasma exposure onto W	Surface sputtering	trapping, No ΔE_{des}				nm- μm
D plasma exposure onto recrystallized W	Variation: Recrystallization	Dislocation trapping, No ΔE_{des}	< 1sec	Negligible	0.75-0.95 eV	Volume ~ μm-mm

5.5 Characteristics of the developed hydrogen retention model comparing to previous studies

Developed hydrogen retention model has distinguishable characteristics with respect to previous studies. The characteristics are arranged in Table 5-5. The characteristics can be defined with reactions in wall material, wall influx, and variation of hydrogen plasma properties.

For the reactions in wall material point of view, previous studies show simple reaction balance of gas dissociation and recombination as surface reactions. While, in this study, complete wall reactions including volume reactions are explained with study on volume retention reactions and corresponding desorption energies. For the wall influx point of view, previous studies showed that it calculated with simple particle balance without volume retention reactions in wall, thus, there is no explanation and they cannot expect the influx. While, in this study, it was expected with hydrogen retention model as a function of volume retention reactions for specific plasma-wall interaction condition. For the variation of hydrogen plasma properties point of view, previous study focused on the byproduct and materials particle. While, this study focused on discharge gas itself as an intrinsic cause of 'plasma drift'. Spatially and temporally varying plasma properties are explained by changed wall influx due to volume retention reactions.

The limitation of this study is that developed model is expectable for hydrogen recycling as a function of long-term volume retention, however, it only expects settling time of plasma property using wall recovery time but it cannot expect absolute variation amount because it is also function of plasma reactions which can be estimated with power balance as well as particle balance. In addition, it is 0-dimensional model hence it will be better to extend from 0 dimensional to 1 or 2-dimensional model to consider system configuration.

Table 5-5. Comparison between previous study and this dissertation.

Characteristics	Previous Studies	This Dissertation
Reactions in wall material	Simple reaction balance of gas dissociation and recombination as surface reactions.	Complete wall reactions including volume reactions are explained with study on volume retention reactions and corresponding desorption energies.
Wall influx	Calculated with simple particle balance without wall retention model. No explain. Can't expect.	Expected with hydrogen retention model as a function of volume retention parameter (Desorption energy) for specific plasma-wall interaction condition.
Variation of hydrogen plasma properties	Focused on byproduct (residue) and material's particle	Focused on discharge gas itself as an intrinsic cause of 'plasma drift'. Temporally varying plasma properties ($T_e \downarrow$, $n_e \uparrow$) are explained by changed wall influx due to volume retention reactions.

Chapter 6 . Conclusion

The hydrogen retention model was developed to explain temporal and spatial variation of hydrogen plasma properties (n_e, T_e) using hydrogen particle balance equation. The volume retention reactions were considered as a cause of neutral gas influx from wall to plasma of particle balance equation, which is function of desorption energies. The desorption energies can be experimentally obtained by thermal desorption spectroscopy (TDS) for various plasma-wall interaction (PWI) conditions. The PWI conditions consist of deuterium plasma exposure onto tungsten, deuterium plasma exposure onto carbon-implanted tungsten, deuterium plasma exposure onto defect-formed tungsten, gas-admixed ($P_{He\ or\ Ar}$ ~10-20%) deuterium plasma exposure onto tungsten, deuterium plasma exposure onto recrystallized tungsten.

Hydrogen retention reactions in tungsten were figured out with corresponding desorption energies; hydrogen solution ($E_{des,0}$: 0.75-0.95 eV), hydrogen oversaturation-induced vacancy trapping ($E_{des,1}$: 1.84 eV), carbon impurity-induced chemical trapping ($E_{des,2}$: 2.33 eV), physical damage-induced defect cluster trapping ($E_{des,3}$: 2.39 eV). In terms of variation effect in fusion-relevant condition, both He ash and Ar puffing gas effects were indirectly understood by using admixing condition; by surface modification and sputtering, both gases reduce retention amount (ΔN_{wall}=50-90%), which is over the density variation of admixed plasma (Δn_e=10-20%). However, both gases do not change the desorption energy ($\Delta E_{des,i}$=0). For the same point of view, the effect of tungsten recrystallization was also analysed that can reduce hydrogen retention amount (ΔN_{wall}=30-50%) due to reduced fabrication-defects without the change of desorption energy ($\Delta E_{des,i}$=0). The dimensions of volume retentions were extended from subsurface (nm ~ μm) to bulk (μm ~ mm) depending on incident energy of implanted plasma

ions (100 eV/D_2^+), impurity ions (300-400 eV/C^{4+}), and high energy ions (2.8 MeV/W^{2+}). Because the results clearly show the wall volume reaction is function of PWI condition, wall condition is not the fixed boundary condition.

Based on hydrogen retention model with experimentally obtained desorption energy data, temporal variation of plasma was expected and explained as a function of desorption energy of volume retention reactions. The wall recovery time, which means time to be equilibrium of plasma variation resulted from recycling of retained hydrogen particles, shows proportional relationship with desorption energy from ~1 sec to ~14,000 sec. The spatial variation of plasma was understood with distance from wall to plasma, where the variation of plasma density occur by hydrogen recycling, is comparable to mean free path (MFP) between neutral particles (D_2). The collisions within MFP result in that increased electron-impact ionization due to increased neutral (D_2) density. Hence the expectation of plasma variation requires information about wall volume retention reaction, which can have more significant importance for long-term operation condition with various PWI. This dissertation extends boundary definition of plasma system from plasma-to-wall surface to plasma-to-wall volume by considering volume retention reactions for particle balance equation. The adoption of hydrogen retention model can be a strategy to operate plasma system with higher reproducibility for long-term operation by expecting variation of plasma with variation of wall volume reactions.

Bibliography

[1] R. A. Causey, “Hydrogen isotope retention and recycling in fusion reactor plasma-facing components,” *J. Nucl. Mater.*, vol. 300, no. 2–3, pp. 91–117, 2002.

[2] K. Schmid, K. Krieger, S. W. Lisgo, G. Meisl, S. Brezinsek, and J. E. T. Contributors, “WALLDYN simulations of global impurity migration in JET and extrapolations to ITER,” *Nucl. Fusion*, vol. 55, no. 5, p. 53015, 2015.

[3] T. Tanabe, “Review of hydrogen retention in tungsten,” *Phys. Scr.*, vol. T159, p. 14044, 2014.

[4] Y. Yu *et al.*, “First comprehensive particle balance study in KSTAR with a full graphite first wall and diverted plasmas,” *Plasma Phys. Control. Fusion*, vol. 54, no. 10, p. 105006, 2012.

[5] K. Schmid, K. Krieger, S. W. Lisgo, G. Meisl, and S. Brezinsek, “Quantitative modeling of fuel retention in the JET-C and JET-ILW wall configurations by WallDYN and predictions for ITER,” *J. Nucl. Mater.*, vol. 463, pp. 66–72, 2015.

[6] K. Schmid, K. Krieger, S. W. Lisgo, S. Brezinsek, and J. E. Contributors, “Quantitative modeling of fuel retention in the JET-C and JET-ILW wall configurations by WallDYN and predictions for ITER,” *21st Int. Conf. Plasma Surf. Interact. Control. Fusion Devices PSI-2014*, p. I6, 2014.

[7] M. J. Baldwin and R. P. Doerner, “Helium induced nanoscopic morphology on tungsten under fusion relevant plasma conditions,” *Nucl. Fusion*, vol.

48, no. 3, p. 35001, 2008.

[8] J. Roth *et al.*, "Tritium inventory in ITER plasma-facing materials and tritium removal procedures," *Plasma Phys. Control. Fusion*, vol. 50, no. 10, p. 103001, 2008.

[9] D. Douai *et al.*, "Wall conditioning for ITER: Current experimental and modeling activities," *J. Nucl. Mater.*, vol. 463, pp. 150–156, 2015.

[10] M. J. Baldwin, R. P. Doerner, W. R. Wampler, D. Nishijima, T. Lynch, and M. Miyamoto, "Effect of He on D retention in W exposed to low-energy, high-fluence (D, He, Ar) mixture plasmas," *Nucl. Fusion*, vol. 51, no. 10, p. 103021, 2011.

[11] Z. Tian, J. W. Davis, and a. a. Haasz, "Deuterium retention in tungsten at fluences of up to 1026 D+/m2 using D+ ion beams," *J. Nucl. Mater.*, vol. 399, no. 1, pp. 101–107, Apr. 2010.

[12] P. A. Redhead, "Thermal desorption of gases," *Vacuum*, vol. 12, no. 4, pp. 203–211, 1962.

[13] Y. Jin *et al.*, "Observation of oversaturation-induced defect formation in tungsten irradiated by low energy deuterium ion," *J. Korean Phys. Soc.*, vol. 69, no. 4, pp. 518–524, 2016.

[14] H. Fujita *et al.*, "Effect of neutron energy and fluence on deuterium retention behaviour in neutron irradiated tungsten," *Phys. Scr.*, vol. T167, pp. 014068–014072, 2016.

[15] D. F. Johnson and E. A. Carter, "Hydrogen in tungsten: Absorption, diffusion, vacancy trapping, and decohesion," *J. Mater. Res.*, vol. 25, no. 2, pp. 315–327, 2010.

[16] K. Heinola, T. Ahlgren, K. Nordlund, and J. Keinonen, "Hydrogen interaction with point defects in tungsten," *Phys. Rev. B*, vol. 82, no. 9, p. 94102, Sep.

2010.

[17] O. V. Ogorodnikova, J. Roth, and M. Mayer, “Ion-driven deuterium retention in tungsten,” *J. Appl. Phys.*, vol. 103, no. 2008, p. 34902, 2008.

[18] D. F. Johnson and E. A. Carter, “Hydrogen in tungsten: Absorption, diffusion, vacancy trapping, and decohesion,” *J. Mater. Res.*, vol. 25, no. 2, pp. 315–327, 2010.

[19] H. Fujita *et al.*, “Effect of neutron energy and fluence on deuterium retention behaviour in neutron irradiated tungsten,” *Phys. Scr.*, vol. T167, p. 14068, 2016.

[20] H. Atsumi, “Hydrogen retention in graphite and carbon materials under a fusion reactor environment,” *J. Nucl. Mater.*, vol. 313–316, no. SUPPL., pp. 543–547, 2003.

[21] R. A. Causet and T. J. Venhaus, “The Use of Tungsten in Fusion Reactors: A Review of the Hydrogen Retention and Migration Properties,” *Phys. Scr.*, vol. T94, no. 1, p. 9, 2001.

[22] J. Roth and K. Schmid, “Hydrogen in tungsten as plasma-facing material,” *Phys. Scr.*, vol. T145, p. 14031, 2011.

[23] Z. Tian, J. W. Davis, and a. a. Haasz, “Deuterium retention in tungsten at fluences of up to 1026 D+/m2 using D+ ion beams,” *J. Nucl. Mater.*, vol. 399, no. 1, pp. 101–107, Apr. 2010.

[24] Y. Hatano *et al.*, “Retention of Hydrogen Isotopes in Neutron Irradiated Tungsten,” *Mater. Trans.*, vol. 54, no. 4, pp. 437–441, 2013.

[25] Y.-N. Liu *et al.*, “Mechanism of vacancy formation induced by hydrogen in tungsten,” *AIP Adv.*, vol. 3, no. 12, p. 122111, 2013.

[26] S.-Y. Qin, S. Jin, L. Sun, H.-B. Zhou, Y. Zhang, and G.-H. Lu,

"Hydrogen assisted vacancy formation in tungsten: A first-principles investigation," *J. Nucl. Mater.*, vol. 465, pp. 135–141, Oct. 2015.

[27] S. T. Lim, H. S. Kim, Y. Jin, J. Y. Lee, J. M. Song, and G. H. Kim, "Investigation of SOL plasma interaction with graphite PFC," *J. Nucl. Mater.*, vol. 463, pp. 753–756, 2015.

[28] F. F. Chen, "Numerical computations for ion probe characteristics in a collisionless plasma," *J. Nucl. Energy. Part C, Plasma Physics, Accel. Thermonucl. Res.*, vol. 7, no. 1, pp. 47–67, 1965.

[29] J. G. Bak, H. S. Kim, J. Kim, K. I. You, S. H. Hong, and M. K. Bae, "SOL parameters, and particle and heat fluxes at divertor targets from electric probe measurements in KSTAR," *J. Korean Phys. Soc.*, vol. 65, no. 8, pp. 1232–1238, 2014.

[30] J. F. Ziegler, M. D. Ziegler, and J. P. Biersack, "SRIM - The stopping and range of ions in matter," *Nucl. Instruments Methods Phys. Res. Sect. B Beam Interact. with Mater. Atoms*, vol. 268, no. 11–12, pp. 1818–1823, 2010.

[31] W. M. Shu, G.-N. Luo, and T. Yamanishi, "Mechanisms of retention and blistering in near-surface region of tungsten exposed to high flux deuterium plasmas of tens of eV," *J. Nucl. Mater.*, vol. 367–370, pp. 1463–1467, Aug. 2007.

[32] A. H. M. Krom and A. Bakker, "Hydrogen trapping models in steel," *Metall. Mater. Trans. B*, vol. 31, no. 6, pp. 1475–1482, 2000.

[33] R. G. Wilson, "SIMS quantification in Si, GaAs, and diamond - an update," *Int. J. Mass Spectrom. Ion Process.*, vol. 143, no. C, pp. 43–49, 1995.

[34] R. Neu *et al.*, "Overview on plasma operation with a full tungsten wall in ASDEX Upgrade," *J. Nucl. Mater.*, vol. 438, pp. S34–S41, 2013.

[35] J. Roth *et al.*, "Recent analysis of key plasma wall interactions issues for

ITER," *J. Nucl. Mater.*, vol. 390–91, pp. 1–9, 2009.

[36] J. Roth *et al.*, "Tritium inventory in ITER plasma-facing materials and tritium removal procedures," *Plasma Phys. Control. Fusion*, vol. 50, no. 10, p. 103001, 2008.

[37] G. J. van Rooij *et al.*, "Tungsten divertor erosion in all metal devices: Lessons from the ITER like wall of JET," *J. Nucl. Mater.*, vol. 438, pp. S42–S47, Jul. 2013.

[38] W.-H. Ko *et al.*, "Ion temperature and toroidal velocity edge transport barriers in KSTAR," *Nucl. Fusion*, vol. 55, no. 8, p. 83013, 2015.

[39] Y. Oya *et al.*, "Impact of temperature during He+ implantation on deuterium retention in tungsten, tungsten with carbon deposit and tungsten carbide," *Phys. Scr.*, vol. T167, p. 14037, 2016.

[40] O. V. Ogorodnikova, J. Roth, and M. Mayer, "Deuterium retention in tungsten in dependence of the surface conditions," *J. Nucl. Mater.*, vol. 313–316, pp. 469–477, Mar. 2003.

[41] V. K. Alimov *et al.*, "Deuterium retention in tungsten exposed to low-energy, high-flux clean and carbon-seeded deuterium plasmas," *J. Nucl. Mater.*, vol. 375, no. 2, pp. 192–201, Apr. 2008.

[42] M. Fukumoto, T. Nakano, Y. Ueda, K. Itami, and H. Kubo, "Deuterium retention in tungsten coating irradiated by deuterium and carbon ions," *J. Nucl. Mater.*, vol. 462, pp. 354–359, 2015.

[43] S. H. Son *et al.*, "Multi-purpose mid-plane manipulator for plasma surface interaction research in KSTAR," *Fusion Eng. Des.*, vol. 109–111, no. PartA, pp. 286–289, 2016.

[44] G. Federici *et al.*, "Plasma-material interactions in current tokamaks and

their implications for next step fusion reactors," *Nucl. Fusion*, vol. 41, no. 12R, pp. 1967–2137, 1967.

[45] H. K. Na, S. Sajjad, J. M. Park, and M. Kwon, "Configuration and installation design of optical diagnostic systems on KSTAR," *Fusion Eng. Des.*, vol. 86, no. 1, pp. 66–70, 2011.

[46] R. J. Colchin, D. L. Hillis, R. Maingi, C. C. Klepper, and N. H. Brooks, "The filterscope," *Rev. Sci. Instrum.*, vol. 74, no. 3 II, pp. 2068–2070, 2003.

[47] E. N. Bang *et al.*, "Temporal and Spatial PFC Temperature Profiles in KSTAR 2010," *IEEE Trans. Plasma Sci.*, vol. 40, no. 6, pp. 1768–1772, Jun. 2012.

[48] J. G. Bak *et al.*, "Investigation of SOL parameters and divertor particle flux from electric probe measurements in KSTAR," *J. Nucl. Mater.*, vol. 463, pp. 10–13, 2014.

[49] J. G. Bak *et al.*, "Investigation of SOL parameters and divertor particle flux from electric probe measurements in KSTAR," *J. Nucl. Mater.*, vol. 463, pp. 424–427, 2015.

[50] Y. Jin, S. Choi, S. J. Yang, C. R. Park, and G. H. Kim, "Effect of helmholtz oscillation on auto-shroud for APS tungsten carbide coating," *J. Therm. Spray Technol.*, vol. 22, no. 5, pp. 756–763, 2013.

[51] J. Luthin, H. Plank, J. Roth, and C. Linsmeier, "Ion beam-induced carbide formation at the the titanium-carbon interface," *Nucl. Instruments Methods Phys. Res. Sect. B Beam Interact. with Mater. Atoms*, vol. 182, no. 1–4, pp. 218–226, 2001.

[52] A. Warren, A. Nylund, and I. Olefjord, "Oxidation of tungsten and tungsten carbide in dry and humid atmospheres," *Int. J. Refract. Met. Hard Mater.*, vol. 14, pp. 345–353, 1996.

[53] G. Federici *et al.*, "Key ITER plasma edge and plasma-material interaction issues," *J. Nucl. Mater.*, vol. 313–316, no. SUPPL., pp. 11–22, 2003.

[54] D. Naujoks *et al.*, "Tungsten as target material in fusion devices," *Nucl. Fusion*, vol. 36, no. 6, pp. 671–687, 1996.

[55] O. V. Ogorodnikova, B. Tyburska, V. K. Alimov, and K. Ertl, "The influence of radiation damage on the plasma-induced deuterium retention in self-implanted tungsten," *J. Nucl. Mater.*, vol. 415, no. 1, pp. S661–S666, Aug. 2011.

[56] J. Roth *et al.*, "Tritium inventory in ITER plasma-facing materials and tritium removal procedures," *Plasma Phys. Control. Fusion*, vol. 50, no. 10, p. 103001, 2008.

[57] O. Gruber *et al.*, "Compatibility of ITER scenarios with full tungsten wall in ASDEX Upgrade," *Nucl. Fusion*, vol. 49, no. 11, p. 115014, 2009.

[58] A. J. E. Foreman and B. N. Singh, "The role of collision cascades and helium atoms in cavity nucleation," *Radiat. Eff. Defects Solids*, vol. 113, no. 1–3, pp. 175–194, 1990.

[59] Y. Hatano *et al.*, "Deuterium trapping at defects created with neutron and ion irradiations in tungsten," *Nucl. Fusion*, vol. 53, no. 7, p. 73006, 2013.

[60] J. P. Roszell, J. W. Davis, V. K. Alimov, K. Sugiyama, and A. A. Haasz, "Deuterium retention in single-crystal tungsten irradiated with 10-500 eV/D+," *J. Nucl. Mater.*, vol. 438, no. SUPPL, pp. S1084–S1087, 2013.

[61] E. Markina, M. Mayer, A. Manhard, and T. Schwarz-Selinger, "Recovery temperatures of defects in tungsten created by self-implantation," *J. Nucl. Mater.*, vol. 463, pp. 329–332, 2014.

[62] M. Poon, A. A. Haasz, and J. W. Davis, "Modelling deuterium release during thermal desorption of D+-irradiated tungsten," *J. Nucl. Mater.*, vol. 374, no. 3,

pp. 390–402, 2008.

[63] T. Oda, “Thermodynamic model for grain boundary effects on hydrogen solubility, diffusivity and permeability in poly-crystalline tungsten,” *Fusion Eng. Des.*, vol. 112, pp. 102–116, Nov. 2016.

[64] T. Ahlgren, K. Heinola, N. Juslin, and A. Kuronen, “Bond-order potential for point and extended defect simulations in tungsten,” *J. Appl. Phys.*, vol. 107, no. 3, p. 33516, 2010.

[65] J. A. Brinkman, “Production of Atomic Displacements by High-Energy Particles,” *Am. J. Phys.*, vol. 24, no. 4, p. 246, 1956.

[66] A. Suslova, O. El-Atwani, D. Sagapuram, S. S. Harilal, and A. Hassanein, “Recrystallization and grain growth induced by ELMs-like transient heat loads in deformed tungsten samples,” *Sci. Rep.*, vol. 4, pp. 1–10, 2014.

[67] B. J. Merrill, M. Shimada, and P. W. Humrickhouse, “Simulating Tritium Retention in Tungsten with a Multiple Trap Model in the TMAP Code,” *Plasma Fusion Res.*, vol. 10, pp. 71–75, 2013.

[68] R. A. Anderl, D. F. Holland, G. R. Longhurst, R. J. Pawelko, C. L. Trybus, and C. H. Sellers, “Deuterium transport and trapping in polycrystalline tungsten,” *Fusion Technol.*, vol. 21, pp. 745–752, 1992.

초 록

본 연구에서는 플라즈마와 벽면 재료 간에 발생 할 수 있는 수소 방출속과 유입속에 대한 함수가 고려된 입자균형식 형태의 수소흡착 모델이 개발되었다. 모델의 지배 방정식인 입자균형식에서 벽면으로부터 플라즈마로의 수소 중성가스 유입속은 수소 흡착과 탈착 반응율의 결정인자인 수소 재방출 에너지에 의해 결정되었다. 수소 흡착 반응은 플라즈마-벽면 상호작용의 조건에 따라 상이하게 나타나며 주로 재료 표면 보다는 공간내에서 장주기 흡착반응의 형태로 형성되어 운전중 점진적으로 수소 중성 가스를 방출시킨다.

개발된 수소 흡착 모델은 플라즈마와 벽면 재료간 경계 조건이 운전중 벽면에서 발생하는 중성가스 유입에 의해 변화하고, 그 결과로 플라즈마 밀도 등의 특성이 바뀔 수 있음을 전제로 한다. 해당 유입은 벽면 재료의 공간내에서 흡착되었던 수소가 재방출되면서 발생하며 흡착 반응의 종류에 의존한다. 수소흡착 반응 종류는 각 플라즈마-벽면 상호작용 조건에 따라 따르게 형성되며, 해당반응들은 반응율의 결정인자인 재방출 에너지에 의해 지배된다. 따라서 수소 흡착 모델은 벽면 재료내 흡착 반응 종류와 재방출 에너지 정보들을 바탕으로 근방 수소 플라즈마의 물성 변화를 예측하는 것을 목표로 구축되었다.

수소흡착 모델을 구성하기 위해 실험은 대표적인 플라즈마-벽면 상호작용 조건인 중수소 플라즈마-텅스텐, 중수소 플라즈마-불순물 주입 텅스텐, 중수소 플라즈마-손상 텅스텐, 외부 가스 혼입된 중수소 플라즈마-텅스텐, 중수소 플라즈마-재결정화된 텅스텐 대면 조건에서 수행되었다. 수소 흡착율의 결정인자인 재방출 에너지는 해당 플라즈마 대면 조건에서 발생하는 공간 수소 흡착 반응들에 대해 자체적으로 개발되고 방법론의 정립을 거쳐 정확도를

향상시킨 열탈착 분광계를 바탕으로 진단되었다. 본 연구의 수소 흡착 반응에 대한 연구 결과는 텅스텐 재료내에서의 주요한 수소 흡착반응들이 수소 용해 (0.75-0.95 eV), 수소 과포화에 따른 점 결함과 수소간 흡착 (1.84 eV), 운전중 침투에 따른 불순물과 수소간 화학적 흡착 (2.33 eV), 손상에 따른 결함 군집과 수소간 흡착 (2.39 eV)으로 구성되며 각 반응은 서로 다른 수소 재방출 에너지를 가짐을 규명하였다. 일반적인 조건 외에, 핵융합로에서 특수하게 발생할 수 있는 헬륨 재 및 아르곤 주입가스 효과를 간접적으로 확인하기 위해 플라즈마 밀도 변동이 20% 미만인 조건에서 중수소 가스에 혼합해준 수소흡착 실험의 텅스텐내 수소 재방출 에너지는 변동되지 않았으며, 공통적으로 플라즈마 밀도 변동분 보다 큰 50-90% 이상의 수소 흡착량의 감소를 유발함이 확인되었다. 이러한 경향은 재결정화 텅스텐 조건에서도 동일하게 관찰되었으며, 제조시 발생결함이 재결정화층 내에서 소멸됨이 그 원인 현상으로 확인되었다.

실험적으로 얻은 수소 흡착 반응 종류 및 재방출 에너지 데이터를 바탕으로, 플라즈마 특성치인 플라즈마 밀도와 전자밀도에 대한 시변동 특성 시간인 벽면 회복 시간은 수소 재방출 에너지의 함수임이 실험과 모델간 상호 검증되었다. 흡착 후 재방출되는 수소 중성 가스에 따른 플라즈마의 변동이 종료되는 시간을 의미하는 벽면 포화시간은 수소 흡착 반응의 재방출 에너지에 비례하여 장주기가 되는 특성을 보였다. 해당 변동이 발생하는 공간적 영역은 벽면 재료로부터 플라즈마 사이에 중성가스 간의 평균 자유 행정 거리에 해당하므로 재방출로 증가한 수소 중성가스 밀도에 의한 전자-충돌 이온화 반응의 증가가 플라즈마 밀도 변동을 야기했음을 확인할 수 있었다.

이상의 현상은 벽면 재료 공간내에서 발생하는 수소 흡착모델을 고려하지 않은 기존의 입자균형식의 개념에서는 설명되지 않는다. 따라서, 본 연구는 특히 장주기 운전에서는 벽면재료 공간 내에서의 반응에 대한 해석이 포함되어야만 플라즈마 밀도나 전자 온도 등의 플라즈마 물성의 변동을 예측할 수 있음을

입증하였다. 개발된 수소 흡착 모델은 수소 플라즈마와 텅스텐 재료간 수소 주입, 흡착, 재방출의 일련의 과정에 대한 이해를 제고함으로써 수소와 같이 흡착반응이 발생하는 방전가스 기반의 플라즈마 시스템의 운전 안정성과 재현성 향상을 위한 플라즈마 천이 예측에도 활용 가능할 것으로 기대한다.

주요어 : 수소 흡착 모델, 플라즈마-벽면 상호 작용 (PWI), 수소 플라즈마, 텅스텐, 열탈착 분광계 (TDS)

학번 : 2012-30268